# Early Detection of Alzheimer's Disease - A Fuzzy Logic based Approach

*Thesis Submitted by*

## Sukanta Ghosh

*Doctor of Philosophy (Engineering)*

**Department of Instrumentation and Electronics Engineering**
**Faculty Council of Engineering and Technology**
**Jadavpur University**
**Kolkata- 700032, India**
**2022**

**Department of Instrumentation and Electronics Engineering**
**Faculty Council of Engineering and Technology**
**Jadavpur University**
**Kolkata- 700032, India**

**Index No:** 261/16/E

**Registration No:** 1021610001

**1. Title of Thesis:** Early Detection of Alzheimer's Disease – A Fuzzy Logic based Approach

**2. Name, Designation and Institution of Supervisors:**

Name: **Dr. Rajanikanta Mudi**
Designation: **Professor**
**Department of Instrumentation and Electronics Engineering**
**Jadavpur University**
**Kolkata – 700106 , India**

Name: **Dr. Abhijit Chandra**
Designation: **Assistant Professor**
**Department of Instrumentation and Electronics Engineering**
**Jadavpur University**
**Kolkata – 700106 , India**

## 3. List of Publication:

## A. International Journals:

- S. Ghosh, A. Chandra, and R. Mudi, "A novel fuzzy pixel intensity correlation based segmentation algorithm for early detection of Alzheimer's disease," *Multimedia tools and Applications*, Springer, vol. 78, issue. 9, pp. 12465-12489, 2018.

- S. Ghosh, A. P. Hazarika, A. Chandra, and R. Mudi, "Adaptive neighbor constrained deviation sparse variant fuzzy c-means clustering for brain MRI of AD subject," *Visual Informatics*, Elsevier, vol. 5, issue. 4, pp. 67-80, 2021.

- S. Ghosh, A. Chandra, R. Mudi and T. K. Biswas, "On the composite implementation of robust morphological filtering along with self adaptive fuzzy clustering for improved lateral ventricle classification", *Signal Image and Video Processing,* Springer (Under Review).

## B. International Conference Proceedings:

- S. Ghosh, A. Chandra, and R. K. Mudi, "On Hippocampus Associative Modeling by Approximating Nonlinear Kullback-Leibler Sparsity Constraint," *2021 International Conference on Computer Communication and Informatics (ICCCI),* pp. 1-5, IEEE, 2021.

- S. Ghosh, A. Chandra, and R. K. Mudi, "An Interactive Hippocampus-Parahippocampus Functional 3D Connectivity Modeling with Quadratic Detrending," *The 12$^{th}$ International Conference on Computing, Communication and Networking Technology (ICCCNT),* IEEE, IIT Kharagpur, 2021.

## C. Patent:  None

# Statement of Originality

I, Sukanta Ghosh registered on 12th May 2016 do hereby declare that this thesis entitled **"Early Detection of Alzheimer's Disease – A fuzzy logic based approach"** contains a literature survey and original research work done by the undersigned candidate as part of Doctoral studies.
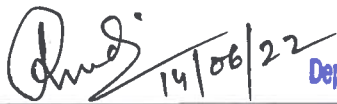
All information in this thesis has been obtained and presented in accordance with existing academic rules and ethical conduct. I declare that, as required by these rules and conduct, I have fully cited and referred all materials and results that are not original to this work.

I also declare that I have checked this thesis as per the ``Policy on Anti Plagiarism, Jadavpur University, 2019", and the level of similarity as checked by iThenticate software is 9 %.

*Sukanta Ghosh*

(Signature of Candidate)

Date:  14/ 06 /2022

*14/06/22*

Professor
Dept. of Instrumentation & Electronics Engg.
Jadavpur University
Saltlake, 2nd Campus
Kolkata-700098

(Certified by Supervisor)
(Signature with date and seal)

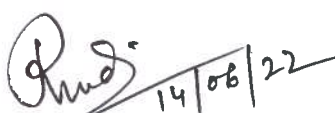*Abhijit Chandra  14/06/2022*

(Certified by Co-Supervisor)
(Signature with date and seal)

Assistant Professor
Dept. of Instrumentation & Electronics Engg
Jadavpur University
Saltlake, 2nd Campus
Kolkata-700 098

# Department of Instrumentation and Electronics Engineering
# Faculty Council of Engineering and Technology
# Jadavpur University
# Kolkata, India

## CERTIFICATE FROM THE SUPERVISOR

This is to certify that the thesis entitled **"Early Detection of Alzheimer's Disease – A fuzzy logic based approach"** was submitted by Sukanta Ghosh, who got his name registered on 12th May 2016 for the award of Ph.D. (Engineering) degree of Jadavpur University, Kolkata, India is absolutely based upon his own work under the supervision of Dr. Rajanikanta Mudi and Dr. Abhijit Chandra and that neither his thesis nor any part of the thesis has been submitted for any degree/diploma or any other academic award anywhere before.

14/06/22

Professor
Dept. of Instrumentation & Electronics Engg.
Jadavpur University
Saltlake, 2nd Campus
Kolkata-700098

_____
(Signature of the Supervisor with the date and official seal)

_Abhijit Chandra 14|06|2022_
_____
(Signature of the Co-Supervisor with the date and official seal)

Assistant Professor
Dept. of Instrumentation & Electronics Engg
Jadavpur University
Saltlake, 2nd Campus
Kolkata-700 098

Dedicated to My Family

# Acknowledgment

I wish to express my heartfelt gratitude and sincere thanks to my esteemed thesis supervisors Prof. Rajanikanta Mudi and Dr. Abhijit Chandra both from the Department of Instrumentation Electronics Engineering, Jadavpur University, Kolkata, India for their relentless guidance, vigorous endeavor, indispensable advice, perpetual encouragement and ceaseless inducement throughout this research work which made the challenging task much gratifying to pursue. I express a deep sense of admiration for their innate goodness. It has been a empyrean grace and my proud privilege to work under their guidance.

I am indebted to Prof. Suranjan Das, Vice-Chancellor, Prof. Samantak Das, Pro-Vice-Chancellor, Prof. Chiranjib Bhattacharjee, Pro-Vice-Chancellor, Prof. Chandan Mazumder, Dean - Faculty Council of Engineering and Technology, Prof. Ratna Ghosh, Head of the Department, Instrumentation and Electronics Engineering, Jadavpur University, Kolkata, India for giving me an opportunity to carry out research at the Institute.

I wish to express my deep sense of gratitude to other members of Individual Research Committee (IRC), Prof. Sekhar Mandal (IIEST, Shibpur), Prof. Salil Kumar Sanyal (Former Professor, Jadavpur University), Prof. Bibhas Chandra Dhara and Prof. Bipan Tudu of Jadavpur University, Kolkata, India for their constructive criticism, valuable suggestions and support throughout the research work. Their editorial excellence of revision is simply outstanding, without which the thesis would have not taken proper shape.

I wish to express my heartfelt gratitude to Sir Visvesvaraya PhD Scheme for Electronics and IT, Ministry of Electronics and Information Technology, Government of India, for providing me financial support during the entire tenure of my research.

I express my gratitude to all my teachers from childhood whose care and contribution has made me able to present in this platform.

I am grateful for the well wishes and prayers of my friends and colleagues for their valuable support and positive suggestions during my research work.

Finally, a very special and sincere heartfelt gratitude to my parents Mr. Sanat Kumar Ghosh and Mrs. Sipra Ghosh, to my wife Mrs. Munmun Adak and to my beloved daughter Ms. Aadrika Ghosh, whose love and constructive support has been a source of inspiration to me. No words can adequately express my gratitude to them.

*Sukanta Ghosh*

Sukanta Ghosh

Department of Electronics & Instrumentation Engineering

Jadavpur University, Salt Lake Campus

Sector III, Block- LB, Kolkata 700106

Date: 14/06/2022

Place: kolkata

# List of Abbreviations

| Abbreviation | Description |
|---|---|
| ACO | Ant Colony Optimization |
| ACWE | Active Contour Without Edges |
| AD | Alzheimer's Disease |
| ADNI | Alzheimer's Disease Neuroimaging Initiative |
| AN_DsFCM | Adaptive Neighbor constrained deviation sparse fuzzy FCM Clustering |
| ARKFCM | Adaptively Regularized Kernel-based Fuzzy c-means Clustering |
| BOLD | Blood Oxygen Level Dependent |
| CA | Cerebral Aneurism |
| CA | Cornu Ammonis |
| CT | Computer Tomography |
| DC | Dice Coefficient |
| DG | Dentate Gyrus |
| DSFCM | Deviation Sparse FCM Clustering |
| DSFCM_N | Neighbor Information based DSFCM |
| ENT | Entorhinal Cortex |
| FC | Functional Connectivity |
| FCM | Fuzzy C-means |
| FCMLSM | Fuzzy C-means with Level Set Methods |
| FDCM | Fuzzy Double c mean method |
| FGFCM | Fast Generalized Fuzzy c-means |
| FIS | Fuzzy Inference System |
| FLICM | Fuzzy Clustering Method using Local Information |
| FLS | Fuzzy logic system |
| f-MRI | Functional Magnetic Resonance Imaging |
| FN | False Negetive |
| FOM | Figure of Merit |

| | |
|---|---|
| FP | False Positive |
| FRFCM | Fast and Robust Fuzzy c-means Clutering |
| GA | Genetic Algorithm |
| GT | Ground Truth |
| HC | Healthy Control |
| H-PH | Hippocampus- Parahippocampus |
| JI | Jaccard Index |
| KGFCM | Kernel Generalized Fuzzy c-means Clustering |
| K-L | Kullback-Leibler (K-L) divergence |
| KWFLICM | Kernel Version of FLICM |
| LV | Lateral Ventricle |
| MCI | Mild Cognitive Impairment |
| MF | Morphological Filtering |
| MG | Morphological Gradient |
| fMRI | Functional Magnetic Resonance Imaging |
| sMRI | Structural Magnetic Resonance Imaging |
| MNI | Montreal Neurological Institute standard atlas |
| MRI | Magnetic Resonance Imaging |
| MTL | Medial Temporal Lobe |
| NDFCM | Noise Detecting Fuzzy c-means Clustering |
| NWFCM | Neighborhood Weighted Fuzzy c-means Clustering |
| PCM | Possibilistic c means |
| PET | Positron Emission Tomography |
| PFCM | Possibilistics Fuzzy c-means |
| PHC | Posterior Parahippocampal Cortices |
| PRC | Perirhinal Cortices |
| REST | Resting-State fMRI Data Analysis |
| Rf-MRI | Resting State Functional Magnetic Resonance Imaging |
| RG | Region Growing |
| ROI | Region of Interest |
| RSC | Retrosplenial Cortices |

| | |
|---|---|
| SA | Segmentation Accuracy |
| SE | Structuring Element |
| SPCM | Sparsity-aware Possibilisctics Clustering Method |
| SPM | Statistical Parametric Mapping |
| SSIM | Structural Similarity Index Measure |
| STNeT | Spatial-Temporal Convolutional-recurrent neural Network |
| TN | True Negetive |
| TP | True Positive |
| VGC | Validity Guided Re-clustering |

# Contents

## Chapter 1: Introduction

## Chapter 2: Literature Overview

## Chapter 3: A Novel Fuzzy Pixel Intensity Correlation Based Brain MRI Segmentation Algorithm

# Chapter 4: A Composite Implementation of Robust Morphological Filtering and Self Adaptive Fuzzy Clustering for Improved Lateral Ventricle Classification

# Chapter 5: An Adaptive Neighbor Constrained Deviation Sparse Variant Fuzzy C-Means Clustering Algorithm for Brain MRI of AD Subject

# Chapter 6: Hippocampus Associated Functional 3D Connectivity Modeling

# Chapter 7: Conclusion & Future Scope of Work

# List of Figures

# List of Tables

# Abstract

Alzheimer's disease (AD) is the most widespread and fatal neurodegenerative dementia in the recent past. Prominent symptoms of AD include short-term and long-term memory loss, poor judgment, abstract thinking, disorientation of time and place, emotional outbreaks etc. AD substantially affects elderly persons and the progression of disease becomes worse over time. AD starts very slowly and is mostly detected at a later stage where treatment can only improve some temporary symptoms but reversal or termination of the progression of disease seems to be impossible. AD-related primary cognitive declinement is largely known as mild cognitive impairment (MCI) which has a very high tendency to be converted into severe AD as compared to healthy control (HC). Hence, the prevention of AD is mostly dependent on diagnosis at a trivial stage of MCI. Magnetic resonance imaging (MRI) is regarded as a reliable, non-invasive, and most effective tool for the diagnosis of brain diseases over a long time. This thesis work introduces various novel methodologies of analyzing MRI and Rf-MRI (Resting state functional MRI) images to develop the tools for detecting AD at an early stage.

Mild and severe AD is associated with tissue loss in the medial temporal lobe (MTL) and hippocampus. MCI can be more accurately identified by precise detection of object boundaries in brain MRI scans. Existing edge detection techniques fundamentally select each pixel in digital image space and examine whether they can be considered as an edge pixel or not. Proposed algorithm follows some other paths and finds out the connectedness and natural attachment of pixels that exist in edges of image object boundary. It figures out the connected edge line based on fuzzy weights of pixel intensities for brain MRI subjects. A novel fuzzy rule base and fuzzy inference system is implemented where a fuzzy pixel intensity-based topological selection of adjacent edge pixels is developed for higher-order precision. Since brain MRI scans are generally of low contrast, the presented algorithm extracts regional boundaries with more precision which becomes capable to predict or check disease progression. The presented method emphasizes on settling the primary edge pixel and figures out the next adjacent pixel that can be considered as an edge pixel depending on a dynamic fuzzy pixel intensity correlation algorithm. The selected edge pixels are further accumulated in the pixel matrix to identify the impression of edge

contour. Proposed algorithm leads to tracing early impairment in human brain and helps to detect MCI.

AD, associated with tissue loss in MTL and hippocampus, can be identified by correlated enlargement of the lateral ventricle (LV) region. In connection to this, a composite implementation of several algorithms is presented which is an improved extractor of LV in a form of a segregated entity. A robust morphological filtering process is presented that can eliminate noise, focus lateral ventricle and avoid overestimation in object boundary as well. An improved fuzzy c-means (FCM) clustering algorithm is successfully employed on test MRI images to enhance the lateral ventricle region information. Presented clustering algorithm iteratively uses improved FCM to settle for optimum clustering validity index. This process minimizes the chance of ventricular information loss and simultaneously avoids overestimation. By means of appropriate implementation of active contour without edges (ACWE) and region growing (RG) algorithms with proper seed point, the LV is separated as a single and connected entity for cerebral cortical atrophy subjects. The presented method exhibits superior ability to classify LV both qualitatively and quantitatively. It has subsequently been simulated on a large data set of different MRI subjects. The experimental outcomes demonstrate that the executed method efficiently segregates HC, MCI and AD subjects. Therefore, the presented technique may be used as a viable tool to detect early Alzheimer's disease.

Diagnosing brain MRI scans with an advanced FCM clustering algorithm helps to take appropriate intervention for tracing out MCI. A novel clustering algorithm is presented where firstly the sparsity is initiated for brain MR scans of AD subject. Secondly, a unique neighbor pixel constrained FCM clustering algorithm is designed and implemented where a topology-based selection of parsimonious neighbor pixel is automated. The adaptability in choice of neighbor pixel class creates a more justified object edge boundary. The presented adaptive neighbor constrained deviation sparse variant fuzzy c-means clustering (AN_DsFCM) can withhold imposed sparsity and withstand rician noise. This robust algorithm is applied for MRI of AD subjects and normative data is acquired to analyze clustering accuracy. The data processing pipeline of a theoretically plausible proposition is elaborated in detail. The experimental results are compared with state-of-the-art fuzzy clustering methods for test MRI scans. Visual evaluation and statistical measures are studied to meet both image processing and clinical neurophysiology standards.

Early identification of dementia can be achieved by diagnosis of blood oxygen level dependent (BOLD) signal-based functional magnetic resonance imaging (f-MRI) at resting-state. Detection of dementia at the stage of MCI is limited to effective spatial-temporal dependency. The functional connectivity (FC) among various hubs of human brain estimates neuronal health and disease progression. Due to motion-related artifacts at acquisition time, noise intervention, and many other reasons, the sparse constraint becomes predominant in Rf-MRI. A unique Kullback-Leibler (K-L) divergence-based sparse constrained regression model is presented, which creates a framework to identify and analyze connectivity between the hippocampus and other significant regions of interest (ROI) of brain. Experimental results demonstrate a promising improvement in hippocampus centric connectivity measurements. Outcome of simulated results also appears in the form of a whole-brain correlation matrix which shows significant improvement in connectivity constraints.

Since the MCI related tissue loss primarily affects MTL and hippocampus, the consequent functional connectivity degradation can be observed in Rf-MRI analysis. A three-dimensional model for FC analysis between hippocampus and parahippocampus is presented to trace the early signs of MCI. The FC between each hippocampal subfields and parahippocampal subfields in their entirety is examined. A quadratic detrending algorithm is implemented to model both complex scanner drift constraints and longer scan sessions. The noise interventions and motion-related artifacts and are also well handled by the presented framework. Outcomes in terms of correlation matrix demonstrate noticeable efficiency of dealing with functional connectivity constraints between hippocampus and parahippocampus. The entire process including full brain FC analysis leads to trace MCI related connectivity malfunctions.

# List of Figures

# List of Tables

# Abstract

Alzheimer's disease (AD) is the most widespread and fatal neurodegenerative dementia in the recent past. Prominent symptoms of AD include short-term and long-term memory loss, poor judgment, abstract thinking, disorientation of time and place, emotional outbreaks etc. AD substantially affects elderly persons and the progression of disease becomes worse over time. AD starts very slowly and is mostly detected at a later stage where treatment can only improve some temporary symptoms but reversal or termination of the progression of disease seems to be impossible. AD-related primary cognitive declinement is largely known as mild cognitive impairment (MCI) which has a very high tendency to be converted into severe AD as compared to healthy control (HC). Hence, the prevention of AD is mostly dependent on diagnosis at a trivial stage of MCI. Magnetic resonance imaging (MRI) is regarded as a reliable, non-invasive, and most effective tool for the diagnosis of brain diseases over a long time. This thesis work introduces various novel methodologies of analyzing MRI and Rf-MRI (Resting state functional MRI) images to develop the tools for detecting AD at an early stage.

Mild and severe AD is associated with tissue loss in the medial temporal lobe (MTL) and hippocampus. MCI can be more accurately identified by precise detection of object boundaries in brain MRI scans. Existing edge detection techniques fundamentally select each pixel in digital image space and examine whether they can be considered as an edge pixel or not. Proposed algorithm follows some other paths and finds out the connectedness and natural attachment of pixels that exist in edges of image object boundary. It figures out the connected edge line based on fuzzy weights of pixel intensities for brain MRI subjects. A novel fuzzy rule base and fuzzy inference system is implemented where a fuzzy pixel intensity-based topological selection of adjacent edge pixels is developed for higher-order precision. Since brain MRI scans are generally of low contrast, the presented algorithm extracts regional boundaries with more precision which becomes capable to predict or check disease progression. The presented method emphasizes on settling the primary edge pixel and figures out the next adjacent pixel that can be considered as an edge pixel depending on a dynamic fuzzy pixel intensity correlation algorithm. The selected edge pixels are further accumulated in the pixel matrix to identify the impression of edge

contour. Proposed algorithm leads to tracing early impairment in human brain and helps to detect MCI.

AD, associated with tissue loss in MTL and hippocampus, can be identified by correlated enlargement of the lateral ventricle (LV) region. In connection to this, a composite implementation of several algorithms is presented which is an improved extractor of LV in a form of a segregated entity. A robust morphological filtering process is presented that can eliminate noise, focus lateral ventricle and avoid overestimation in object boundary as well. An improved fuzzy c-means (FCM) clustering algorithm is successfully employed on test MRI images to enhance the lateral ventricle region information. Presented clustering algorithm iteratively uses improved FCM to settle for optimum clustering validity index. This process minimizes the chance of ventricular information loss and simultaneously avoids overestimation. By means of appropriate implementation of active contour without edges (ACWE) and region growing (RG) algorithms with proper seed point, the LV is separated as a single and connected entity for cerebral cortical atrophy subjects. The presented method exhibits superior ability to classify LV both qualitatively and quantitatively. It has subsequently been simulated on a large data set of different MRI subjects. The experimental outcomes demonstrate that the executed method efficiently segregates HC, MCI and AD subjects. Therefore, the presented technique may be used as a viable tool to detect early Alzheimer's disease.

Diagnosing brain MRI scans with an advanced FCM clustering algorithm helps to take appropriate intervention for tracing out MCI. A novel clustering algorithm is presented where firstly the sparsity is initiated for brain MR scans of AD subject. Secondly, a unique neighbor pixel constrained FCM clustering algorithm is designed and implemented where a topology-based selection of parsimonious neighbor pixel is automated. The adaptability in choice of neighbor pixel class creates a more justified object edge boundary. The presented adaptive neighbor constrained deviation sparse variant fuzzy c-means clustering (AN_DsFCM) can withhold imposed sparsity and withstand rician noise. This robust algorithm is applied for MRI of AD subjects and normative data is acquired to analyze clustering accuracy. The data processing pipeline of a theoretically plausible proposition is elaborated in detail. The experimental results are compared with state-of-the-art fuzzy clustering methods for test MRI scans. Visual evaluation and statistical measures are studied to meet both image processing and clinical neurophysiology standards.

Early identification of dementia can be achieved by diagnosis of blood oxygen level dependent (BOLD) signal-based functional magnetic resonance imaging (f-MRI) at resting-state. Detection of dementia at the stage of MCI is limited to effective spatial-temporal dependency. The functional connectivity (FC) among various hubs of human brain estimates neuronal health and disease progression. Due to motion-related artifacts at acquisition time, noise intervention, and many other reasons, the sparse constraint becomes predominant in Rf-MRI. A unique Kullback-Leibler (K-L) divergence-based sparse constrained regression model is presented, which creates a framework to identify and analyze connectivity between the hippocampus and other significant regions of interest (ROI) of brain. Experimental results demonstrate a promising improvement in hippocampus centric connectivity measurements. Outcome of simulated results also appears in the form of a whole-brain correlation matrix which shows significant improvement in connectivity constraints.

Since the MCI related tissue loss primarily affects MTL and hippocampus, the consequent functional connectivity degradation can be observed in Rf-MRI analysis. A three-dimensional model for FC analysis between hippocampus and parahippocampus is presented to trace the early signs of MCI. The FC between each hippocampal subfields and parahippocampal subfields in their entirety is examined. A quadratic detrending algorithm is implemented to model both complex scanner drift constraints and longer scan sessions. The noise interventions and motion-related artifacts and are also well handled by the presented framework. Outcomes in terms of correlation matrix demonstrate noticeable efficiency of dealing with functional connectivity constraints between hippocampus and parahippocampus. The entire process including full brain FC analysis leads to trace MCI related connectivity malfunctions.

# Chapter 1

# Introduction

Digital image processing is an indispensable component of the state-of-the-art research in medicinal diagnosis, neuroscience, space science, cosmology, optics, etc [1]. Image processing has enormous participation in various diagnoses of neurological disorders. Alzheimer's disease (AD) is major neurodegenerative dementia that mostly affects elderly persons. AD leads to memory loss, poor judgment, abstract thinking, disorientation of time and place [2, 3]. Detecting AD at an early stage, named as mild cognitive impairment (MCI), plays a crucial role in defending the disease progression as medication and precaution initiatives are started [4, 5] by that time. Severity of AD progression is observed with gradual tissue loss in some specific regions of the brain [6].

Prediction of brain disease mostly depends on the systematic analysis of brain images since it is considered as a noninvasive and most facile study. Magnetic resonance imaging (MRI) is the most efficient brain imaging tool compared to computed tomography (CT) or positron emission tomography (PET), as it produces most prominent images of human brain. The MRI impressions of the brain generally represent several overlapping soft tissue cell types. Intervention of highly efficient image quality enhancement algorithms is therefore required to trace the progression of MCI or cause of MCI [7].

## 1.1 Motivation

The number of neuronal disorders is rapidly increasing with unregulated lifestyle and mental stress. These include anxiety, consumption of junk food, unhealthy work and social life balance, poor vegan diet, lack of quality time spent for mental relaxation, and many more which are most crucial for mental health and psychological well-being [11]. There are various dementia which become prominent irrespective of age, like Parkinson's disease, Vascular dementia, Huntington's

disease, Dementia with Lewy bodies, etc [2]. However, other types of dementia like AD, Creutzfeldt-Jakob disease (CJD) etc mostly occur for elderly persons and their effect increases by aging. Globally, dementia is the seventh leading cause of death among all types of diseases [12]. Dementia is also counted as the most prominent cause of dependency and disability for elderly persons. AD is associated with tissue loss at different portions of brain depending on severity of the disease [13] and is responsible for 60-70% cases of dementia worldwide. The principal component of diagnosis for early traces of AD is MRI. As soon as AD is detected at a primary stage, preclusive therapies can be initiated [5] at an earliest. The treatment of AD is mostly preventive as the tendency of tissue loss prolongs. By adopting non-invasive MRI as a diagnosis technique, one can minimize the hazards and risky sample tissue analysis procedures. Functional magnetic resonance imaging (f-MRI) has become a crucial parameter in many of the state-of-the-art research in progression of this disease.

Typical human brain consists of billions of neurons formulating gray matter (GM), white matter (WM) and a fluidic substance called cerebrospinal fluid (CSF). Structural regions of brain overlap with each other and construct a complex shape that varies for each subject. In connection to this, CT provides low contrast brain images which are used for primary analysis about brain conditions. MRI, on the other hand, provides a much more contrast-enhanced insight of brain structure which is further used for in-depth study. Recent state-of-the-art brain study also includes the connectivity among different functional hubs [15]. The functional magnetic resonance imaging provides both structural and functional activity of different regions of interest (ROI) [14, 15]. The functional activity is dynamic which is estimated from BOLD (blood-oxygen-level-dependent) data. The f-MRI is captured and analyzed both in resting state and through activity analysis [16, 17]. Task-based s-MRI or activity-based f-MRI is analyzed to study the correlation among different functional parts of the brain [18, 19]. For predicting neurodegenerative brain diseases like AD, the resting state analysis is an obvious choice as it is more immune to noise interventions. Hence, the appropriate analysis in the context of resting-state functional magnetic resonance image (Rf-MRI) can provide deep insight into structural deformation [20, 21]. This structural deformation leads to predict early signs of AD.

For long, image processing tools are recognized as good choices for extracting crucial information of brain conditions. MRI-based image processing algorithms mainly focus to extract structural information. Regional boundary detection of different parts of brain becomes very challenging as there are several overlapping soft tissue regions. Boundary detection or edge detection plays the most pivotal role in the determination of regional areas. Similarly, the clustering tool in image processing provides each brain region in a single connected zone. The process further leads to making a three-dimensional modeling which is used to estimate the volume of specific regions. Hence, volume degradation due to tissue loss can be traced out. Although the conventional edge detection or clustering algorithms run well for standard images, more advanced edge detection and clustering algorithms are required to meet the accuracy of MRI images. The search for suitable edge detectors and clustering algorithms is being addressed by various soft computing tools of late. The fuzzy logic is a widely used soft computing tool which is being applied in the field of image processing for a long time. Keeping in mind the nature of low contrast grayscale pixel intensity domain in MRI scans, fuzzy-based advanced edge detection techniques and clustering methods are much suitable to provide improved results. These results may deliberately help to provide the accuracy required for tracing volume degradation due to tissue loss for early AD.

Rf-MRI-based image algorithms are used to extract the functional activity of major ROI. The structural deformation due to tissue loss affects the functional connectivity (FC) of brain which is reflected in Rf-MRI impressions. So, the robust connectivity models for Rf-MRI can provide a better response to functional change. This process inherently becomes capable to trace small structural changes due to tissue loss for early MCI.

## 1.2 Objective

Main objective of this thesis work is to develop robust processing algorithms for the early detection of AD from brain MRI images. This research work has the purpose of identifying early AD by analyzing MRI images with the aid of advanced soft computing measures, especially by employing fuzzy-based approaches. The thesis has an additional objective to find out some Rf-

MRI based advanced process which is more capable to identify minute changes in FC due to structural degradation. The objective of this thesis work can be summarized as follows:

- To find out the limitations of existing edge detection algorithms in the context of brain MRI scans, overcoming the drawbacks by designing new edge detection strategies that can distinguish prominent regional edge boundaries.
- To develop new composite methods that can find out some easy and effective measures to estimate the tissue loss in regions where the effect of MCI is primarily observed, especially the medial temporal lobe (MTL).
- To find out the limitations of existing image clustering methods in the context of brain MRI scans, and design new algorithms that can produce more robust clustering results to trace early tissue loss due to MCI.
- To develop appropriate spatial-temporal dependency mathematical models that can identify and analyze the functional connectivity (FC) between multiple target ROI by eliminating diverse noise artifacts in Rf-MRI domain.
- To find out a robust interactive three-dimensional connectivity modeling scheme for medial temporal lobe subfields which is capable to handle complex scanner drifts and motion-related artifacts in Rf-MRI domain.

## 1.3  Methodology

Early detection of AD precisely requires higher-order accuracy in the MRI or Rf-MRI processing techniques which are currently practiced. Although the conventional methods are adequate for standard images, more robust algorithm is required for brain MRI or Rf-MRI processing. The exploration of advanced methods demands state-of-the-art fuzzy edge detection techniques, composite lateral ventricle classifier, robust clustering algorithm, spatial-temporal dependency FC model, and interactive 3D connectivity model for medial temporal lobe subfields.

Desirable edge detection tool needs to be evolved in a dynamic algorithm that provides the potential outcome for brain MRI scans. Existing fuzzy edge detection techniques have an inherent drawback in efficiency of filtering and finding out optimum edge contour. Normalized

MRI scans are needed to be filtered such that essential information should be preserved. The distinction between an edge pixel and a non-edge pixel is needed to be done more vigorously. It is desirable to design an algorithm that can fetch major components in MRI image space and incorporate a high order dynamic selection procedure of edge pixels. The combination of morphological filtering and novel fuzzy edge detector provides an improved regional boundary of brain MRI.

Improved composite implementation of multiple imaging techniques is planned to be executed alongside improved clustering performance for clear measures of AD progression. The process of formulating the less complex measures will help to additionally trace the interventions of MCI. Due to progression early AD, the tissue loss is primarily observed in MTL and then lateral temporal and partial lobes. As a matter of fact, temporal tissue loss can be identified by an enlargement measure of the lateral ventricle (LV). In connection to this, a composite process has been designed by using appropriate filtering, improved clustering, segmentation and region growing algorithm. The process can segregate any particular section into a single connected region. This scheme leads to provide classified and improved LV sections in this work. The proposed algorithm is successfully implemented on large scale MRI images of different AD subjects. Here the experimental outcomes demonstrate that the proposed method is capable to segregate HC, MCI and AD subjects.

A novel clustering algorithm is planned to be designed for more accurate outputs in the context of MRI image domain. The performance of the proposed method is scheduled to be executed in robust circumstances by introducing rician noise and sparse constraints. Thus various noise constraints are mathematically modeled and designed to be filtered out through the clustering process. The scheme of clustering is fabricated in such a way that topology-based selection of parsimonious neighbor pixel is incorporated mathematically and executed properly. The performance of the proposed strategy is further evaluated by comparing it with other state-of-the-art clustering methods.

The functional connectivity model has become a vital tool for analyzing the correlation between major ROIs which is dynamic in nature. In the context of tracing the neurodegenerative diseases,

the network hub connectivity analysis potentially provides a local to global spatial-temporal dynamic connectivity model for each subject. The BOLD signal-based functional connectivity sequences provide a deep insight into brain which can be utilized to reveal information integration and communication among prominent regions. Conventional Rf-MRI based functional connectivity analysis has not yet been largely explored for neurodegenerative brain disease progression studies. In regard to this, a novel functional connectivity based mathematical strategy for hippocampus associative modeling and efficient sub MTL modeling is designed. These models will actively help to figure out minute changes in FC divergence or alteration due to tissue loss. A hippocampus associative modelling by appropriate mathematical modelling eliminates different type of noise constraints. On the other hand, the inter MTL FC analysis is another key indicator of structural change due to early MCI. The process needs to be a highly accurate study and minute interventions in terms of noise should be mathematically modelled and eliminated on the simulation process. A dynamic 3D detrending model is executed to study the interactive inter MTL, hippocampus-parahippocampus (H-PH) FC analysis. The FC analysis between H-PH creates a framework that enables segregating the structural changes.

## 1.4  Major Contribution

Main contributions of this thesis work are listed in this subsection as follows:

- A novel algorithm is presented which follows the connectedness and natural attachment of pixels located in edges of image object boundary and finds the connected edge line based on fuzzy weights of pixel intensities for AD brain MRI subjects. In this context, a robust fuzzy rule base and fuzzy inference system (FIS) have been designed and implemented where a fuzzy pixel intensity weight-based topological selection of connected edge pixels has been developed for higher-order precision. Since brain MRI scans are normally of low contrast, the presented algorithm is designed to extract regional boundaries with more precision which can easily predict or check disease progression. The method emphasizes settling the primary edge pixel and searches for the next adjacent pixel that can be counted as an edge pixel based on fuzzy pixel intensity correlation dynamically. Both the fuzzy rule base and FIS have been uniquely designed so that a

topology-based selection scheme is evolved to choose the next adjacent edge pixel. Finally, the selected edge pixels are accumulated in the image pixel matrix to trace an impression of edge contour. The implemented algorithm together with image opening and morphological gradient (MG) exhibits promising improvement over other existing edge detection algorithms. This novel strategy leads to tracing early impairment in human brain and helps us to detect the possible occurrence of AD.

- A new composite implementation of robust morphological filtering together with self adaptive fuzzy clustering for improved lateral ventricle classification is presented. Firstly, a robust morphological filter on brain MRI scans for cerebral cortical atrophy subject is presented which produces a promising extraction of lateral ventricle edge information. Secondly, an improved fuzzy c means (FCM) clustering algorithm has been successfully employed on brain MRI test images to enhance the connected lateral ventricle region information. Implemented clustering method iteratively uses modified FCM to settle for optimum clustering validity index. In addition to this, ACWE and RG techniques have been subsequently applied to set apart LV from the rest of the brain regions. Composite implementation of morphological filtering and robust FCM clustering algorithm shows excellent extraction of LV region information both qualitatively and quantitatively. Further ACWE along with RG provides excellent segregation of region of interest (ROI). The presented method exhibits superior ability to classify HC, MCI and AD in terms of segmented LV regional information.

- One novel adaptive neighbor information constrained deviation sparse fuzzy c-means clustering (AN_DsFCM) algorithm is presented. Primarily test MR images are exposed to low-level rician noise. It leads to a noise handling capability estimation of presented AN_DsFCM. This process works by estimating theoretical value or actual value rather than the acquired value with the aid of deviation sparse which has a precise impact on clustering outcome. The neighbor information is the major artifact that is modeled by the fuzzy objective function. While the first part of presented algorithm dynamically selects a neighbor set which is to be converted in the current cluster set; the second part focuses on noise handling attributes. An adaptive neighbor constraint is operated such that

AN_DsFCM provides an adorable cluster standard. In brief, the adaptive neighbor information constraint and sparsity in deviations to approximate theoretical value are delivered to meet the precision standard of brain MR images of AD subjects.

- An improved hippocampus associated functional connectivity (FC) modelling is presented by approximating nonlinear Kullback-Leibler (K-L) sparsity constraint. A novel K-L divergence based regression model is presented which takes care of sparsity constraints in a robust way. Simulated result outcomes exhibit an improved dynamic FC in terms of a correlation matrix. A robust hippocampus-parahippocampus three dimensional functional connectivity model with quadratic detrending is proposed. The quadratic detrending process is presented which is capable to model both longer scan sessions and scanner drift constraints. The process is mainly designed to model FC between hippocampus and para-hippocampus in view of predicting MCI at an early stage. Simulation results show efficient outcomes in terms of a correlation coefficient.

## 1.5  Dissertation Overview

The remaining part of the thesis is organized as follows:

- Chapter 2 describes an elaborated literature review in the context of fuzzy theory-based edge detection methods, LV classification algorithms, clustering methods, and its diverse applications in potential fields for analysis of brain MRI scans. The theoretical background of fuzzy theory, morphological filtering, edge detection, fuzzy clustering is explained in view of the presented theme. This chapter also focuses on a detailed literature survey on different BOLD signal-based FC models of brain scans to figure out the potential scope of MTL to global and inter MTL FC analysis in the context of tracing out early signs of MCI.  Various aspects of mathematical and conceptual background are elaborated with an emphasis to achieve a potential MTL-related FC model.

- Chapter 3 represents a novel scheme of fuzzy pixel intensity correlation-based edge

detection algorithm for brain MRI scans. Implementation of robust morphological filtering, a new FIS system, and a dynamic correlation-based pixel classifier is presented in this chapter. Additionally, several methods of soft computing based algorithms are executed to demonstrate the supremacy of the presented algorithm.

- In the context of segregation of LV, chapter 4 discusses a composite execution of MF, improved FCM with optimum clustering validity index, ACWE, and RG algorithm. Each part of the composite method is critically designed by preserving the boundary information. The presented method also takes care of possible overestimation such that MCI can be predicted with the requisite precision. Capability of the method to segregate different subjects of HC, MCI and AD is successfully evaluated and demonstrated for a large data set.

- Chapter 5 illustrates a novel Fuzzy c-means clustering algorithm which incorporates sparse constraints. The process is designed such that topology-based selection of parsimonious neighbor pixel is automated in MRI image space. The adaptability in choice of neighbor pixel class produces more justified object edge boundary which outperforms a dynamic cluster output. The demonstrated process yields an improved clustering accuracy which is required to figure out MCI.

- Chapter 6 introduces Rf-MRI based advanced algorithms on functional connectivity model to estimate associativity between hippocampal subregions and neighboring cortical fields. Initially, a robust K-L divergence based regression model is demonstrated which eliminates the noise by eliminating the sparse constraint and provides improved hippocampus connectivity. Secondly, an inter MTL hippocampus-parahippocampus quadratic detrending model is presented towards predicting MCI. The process is mainly designed to model FC between hippocampus and parahippocampus in view of predicting MCI at an early stage. Additionally, it is also observed that the algorithm is capable to model both longer scan sessions and scanner drift constraints.

- Chapter 7 concludes major findings of the thesis. The potential scope of future work is

also discussed in this chapter.

# REFERENCES

[1] Rafael C. Gonzalez, Richard E. Woods, Digital Image Processing, 3$^{rd}$ ed., Pearson India.

[2] W. H. Organization et al., "Dementia: Fact sheet no. 362. 2017," WHO. Available online at: http://www. who. int/mediacentre/factsheets/fs362/en/. Accessed, vol. 2, 2017.

[3] A. Burns and S. Iliffe, "Alzheimer's disease. bmj 338, b158," 2009.

[4] C. Misra, Y. Fan, and C. Davatzikos, "Baseline and longitudinal patterns of brain atrophy in mci patients, and their use in prediction of short term conversion to ad: results from adni," Neuroimage, vol. 44, no. 4, pp. 1415–1422, 2009.

[5] B. Singh, M. M. Mielke, A. K. Parsaik, R. H. Cha, R. O. Roberts, P. D. Scanlon, Y. E. Geda, T. J. Christianson, V. S. Pankratz, and R. C. Petersen, "A prospective study of chronic obstructive pulmonary disease and the risk for mild cognitive impairment," JAMA neurology, vol. 71, no. 5, pp. 581–588, 2014.

[6] D. Ferreira, C. Verhagen, J. A. Hernandez-Cabrera, L. Cavallin, C. J. Guo, U. Ekman.et al., "Distinct subtypes of Alzheimer's disease based on patterns of brain atrophy: longitudinal trajectories and clinical applications," Nature Neuroscience, DOI: 10.1038/srep46263., 2017.

[7] J. J. Hsiao and E. Teng, "Depressive symptoms in clinical and incipient alzheimer's disease," Neurodegenerative disease management, vol. 3, no. 2, pp. 147–155, 2013.

[8] X. Mu˜noz, J. Freixenet, X. Cufı, and J. Martı, "Strategies for image segmentation combining region and boundary information," Pattern recognition letters, vol. 24, no. 1-3, pp. 375–392, 2003.

[9] Y. Guo, L. Jiao, S. Wang, S. Wang, F. Liu, and W. Hua, "Fuzzy superpixels for polarimetric sar images classification," IEEE Transactions on Fuzzy Systems, vol. 26, no. 5, pp. 2846–2860, 2018.

[10] J. Gu, L. Jiao, S. Yang, and F. Liu, "Fuzzy double c-means clustering based on sparse self-representation," IEEE Transactions on Fuzzy Systems, vol. 26, no. 2, pp. 612–626, 2017.

[11] M.V.F. Silva, C.D.M.G. Loures, L.C.V. Alves, L.C. de Souza, K.B.G. Borges, and G. C. Maria Das, "Alzheimer's disease: risk factors and potentially protective measures", Journal of biomedical science, vol. 26. no.1, pp.1-11,2019.

[12] K. D. Kochanek, S. L. Murphy, J. Xu, and E. Arias, "Deaths: final data for 2017," 2019.

[13] J. L. Whitwell, C. R. Jr. Jack, S. A. Przybelski, J. E. Parisi, M. L. Senjem, B. F. Boeve.et al. "Temporoparietal atrophy: a marker of AD pathology independent of clinical diagnosis," Neurobiol. Aging, vol. 32, no. 9, pp. 1531–1541, 2011.

[14] M. Machulda, H. Ward, B. Borowski, J. Gunter, R. Cha, P. Obrien, R. Petersen, B. Boeve, D. Knopman, D. Tang-Wai et al., "Comparison of memory fMRI response among normal, MCI, and Alzheimer's patients," Neurology, vol. 61, no. 4, pp. 500–506, 2003.

[15] J. S. Damoiseaux, "Resting-state fMRI as a biomarker for Alzheimer's disease?" Alzheimer's Research and Therapy, vol. 4, no. 8, pp. 1–2, 2012.

[16] C.-Y. Wee, P.-T. Yap, D. Zhang, L. Wang, and D. Shen, "Groupconstrained sparse fMRI connectivity modeling for mild cognitive impairment identification," Brain Structure and Function, vol. 219, no. 2, pp. 641–656, 2014.

[17] B. Jie, M. Liu, D. Zhang, and D. Shen, "Sub-network kernels for measuring similarity of brain connectivity networks in disease diagnosis," IEEE Transactions on Image Processing, vol. 27, no. 5, pp. 2340–2353, 2018.

[18] B. Jie, M. Liu, D. Zhang, and D. Shen, "Sub-network kernels for measuring similarity of brain connectivity networks in disease diagnosis," IEEE Transactions on Image Processing, vol. 27, no. 5, pp. 2340–2353, 2018.

[19] J. Zhang, W. Cheng, Z. Liu, K. Zhang, X. Lei, Y. Yao, B. Becker, Y. Liu, K. M. Kendrick, G. Lu et al., "Neural, electrophysiological and anatomical basis of brain-network variability and its characteristic changes in mental disorders," Brain, vol. 139, no. 8, pp. 2307–2321, 2016.

[20] R. M. Hutchison, T. Womelsdorf, E. A. Allen, P. A. Bandettini, V. D. Calhoun, M. Corbetta, S. Della Penna, J. H. Duyn, G. H. Glover, J. Gonzalez-Castillo et al., "Dynamic functional connectivity: Promise, issues, and interpretations," NeuroImage, vol. 80, pp. 360–378, 2013.

[21]    M. Wang, D. Zhang, J. Huang, P.-T. Yap, D. Shen, and M. Liu, "Identifying autism spectrum disorder with multi-site fMRI via low-rank domain adaptation," IEEE Transactions on Medical Imaging, 2019.

# Chapter 2

# Literature Review

## 2.1 Alzheimer's Disease and Detection Methods

In the current era of technology, digital image processing (DIP) technique is considered as one of the most powerful tool which is applied in diverse domains.

Cerebral atrophy is a transpiring neuronal disorder that is common for most fatal brain diseases. The most prominent neural disease which is intimated as cerebral cortical atrophy and accounts for 60% to 70% of cases of dementia is Alzheimer's disease (AD) [1]. Alzheimer's disease (AD) is the major neurodegenerative dementia for elderly persons that lead to memory loss, confusion, abstract thinking, and disorientation in time and place, and poor judgment. The primary stage of AD is called mild cognitive impairment (MCI) which starts very slowly and becomes worse over time. AD is mostly detected at late-stage where treatment can only improve some temporary symptoms but reverse or stop of progression is not possible [2]. Mild cognitive impairment is the beginning of cognitive declinement which does not notably interfere in daily activities [3]. Healthy control (HC) has a chance to convert into AD at about 1% - 2% [4] while MCI produces a high risk of developing AD with an estimation of 10% - 20% [5]. The tendency of cerebral cortical atrophy affectedness increases with aging and is identified as gradual shrinkage of both hippocampus and associative cortex tissue loss [6, 7]. Precise pharmacological initiatives can delay or restrict progression of MCI into moderate and severe stages [8]. Thus, to prevent AD, it is most important to diagnose and detect it at trivial stage of MCI. However detection of MCI becomes challenging due to mild symptoms and individual subject constraints [9].

MCI can be accurately identified by precise detection of image object boundaries of brain MRI. An edge point in any digital image is a continuous higher order change in intensity or color between adjacent pixels. The edge contour is absolutely random in nature and represents an

object structure in most of the cases. Extracting shapes from various images becomes even more challenging in presence of noise and therefore necessitates the use of sophisticated algorithms [10, 11]. There exist a number of state-of-the-art algorithms for detecting edges in a digital image among which Roberts, Sobel, Canny, Prewitt and LoG are most popular [12-16]. In regard to this, Salinas et al. [17] and Perona et al. [18] proposed algorithms to produce sharp object boundaries compared to other Gaussian techniques.

Recent studies recognize neuropathological and structural heterogeneity in MTL regional tissue loss for MCI and AD [19, 20]. The tendency of losing neuronal tissue is noticed mostly in some specific regions of human brain. Starting from para-hippocampus of MTL, shrinkage in volume of different brain cortices occurs in parallel. AD patients encounter a prominent atrophy in MTL due to diminution of hippocampus and hypertrophy is distinguished in temporal horn of lateral ventricles [21]. It is also spotted that the loss of neurons in human brain starts from hippocampus which controls the long term memory and emotional responses [22]. Nestor et al. suggested that the tissue loss in MTL can be predicted with enlargement of temporal horn in LV [23]. Therefore the extraction of lateral ventricle size information can be interpreted as a measure of tissue loss due to cerebral atrophy progression.

A number of studies have been successfully conducted which implements morphological filtering in connection to medical imaging. An amalgamation of iterative double automated thresholding and morphological filtering (MF) for early detection of cerebral aneurism (CA) is demonstrated [24] in which outgrowth of blood vessel is segregated by applying MF on the thresholded DSA binary images. Higher order fuzzy algorithms and nature inspired optimization methods have been successfully implemented for image segmentation [25-28]. Huang et al. [29] proposed a fuzzy model to access the indication of dementia depending on magnetic resonance imaging. Hanung Adi Nugroho et al. [30] proposed and implemented a neutrosophic and fuzzy c-means clustering algorithm for segmentation of contrast enhanced ultrasound image.

## 2.2 Fuzzy Theory based Image Classification Methods

There are a number of recent advancements in fuzzy clustering method for segmentation of

digital image object [31-33]. A sparse representation method and *K-SVD* dictionary learning algorithm is implemented for segmenting MRI scans in [32]. For better accuracy in initial clustering approximation of fuzzy c-means clustering, validity index has been redefined and modified by Xie and Beni [34], Bensaid [35] and Ren et al. [36].

An edge detection technique based on a universal gravity based method was discussed in [37] where pixel intensity is considered as gravitational mass. One novel amalgamation technique for early detection of cerebral aneurism was described in [38] which employ iterative double automated thresholding and morphological filtering with appropriate selection of structuring element (SE).

Another modified universal gravity law based edge detection algorithm is proposed by Malina et al. [39]. In this paper multiple prototypes of triangular norms have been studied on extracted fuzzy membership degree of resultant individual pixel gravitational force. In regard, Butkiewicz [40] had described the correlation property between different fuzzy variables. Advanced fuzzy theory have subsequently been implemented in edge detection for more distinct and accurate results. Melin et al. has described an edge detection technique based on generalized type-2 fuzzy logic and morphological gradient [41] in which the theory of alpha planes has been incorporated over type-2 fuzzy logic.

Clustering is a widely used tool that helps to segregate patterns or objects based on similarity measures [42, 43]. Fuzzy based clustering algorithms are successfully applied for medical image analysis [44 - 48]. The application scope of *K*-means clustering algorithm and atlas-guided approaches for segmenting the brain MRI scans have been discussed in [44]. Fuzzy c-means (FCM) is considered as a noise free efficient clustering algorithm which is based on fuzzy logic [49, 50]. The most commonly used analytical fuzzy c-means clustering is proposed by Bezdek's [49]. The fuzzy c-means uses probabilistic constraint term over the membership function so that the sum of all membership function is equal to 1.

It is observed that when data is acquired or transmitted from one entity to other, there is a higher probability of distortion. Due to this, there are chances of intervening noise or outliers which

bring challenges to traditional FCM algorithm. Consequently, a number of modified versions of FCM was introduced in the literature amongst which possibilistic c-means (PCM) is well known [51, 52]. PCM is sensitive to initialization and it clusters the data points on the basis of possibility of the membership function belonging to the cluster [53]. Pal *et al*. introduced a hybrid possibilistics fuzzy c-means algorithm (PFCM) [54] which is a combination of possibilistic c-means (PCM) and fuzzy c-means algorithm. PFCM is less sensitive to noise where partitioning is carried out not only on the basis of membership but also with possibilities.

Sparsity on the membership matrix of PCM is imposed by an algorithm known as sparsity-aware possibilisctics clustering method (SPCM), proposed in [55]. SPCM is capable to measure cluster centers with more precision. Car *et al*. [56] proposed fast generalized fuzzy c-means method (FGFCM), which improves the clustering by introducing local similarity measure. Later Zhu *et al*. [57] proposed a clustering algorithm by improving the fuzzy partition matrix named GIFP_FCM. This algorithm is suitable to provide good performance during segmentation of noisy images.

The elimination of noise interventions was a point of interest for justified reasons. The inclusion of neighbor information constraint into FCM used to be initiated both for enhanced clustering accuracy and elimination of noise. Ahmed *et al*. [58] proposed FCM for bias field estimation algorithm (BCFCM) by influencing neighbor information constraint in the objective function. This method is more immune to noise compared to FCM. The BCFCM is successfully implemented for segmentation of brain MRI data. FCM_S1 and FCM_S2 are two variations of FCM_S [59]. However, the parameter selection is very challenging in FCM_S method.

Krinidis and Chatazis [31] proposed robust fuzzy logical information c-means method (FLICM) which is very effective for image corrupted by noise or outliers. Zhang *et al*. [46] proposed another algorithm based on adaptive fuzzy logical c-means (ADFLICM) for the purpose of remotely sensed imagery classification. ADFLICM is designed for decreasing the edge blurring artifact and handling noise. FLICM is also able to achieve considerable results in case of noisy data. FLICM is associated with a fuzzy factor which is related to the cluster centers and

membership in each iterative step. Another kernel version of FLICM is proposed by Gong *et al*. [60] named KWFLICM which is unstable and time consuming.

Zhao [61] proposed an algorithm called Kernel generalized fuzzy c-means (KGFCM) clustering with spatial information for segmentation (KGFCM). This algorithm can improve the performance of GIFP_FCM proposed in [57]. Again KGFCM could be further modified to its advanced versions KGFCM_S1 and KGFCM_S2 by considering its neighbor information. These techniques are robust to noise but they are sensitive to parameter selection. The KGFCM is successfully implemented for different noisy images including MRI data in [61]. Gu *et al*. [62] proposed another method for detection of noise by using noise detecting fuzzy c-means algorithm (NDFCM). NDFCM method used two image filtering methods for removal of the noise. Its noise level is considered in each local window of NDFCM. But the performance of NDFCM solely depends on the selection of the parameters. Zhao *et al*. [63] proposed neighborhood weighted fuzzy c-means method (NWFCM). In this algorithm, they used Euclidean distance in FCM with neighborhood weighted distance. NWFCM is immune to noise but the computational cost is very high. The method is applied for segmentation of rician noise induced brainweb T1-weighted MR images in [63]. Lei *et al*. [64] proposed an algorithm called fast and robust fuzzy c-means clustering (FRFCM). It considers membership filtering and morphological reconstruction for its inherent mode of operation. This algorithm is simple, fast and also efficient for noisy image segmentation.

Gu *et al*. [47] proposed fuzzy double c-means method (FDCM) by introducing sparse in FCM. FDCM is able to handle data-set with different dimensions simultaneously. However the computational cost is very high for FDCM. Y Zhang [33] proposed deviation sparse fuzzy c-means (DSFCM) and a neighbor information based DSFCM (DSFCM_N) algorithm in which spatial correlation is considered. But the gross and overexerted estimation of neighbor information does not seem to meet sufficient clustering accuracy.

There are several improvements in the implementation of interval type-2 fuzzy FIS with the incorporation of genetic algorithm [65], evolutionary computation [66] and so on [67, 68]. Nature inspired optimization techniques have been widely implemented in the field of image

segmentation [69 - 71] of late. In recent times, information theoretic learning based discriminative segmentation algorithm for brain MRI impression is proposed by Kong et al. [72], whereas a minimal path propagation technique with backtracking approach has been introduced in [73] to extract curve like geometric structures which can be potentially implemented for brain image segmentation purpose. Deng and his co-workers have presented a fusion method between hierarchical deep neural network and fuzzy system to form dataset to be classified [74]. The authors have successfully implemented fuzzy based deep learning algorithm to classify brain MRI scans which contain high level of uncertainty.

The automatic diagnostics of AD patients to distinguish with different degrees of mental impairment is considered as a major challenge. Support vector machine classifier was applied on features obtained from volumetric measurements of hippocampus [75] and other brain areas [76]. Recently multiple deep-learning algorithms have been implemented to this task. Gupta et al. [77] implemented a pretraining method based on a sparse autoencoder to execute classification on the Alzheimer's Disease Neuroimaging Initiative (ADNI) dataset. Hon and Khan [78] successfully implemented advanced architectures such as VGG (Simonyan and Zisserman [79]) and Inception Net (Szegedy et al. [80]) on the OASIS dataset (Marcus et al. [81]), choosing the most information contained slice sections in the 3D impressions based on image entropy. Valliani and Soni [82], demonstrated that a ResNet (He et al. [83]) imposed on ImageNet (Deng et al. [84]) performed better than a baseline 2D CNN. Hosseini-Asl et al. [85] showed a 3D CNN architecture on ADNI and the CAD Dementia challenge (Bron et al. [86]) data set. Cheng et al. [87] presented a more computationally-efficient method based on long 3D patches produced by individual CNNs, which are further combined by an additional CNN to process the output. Lian et al. [88] impemented a related hierarchical CNN algorithm that automatically segregrate the significant patches. Khvostikov et al. [89] applied Siamese network to distinguish regions of interest (ROI) around the hippocampus fusing data set from multiple imaging modalities. As described in a relevant review article, Wen et al. [90], several existing works suffer from data leakage for flawed data splits, biased transfer learning rate, or the absence of independent test set. The report also shows that, in the absence of data leakage, CNNs achieve an impressive accuracy of 72-86% when distinguishing between healthy controls (HC) and AD. In a similar study, Fung et al. [91] showed the effect of multiple data-splitting methods on classification

accuracy. Bäckström et al. [92] also reported the effect of splitting methods and reported indistinguishable outcomes for two-way classification.

## 2.3 Advanced Methods of Image Classification

Predicting MCI by analysis of MRI is being practiced for a long time by researchers so that medication and precautionary measures can be initiated as early as possible. In this context the resting state functional MRI (Rf-MRI) analysis is a state of the art tool for assessment of MCI Progression [93 - 97]. Using BOLD (blood oxygen-level-dependent) signal based Rf-MRI data analysis; several learning based methods have been adopted for automated detection of AD [98, 99]. These techniques mainly use Pearson's correlation coefficient based functional connectivity (FC) assessment to model the temporal relationship between different region of interests (ROIs). These methods are mostly developed by considering FC as a stationary entity throughout the fMRI acquition process. Some recent studies demonstrates that FC in human brain is not a static rather dynamic parameter [100, 101]. Hence several new efforts have been made towards dynamic connectivity analysis which are focused to model local temporal dynamic property and local spatial dependency. Further the algorithms are developed for local-to-local and local-to-global spatial-temporal dependency model which might help to trace the change in brain networks [102]. In addition to FC, a different approach named network hub connectivity biomarker is used to find out the communication and information integration among different regions of brain [103 - 105]. Some recent studies show that progression of AD like neurodegenerative diseases significantly affects the activity of different functional hub regions in human brain and Consequent abnormality is observed in brain network connectivity [106 - 108]. In order to find out the functional connectivity between different brain regions, a deep learning based technique using Pearson's correlation is implemented by Ju *et.al* [109].
 Further a deep learning based method, i.e., Spatial Temporal convolutional-recurrent neural Network (STNet) is also demonstrated in [110]. This technique models the whole brain temporal sequences in dynamic FC patterns for identification of MCI.

The MCI is recognized as gradual shrinkage of the hippocampus in medial temporal lobe (MTL) [111]. Hippocampus is structurally heterorogenious in nature which is constructed of dentate gyrus (DG), cornu ammonis (CA) 1-4, presubiculum, subiculum, prosubiculum, parasubiculum

and uncus. Hippocampus is responsible for long term memory and emotional responses where gradual tissue loss is observed with progression of MCI [112, 113]. The source of the canonical tri-synaptic pathway is the entorhinal cortex (ENT), which is the primary input to the hippocampus. Anatomical evidence reveals that hippocampus-associated regions including the ENT, perirhinal (PRC), posterior parahippocampal (PHC) and retrosplenial (RSC) cortices interact with hippocampal subfields directly, avoiding the canonical hippocampal passageway in both non-human primates [114 - 117] and rodents [118]. Parahippocampal gyrus is a section of grey matter cortical region which is surrounded by the hippocampus. The hippocampus associated parahippocampus plays a major role in memory retrieval and memory encoding.

The hippocampal-parahippocampal associative in vivo framework in human brain can be studied by characterizing the acquired Rf-MRI FC to reveal the MCI progression. In this context the anatomical pathways are often reflected by Rf-MRI FC [119]. Due to technical challenges inherent to human hippocampal subfield modeling by using MRI, only a few numbers of studies have been reported. Additionally there is no systematic study of FC between different ROI subfields.

Several correlation coefficient based dynamic learning methods are examined to model spatial-temporal dependency changes in functional brain networks [120]. Network hub connectivity biomarker is also implemented to extract communication and information integration among different ROIs by using BOLD (blood oxygen-level-dependent) signal [121 - 123]. In some recent studies the FC of each human hippocampal subfield along with longitudinal axis and anterior-posterior axis has been systematically characterized [124]. In connection to this, several advanced deep-learning based algorithms have been recently implemented for the early detection of Alzheimer's disease [125 - 127].

# REFERENCES

[1]    A. Burns and S. Iliffe, "Alzheimer's disease. bmj 338, b158," 2009.

[2]    W. H. Organization et al., "Dementia: Fact sheet no. 362. 2017," WHO. Available online at: http://www. who. int/mediacentre/factsheets/fs362/en/. Accessed, vol. 2, 2017.

[3]    S. Gauthier, B. Reisberg, M. Zaudig, R. C. Petersen, K. Ritchie, K. Broich, S. Belleville, H. Brodaty, D. Bennett, H. Chertkow, et al., "Mild cognitive impairment," The lancet, vol. 367, no. 9518, pp. 1262– 1270, 2006.

[4]    J. Bischkopf, A. Busse, and M. Angermeyer, "Mild cognitive impairment 1–a review of prevalence, incidence and outcome according to current approaches," Acta Psychiatrica Scandinavica, vol. 106, no. 6, pp. 403– 414, 2002.

[5]    C. Misra, Y. Fan, and C. Davatzikos, "Baseline and longitudinal patterns of brain atrophy in mci patients, and their use in prediction of shortterm conversion to ad: results from adni," Neuroimage, vol. 44, no. 4, pp. 1415–1422, 2009.

[6]    Y Noh *et al.*, "Anatomical heterogeneity of Alzheimer disease: based on cortical thickness on MRIs", *Neurology*, vol. 83, pp. 1936–1944, 2014.

[7]    D. Ferreira et al., "Distinct subtypes of Alzheimer's disease based on patterns of brain atrophy: longitudinal trajectories and clinical applications", Nature Neuroscience, 2017.

[8]    B. Singh, M. M. Mielke, A. K. Parsaik, R. H. Cha, R. O. Roberts, P. D. Scanlon, Y. E. Geda, T. J. Christianson, V. S. Pankratz, and R. C. Petersen, "A prospective study of chronic obstructive pulmonary disease and the risk for mild cognitive impairment," JAMA neurology, vol. 71, no. 5, pp. 581–588, 2014.

[9]    J. J. Hsiao and E. Teng, "Depressive symptoms in clinical and incipient alzheimer's disease," Neurodegenerative disease management, vol. 3, no. 2, pp. 147–155, 2013.

[10]   V. Torre, T A Poggio, "On edge detection", IEEE Trans. Pattern Anal. Mach. Intell., vol. PAMI-8, no. 6, pp. 147–163, 1986.

[11]   M. Setayesh, M. Zhang, M. Johnston, "Effects of static and dynamic topologies in particle swarm optimization for edge detection in noisy images", Proc. IEEE Congr. Evol. Comput., pp. 1–8, 2012.

[12]   R. C. Gonzalez, Richard E. Woods, Digital Image Processing, 3$^{rd}$ ed., Pearson India.

[13]   W. Gao, L. Yang, X. Zhang, H. Liu, "An Improved Sobel Edge Detection", IEEE 3$^{rd}$ International Conference on Innovative Computing Technologies (ICICT), vol. 5, pp. 67-71, 2010.

[14]   J. Canny, "A computational approach to edge detection", IEEE Trans. Pattern Anal. Mach. Intell., vol. PAMI-8, no. 6, pp. 679–698, 1986.

[15]   J M S Prewitt, "Object enhancement and extraction", Picture Analysis and Psychopictorics, B. S. Lipkin and A. Rosenfeld, Eds. New York,NY, USA: Academic, pp. 75–149, 1970.

[16]   M. Basu, "Gaussian Based Edge Detection Methods: A Survey", IEEE Trans. On systems, man and cybernetics, vol. 32, no. 3, pp. 252 – 260, 2002.

[17]   R. A. Salinas, C. Richardson, M. A. Abidi and R. C. Gonzalez, "Data Fusion: Color edge detection and surface reconstruction through regularization", IEEE Trans. on Industrial Electronics, vol. 43, no. 3, pp. 355-363, 1996.

[18]   P. Perona, J. Malik, "Scale-space and edge detection using anisotropic diffusion", IEEE Trans. On Pattern Analysis and Machine Intelligence, vol. 12, no. 7, pp. 629-639, 1990.

[19]   M. E. Murray, N. R. Graff-Radford, O. A. Ross, R. C. Petersen, R. Duara, and D. W. Dickson, "Neuropathologically defined subtypes of Alzheimer's disease with distinct clinical characteristics: a retrospective study," Lancet. Neurol, vol. 10, no. 9,pp.785–796, 2011.

[20]   J. L. Whitwell, D. W. Dickson, M. E. Murray, S. D. Weigand, N. Tosakulwong, M. L. Senjem *et al.* "Neuroimaging correlates of pathologically defined subtypes of Alzheimer's disease: a case-control study." *Lancet. Neurol.*, vol. 11, no. 10, pp. 868–877, 2012.

[21]   J. L. Whitwell, C. R. Jr. Jack, S. A. Przybelski, J. E. Parisi, M. L. Senjem, B. F. Boeve.*et al.* *"*Temporoparietal atrophy: a marker of AD pathology independent of clinical diagnosis," Neurobiol. Aging, vol. 32, no. 9, pp. 1531–1541, 2011.

[22]   D. Ferreira, C. Verhagen, J. A. Hernandez-Cabrera, L. Cavallin, C. J. Guo, U. Ekman.et al., "Distinct subtypes of Alzheimer's disease based on patterns of brain atrophy: longitudinal trajectories and clinical applications," Nature Neuroscience, DOI: 10.1038/srep46263., 2017.

[23] S. M. Nestor, R. Rupsingh, M. Borrie, M. Smith, V. Accomazzi, J. L. Wells. et al., "Ventricular Enlargement as a possible measure of alzheimer's disease progression validated using the Alzheimer's disease neuroimaging initiative database," Brain, vol. 131, no. 9, pp. 2443-2454, 2008.

[24] A. Chandra and S. Mondal, "Amalgamation of iterative double automated thresholding and morphological filtering for early detection of cerebral aneurism," Multimedia tools and Application, Springer, vol. 76, no. 22, pp. 23957–23979, 2017.

[25] P. Melin, O. Mendoza, and O. Castillo, "An improved method for edge detection based on interval type-2 fuzzy logic," Expert Syst. Appl., vol. 37, no. 12, pp. 8527-8535, 2010.

[26] M. Setayesh, M. Zhang and M. Johnston, "A novel particle swarm optimization approach to detecting continuous, thin and smooth edges in noisy images," *Information Sciences*, vol. 246, pp. 28-51, 2013.

[27] O. P. Verma and Anil Singh Parihar, "An optimal fuzzy system for edge detection in color images using bacterial foraging algorithm," IEEE Transactions on fuzzy systems, vol. 25, no. 1, pp. 114-127, 2017.

[28] P. Melin, C. I. Gonzalez, J. R. Castro, O. Mendoza, and O. Castillo, "Edge detection method for image processing based on generalized type-2 fuzzy logic," IEEE Transactions on Fuzzy Systems, vol. 22, no.6, pp. 1515-1525, 2014.

[29] Yo-Ping Huang, B-X. Yang, S. Zaza, and W-H Liu, "A fuzzy approach to assess the indication of dementia based on magnetic reasoning imaging", International Conference on fuzzy theory and it's applications, National Taiwan University of Technology, Taipei, Taiwan, Dec 6-8, pp. 328-333, 2013.

[30] H. A. Nugroho, M. Rahmawaty, Y. Triyani, and I. Ardiyanto, "Neutrosophic and Fuzzy C-Means Clustering for Breast Ultrasound Image Segmentation," 9[th]Internatiional Conference on Information Technology and Electrical Engineering (ICITEE), Phuket, Thailand, pp. 1-5, 2017.

[31] S. Krinidis and V.Chatzis, "A robust fuzzy local information C-means clustering algorithm," IEEE Transactions on Image Processing, vol. 19, no. 5, pp. 1328-1337, May 2010.

[32] A. Julazadeh, J. Alirezaie, and P. Babyn, "A novel automated approach for segmenting lateral ventricle in MR images of the brain using sparse representation and dictionary learning," 11th International conference on Information Science, Signal Processing and their applications(ISSPA), pp. 888-893, 2012.

[33] Y. Zhang, X. Bai, R. Fan, and Z. Wang, "Deviation-sparse fuzzy C-means with neighbor information constraints," IEEE Transactions on Fuzzy Systems, vol. 27, no. 1, pp.185-199, January 2019.

[34] X. L. Xie and G. Beni, "A validity measure for fuzzy clustering," IEEE Transactions on Pattern Analysis and Machine Intelligence, vol. 13, no. 8, pp. 841–847, 1991.

[35] A. M. Bensaid, L. O. Hall, J. C. Bezdek, L. P. Clarke, M. L. Sibiger, J. A. Arrington et al., "Validity-guided (re)clustering with applications to image segmentation," IEEE Trans on Fuzzy Sys, vol. 4, no. 2, pp. 112–123, 1996.

[36] M. Ren, P. Liu, Z. Wang and J. Yi, "A self-adaptive fuzzy c-means algorithm for determining optimal number of clusters," Computational Intelligence and Neuroscience *2016*, Hindawi, 2016.

[37] G. Sun, Liu Qinhuo, Liu Qiang, C. Ji and X. Li, "A novel approach for edge detection based on the theory of universal gravity", Pattern Recognition, vol. 40, pp. 2766-2775, 2007.

[38] A. Chandra, S. Modal. "Amalgamation of iterative double automated thresholding and morphological filtering: A new proposition in the early detection of cerebral aneurysm", Multimedia Tools and Applications. Springer, vol.76, no.22, pp. 23957–23979, 2017.

[39] C. L. Molina, H. Bustince H, J. Fernandez, P. Couto and B. De Baets, "A gravitational approach to edge detection based on triangular norms", Pattern Recognition, vol. 43, pp. 3730-3741, 2010.

[40] B. S. Butkiewicz, "Fuzzy Approach to Correlation Function", Warsaw University of Technology, Warsaw, Poland.

[41] P. Melin et al., "Edge detection method for image processing based on Generalized Type-2 fuzzy logic", IEEE Transactions on Fuzzy Systems, vol. 22, pp. 1515-1525, 2014.

[42] X. Mu˜noz, J. Freixenet, X. Cufı, and J. Martı, "Strategies for image segmentation combining region and boundary information," Pattern recognition letters, vol. 24, no. 1-3, pp. 375–392, 2003.

[43] A. Baraldi and P. Blonda, "A survey of fuzzy clustering algorithms for pattern recognition. i," IEEE Transactions on Systems, Man, and Cybernetics, Part B (Cybernetics), vol. 29, no. 6, pp. 778–785, 1999.

[44] D. L. Pham, C. Xu, and J. L. Prince, "Current methods in medical image segmentation," Annual review of biomedical engineering, vol. 2, no. 1, pp. 315–337, 2000.

[45] Y. Guo, L. Jiao, S. Wang, S. Wang, F. Liu, and W. Hua, "Fuzzy super pixels for polarimetric sar images classification," IEEE Transactions on Fuzzy Systems, vol. 26, no. 5, pp. 2846–2860, 2018.

[46]   H. Zhang, Q. Wang, W. Shi, and M. Hao, "A novel adaptive fuzzy local information c-means clustering algorithm for remotely sensed imagery classification," IEEE Transactions on Geoscience and Remote Sensing, vol. 55, no. 9, pp. 5057–5068, 2017.

[47]   J. Gu, L. Jiao, S. Yang, and F. Liu, "Fuzzy double c-means clustering based on sparse self-representation," IEEE Transactions on Fuzzy Systems, vol. 26, no. 2, pp. 612–626, 2017.

[48]   X. Bai, Y. Wang, H. Liu, and S. Guo, "Symmetry information based fuzzy clustering for infrared pedestrian segmentation," IEEE Transactions on Fuzzy Systems, vol. 26, no. 4, pp. 1946–1959, 2017.

[49]   J. C. Bezdek, Pattern recognition with fuzzy objective function algorithms, Springer Science & Business Media, 2013.

[50]   L. A. Zadeh, "Fuzzy sets," Information and control, vol. 8, no. 3, pp. 338–353, 1965.

[51]   R. Krishnapuram and J. M. Keller, "A possibilistic approach to clustering," IEEE transactions on fuzzy systems, vol. 1, no. 2, pp. 98–110, 1993.

[52]   R. Krishnapuram and J. M. Keller, "The possibilistic c-means algorithm: insights and recommendations," IEEE transactions on Fuzzy Systems, vol. 4, no. 3, pp. 385–393, 1996.

[53]   S. Theodoridis and K. Koutroumbas, "Pattern recognition. 2003," Google Scholar Digital Library, 2009.

[54]   N. R. Pal, K. Pal, J. M. Keller, and J. C. Bezdek, "A possibilistic fuzzy c-means clustering algorithm," IEEE transactions on fuzzy systems, vol. 13, no. 4, pp. 517–530, 2005.

[55]   S. D. Xenaki, K. D. Koutroumbas, and A. A. Rontogiannis, "Sparsity-aware possibilistic clustering algorithms," IEEE Transactions on Fuzzy Systems, vol. 24, no. 6, pp. 1611–1626, 2016.

[56]   W. Cai, S. Chen, and D. Zhang, "Fast and robust fuzzy c-means clustering algorithms incorporating local information for image segmentation," Pattern recognition, vol. 40, no. 3, pp. 825–838, 2007.

[57]   L. Zhu, F.-L. Chung, and S. Wang, "Generalized fuzzy c-means clustering algorithm with improved fuzzy partitions," IEEE Transactions on Systems, Man, and Cybernetics, Part B (Cybernetics), vol. 39, no. 3, pp. 578–591, 2009.

[58]   M. N. Ahmed, S. M. Yamany, N. Mohamed, A. A. Farag, and T. Moriarty, "A modified fuzzy c-means algorithm for bias field estimation and segmentation of mri data," IEEE transactions on medical imaging, vol. 21, no. 3, pp. 193–199, 2002.

[59]   S. Chen and D. Zhang, "Robust image segmentation using fcm with spatial constraints based on new kernel-induced distance measure," IEEE Transactions on Systems, Man, and Cybernetics, Part B (Cybernetics), vol. 34, no. 4, pp. 1907–1916, 2004.

[60]   M. Gong, Y. Liang, J. Shi, W. Ma, J. Ma, "Fuzzy c-means clustering with local information and kernel metric for image segmentation", IEEE Trans. Image Process. Vol. 22, no. 2, pp. 573–584, 2012.

[61]   F. Zhao, L. Jiao, H. Liu, "Kernel generalized fuzzy c-means clustering with spatial information for image segmentation", Digit. Signal Process, Vol. 23, no. 1, pp. 184-199. 2013.

[62]   F. F. Guo, X. X. Wang, J. Shen, "Adaptive fuzzy c-means algorithm based on local noise detecting for image segmentation", IET Image Process, vol. 10, no. 4, pp. 272-279, 2016.

[63]   Z. Zaixin, C. Lizhi, C. Guangquan, "Neighbourhood weighted fuzzy c- means clustering algorithm for image segmentation", IET Image Processing. Vol. 8, no. 3, pp. 150-161, 2013.

[64]   T. Lei, X. Jia, Y. Zhang, L. He, H. Meng, A. K. Nandi, "Significantly fast and robust fuzzy c-means clustering algorithm based on morphological reconstruction and membership filtering", IEEE Trans. on Fuzzy Systems. Vol. 26, no. 5, pp. 3027-3041, 2018.

[65]   S. Chen, Y. Chang, J. Pan, "Fuzzy rules interpolation for sparse fuzzy rule-based systems based on interval type-2 Gaussian fuzzy sets and genetic algorithms", IEEE Trans. Fuzzy Syst., vol. 21, no. 3, pp. 412–425, 2013.

[66]   C. Hsu, C. Juang, "Evolutionary robot wall-following control using type-2 fuzzy controller with species-DE-activated continuous ACO", IEEE Trans. Fuzzy Syst., vol. 21, no. 1, pp. 100–112, 2013.

[67]   H. Zhou, H. Ying, "A method for deriving the analytical structure of a broad class of typical interval type-2 Mamdani fuzzy controllers, IEEE Trans. Fuzzy Syst., vol. 21, no. 3, pp. 447–458, 2013.

[68]   X. J. Li, G. H. Yang, "Switching-type H∞filter design for T–S fuzzy systems with unknown or partially unknown membership functions", IEEE Trans. Fuzzy Syst., vol. 21, no. 2, pp. 385–392, 2013.

[69]   M. Setayesh, M. Zhang, M. Johnston, "A novel particle swarm optimization approach to detecting continuous, thin and smooth edges in noisy images", Information Sciences, vol. 246, pp. 28-51, 2013.

[70]   S. A. Etemad, T. White, "An ant-inspired algorithm for detection of edge features", Applied Soft Computing, vol. 11, pp. 4883-4893, 2011.

[71]   O. P. Verma and A. S. Parihar , "An optimal fuzzy system for edge detection in color images using bacterial foraging algorithm", IEEE Transactions on fuzzy systems, vol. 25, pp. 114-127, 2017.

[72]     Y. Kong, Y. Deng and Q. Dai, "Discriminative clustering and feature selection for brain MRI segmentation", IEEE Signal Processing Letters, vol.22, no.5, pp. 573-577, 2015.

[73]     Y. Chen *et al.*, "Curve-like structure extraction using minimal path propagation with backtracking", IEEE Transactions on Image Processing, vol.25, no.2, pp. 988-1003, 2016.

[74]     Y. Deng, Z. Ren, Y. Kong, F. Bao and Q. Dai, "A hierarchical fused fuzzy deep neural network for data classification," IEEE Transactions on Fuzzy Systems, vol.25, no.4, pp. 1006-1012, 2017.

[75]     G. Emilie, C. Gaël *et al*. "Multidimensional classification of hippocampal shape features discriminates Alzheimer's disease and mild cognitive impairment from normal aging", Neuroimage, vol. 47, no. 4, pp.1476–1486, 2009.

[76]     P. Claudia, J. T. Stefan *et al.*, "Automated detection of brain atrophy patterns based on MRI for the prediction of Alzheimer's disease". Neuroimage, vol. 50, no. 1, pp. 162–174, 2010.

[77]     A. Gupta, M. Ayhan, and A. Maida. "Natural image bases to represent neuroimaging data", In International conference on machine learning, pp. 987–994, 2013.

[78]     M. Hon and N. Mefraz Khan, "Towards Alzheimer's disease classification through transfer learning", In 2017 IEEE International Conference on Bioinformatics and Biomedicine (BIBM), pp. 1166–1169. IEEE, 2017.

[79]     K. Simonyan and A. Zisserman, "Very deep convolutional networks for large-scale image recognition". arXiv preprint arXiv:1409.1556, 2014.

[80]     C. Szegedy, W. Liu, Y. Jia, P. Sermanet, S. Reed, Dragomir Anguelov, Dumitru Erhan, Vincent Vanhoucke, and Andrew Rabinovich, "Going deeper with convolutions", In Proceedings of the IEEE conference on computer vision and pattern recognition, pp. 1–9, 2015.

[81]     D. S. Marcus, A. F. Fotenos, J. G. Csernansky, J. C. Morris, and R. L. Buckner, "Open access series of imaging studies: longitudinal MRI data in nondemented and demented older adults", Journal of cognitive neuroscience, vol. 22, no.12, pp.2677–2684, 2010.

[82]     A. Valliani and A. Soni. Deep residual nets for improved Alzheimer's diagnosis. In BCB, page 615, 2017.

[83]     K. He, X. Zhang, S. Ren, and J. Sun, "Deep residual learning for image recognition", In Proceedings of the IEEE conference on computer vision and pattern recognition, pp. 770–778, 2016.

[84]     J. Deng, W. Dong, R. Socher, Li-Jia Li, Kai Li, and Li Fei-Fei. Imagenet: A large-scale hierarchical image database. In 2009 IEEE conference on computer vision and pattern recognition, pp. 248–255. IEEE, 2009.

[85]     E. Hosseini-Asl, G. Gimel'farb, and A. El-Baz, "Alzheimer's disease diagnostics by a deeply supervised adaptable 3D convolutional network", arXiv preprint arXiv:1607.00556, 2016.

[86]     E. E. Bron, M. Smits *et al*. "Standardized evaluation of algorithms for computer-aided diagnosis of dementia based on structural MRI: the caddementia challenge", NeuroImage, vol. 111, pp. 562–579, 2015.

[87]     D. Cheng, M. Liu, J. Fu, and Y. Wang, "Classification of MR brain images by combination of multi-CNNs for AD diagnosis", "Ninth International Conference on Digital Image Processing (ICDIP 2017), vol. 10420, page 1042042. International Society for Optics and Photonics, 2017.

[88]     C. Lian, M. Liu, J. Zhang, and D. Shen, "Hierarchical fully convolutional network for joint atrophy localization and Alzheimer's disease diagnosis using structural MRI", IEEE transactions on pattern analysis and machine intelligence, vol. 42, no. 4, pp. 880- 893, 2020.

[89]     A. Khvostikov, K. Aderghal, J. Benois-Pineau, A. Krylov, and G. Catheline, "3D CNN-based classification using sMRI and MD-DTI images for Alzheimer disease studies", arXiv preprint arXiv:1801.05968, 2018.

[90]     J. Wen, E. Thibeau-Sutre *et al*., "Convolutional neural networks for classification of Alzheimer's disease: Overview and reproducible evaluation", Medical image analysis, vol. 63, pp. 101694, 2020.

[91]     Y. Ren Fung, Z. Guan, R. Kumar, J. Y. Wu, and M. Fiterau, "Alzheimer's disease brain MRI classification: Challenges and insights", arXiv:1906.04231, 2019.

[92]     Karl Bäckström, Mahmood Nazari, Irene Yu-Hua Gu, and Asgeir Store Jakola. An efficient 3D deep convolutional network for Alzheimer's disease diagnosis using MR images. In 2018 IEEE 15th International Symposium on Biomedical Imaging (ISBI 2018), pp. 149–153. IEEE, 2018.

[93]     S. Rombouts, F. Barkhof, C. Van Meel, and P. Scheltens, "Alterations in brain activation during cholinergic enhancement with rivastigmine in Alzheimer's disease," Journal of Neurology, Neurosurgery and Psychiatry, vol. 73, no. 6, pp. 665–671, 2002.

[94]     J. S. Damoiseaux, "Resting-state fMRI as a biomarker for Alzheimer's disease", Alzheimer's Research and Therapy, vol. 4, no. 8, pp. 1–2, 2012.

[95]     M. Machulda, H. Ward, B. Borowski, J. Gunter, R. Cha, P. Obrien, R. Petersen, B. Boeve, D. Knopman, D. Tang-Wai et al., "Comparison of memory fMRI response among normal, MCI, and Alzheimer's patients," Neurology, vol. 61, no. 4, pp. 500–506, 2003.

[96] B. Jie, D. Zhang, W. Gao, Q. Wang, C.-Y. Wee, and D. Shen, "Integration of network topological and connectivity properties for neuroimaging classification," IEEE Transactions on Biomedical Engineering, vol. 61, no. 2, pp. 576–589, 2013.

[97] C.-Y. Wee, P.-T. Yap, D. Zhang, L. Wang, and D. Shen, "Groupconstrained sparse fMRI connectivity modeling for mild cognitive impairment identification," Brain Structure and Function, vol. 219, no. 2, pp. 641–656, 2014.

[98] B. Jie, M. Liu, D. Zhang, and D. Shen, "Sub-network kernels for measuring similarity of brain connectivity networks in disease diagnosis," IEEE Transactions on Image Processing, vol. 27, no. 5, pp. 2340–2353, 2018.

[99] M. Wang, D. Zhang, J. Huang, P.-T. Yap, D. Shen, and M. Liu, "Identifying autism spectrum disorder with multi-site fMRI via low-rank domain adaptation," IEEE Transactions on Medical Imaging, vol. 39, no. 3, pp. 644-655, 2019.

[100] J. Zhang, W. Cheng, Z. Liu, K. Zhang, X. Lei, Y. Yao, B. Becker, Y. Liu, K. M. Kendrick, G. Lu et al., "Neural, electrophysiological and anatomical basis of brain-network variability and its characteristic changes in mental disorders," Brain, vol. 139, no. 8, pp. 2307–2321, 2016.

[101] R. M. Hutchison, T. Womelsdorf, E. A. Allen, P. A. Bandettini, V. D. Calhoun, M. Corbetta, S. Della Penna, J. H. Duyn, G. H. Glover, J. Gonzalez-Castillo et al., "Dynamic functional connectivity: Promise, issues, and interpretations," NeuroImage, vol. 80, pp. 360–378, 2013.

[102] S. Si, B. Wang, X. Liu, C. Yu, C. Ding, and H. Zhao, "Brain network modeling based on mutual information and graph theory for predicting the connection mechanism in the progression of Alzheimer's disease," Entropy, vol. 21, no. 3, p. 300, 2019.

[103] M. P. van den Heuvel and O. Sporns, "Network hubs in the human brain," Trends in Cognitive Sciences, vol. 17, no. 12, pp. 683–696, 2013.

[104] Z. J. Dai, Y. C. Bi, and Y. He, "With great brain hub connectivity comes great vulnerability," CNS Neuroscience and Therapeutics, vol. 21, no. 7, pp. 541–542, 2015.

[105] C. J. Stam, "Modern network science of neurological disorders," Nature Reviews Neuroscience, vol. 15, no. 10, pp. 683–695, 2014.

[106] R. L. Buckner, J. Sepulcre, T. Talukdar, F. M. Krienen, H. Liu, T. Hedden, J. R. Andrews-Hanna, R. A. Sperling, and K. A. Johnson, "Cortical hubs revealed by intrinsic functional connectivity: Mapping, assessment of stability, and relation to Alzheimer's disease," Journal of Neuroscience, vol. 29, no. 6, pp. 1860–1873, 2009.

[107] Z. Dai, C. Yan, K. Li, Z. Wang, J. Wang, M. Cao, Q. Lin, N. Shu, M. Xia, Y. Bi et al., "Identifying and mapping connectivity patterns of brain network hubs in Alzheimer's disease," Cerebral Cortex, vol. 25, no. 10, pp. 3723–3742, 2014.

[108] W. de Haan, K. Mott, E. C. van Straaten, P. Scheltens, and C. J. Stam, "Activity dependent degeneration explains hub vulnerability in Alzheimer's disease," PLoS Computational Biology, vol. 8, no. 8, pp. 1002582, 2012.

[109] R. Ju, C. Hu, p. zhou and Q. Li, "Early Diagnosis of Alzheimer's Disease Based on Resting-State Brain Networks and Deep Learning," in IEEE/ACM Transactions on Computational Biology and Bioinformatics, vol. 16, no. 1, pp. 244-257, 2019.

[110] M. Wang, C. Lian, D. Yao, D. Zhang, M. Liu and D. Shen, "Spatial-Temporal Dependency Modeling and Network Hub Detection for Functional MRI Analysis via Convolutional-Recurrent Network," in IEEE Transactions on Biomedical Engineering, vol. 67, no. 8, pp. 2241-2252, 2020.

[111] Y. Noh *et al.* Anatomical heterogeneity of Alzheimer disease: based on cortical thickness on MRIs. *Neurology* 83, 1936–1944, 2014.

[112] D. Ferreira et al., "Distinct subtypes of Alzheimer's disease based on patterns of brain atrophy: longitudinal trajectories and clinical applications," Nature Neuroscience, doi: 10.1038/srep46263., 2017.

[113] Whitwell, J. L. *et al. "*Temporoparietal atrophy: a marker of AD pathology independent of clinical diagnosis". *Neurobiol. Aging* 32, pp. 1531–1541, 2011.

[114] M.P. Witter and D.G. Amaral, "Entorhinal cortex of the monkey: V. Projections to the dentate gyrus, hippocampus, and subicular complex", Journal of Comparative Neurology, vol. 307, no. 3, pp.437-459, 1991.

[115] B. W. Leonard, D. G. Amaral, L. R. Squire, and S. Zola-Morgan, "Transient memory impairment in monkeys with bilateral lesions of the entorhinal cortex". Journal of Neuroscience, vol. 15, no. 8, pp.5637-5659, 1995.

[116]    J. P. Aggleton, "Multiple anatomical systems embedded within the primate medial temporal lobe: implications for hippocampal function". Neuroscience & Biobehavioral Reviews, vol. 36, no. 7, pp.1579-1596, 2012.

[117]    Y. Kobayashi and D. G. Amaral, "Macaque monkey retrosplenial cortex: III. Cortical efferents". Journal of Comparative Neurology, vol. 502, no. 5, pp. 810-833, 2007.

[118]    K. L. Agster and R. D. Burwell, "Hippocampal and subicular efferents and afferents of the perirhinal, postrhinal, and entorhinal cortices of the rat", Behavioural brain research, vol. 254, pp.50-64, 2013.

[119]    C. J. Honey, O. Sporns, L. Cammoun, X. Gigandet, J. P. Thiran, R. Meuli, and P. Hagmann, "Predicting human resting-state functional connectivity from structural connectivity", Proceedings of the National Academy of Sciences, vol. 106, no. 6, pp. 2035-2040, 2009.

[120]    S. Si, B. Wang, X. Liu, C. Yu, C. Ding, and H. Zhao, "Brain network modeling based on mutual information and graph theory for predicting the connection mechanism in the progression of Alzheimer's disease," Entropy, vol. 21, no. 3, pp. 300, 2019.

[121]    M. P. van den Heuvel and O. Sporns, "Network hubs in the human brain," Trends in Cognitive Sciences, vol. 17, no. 12, pp. 683–696, 2013.

[122]    Z. J. Dai, Y. C. Bi, and Y. He, "With great brain hub connectivity comes great vulnerability," CNS Neuroscience and Therapeutics, vol. 21, no. 7, pp. 541–542, 2015.

[123]    C. J. Stam, "Modern network science of neurological disorders," Nature Reviews Neuroscience, vol. 15, no. 10, pp. 683–695, 2014.

[124]    M. A. Dalton, C. McCormick, and E. A. Maguire, "Differences in functional connectivity along the anterior-posterior axis of human hippocampal subfields". NeuroImage, 192, pp.38-51, 2019.

[125]    S. Gao, D. Lima, "A review of the application of deep learning in the detection of Alzheimer's disease," International Journal of Cognitive Computing in Engineering, vol. 3, pp. 1-8, 2022.

[126]    V. Patil, M. Madgi, and A. Kiran, "Early prediction of Alzheimer's disease using convolutional neural network: a review," Egypt J Neurol Psychiatry Neurosurg, vol. 58, no. 1, pp. 1-10, 2022.

[127]    S. Katabathula, Q. Wang, and R. Xu, "Predict Alzheimer's disease using hippocampus MRI data: A lightweight 3D deep convolutional network model with visual and global shape representations," Alzheimers Research and Therapy, vol. 13, no. 1, pp. 104, 2021.

# Chapter 3

# A Novel Fuzzy Pixel Intensity Correlation Based Brain MRI Segmentation Algorithm

## 3.1 Introduction

This chapter presents a novel fuzzy segmentation algorithm for brain MRI images which produces improved outcomes. The test MRI scans are initially converted into gray scale images and followed by an implementation of structuring element for image opening. This process effectively enhances the contrast of all the boundary regions of brain which contains crucial information for mild cognitive impairment. A novel rule-base of higher order fuzzy system is presented which dynamically chooses edge pixels and accordingly segregates the next probable edge pixel. The advanced fuzzy inference system (FIS) is inspired by fuzzy connectedness algorithm and the FIS converts probable edge pixels into edge pixels depending on intensity correlation between ordered pixels. In support of designed rule-base, the presented algorithm further accumulates the edge pixels into an edge contour. The proposition is finally tested over several ADNI and real time brain MRI images of different subject and orientation. Experimental results show a promising improvement in MRI object boundaries detection and enhance image contrast both qualitatively and quantitatively.

## 3.2 Initial Works

Predicting brain diseases mostly relies on the analysis of brain images since it is considered to be most facile and non invasive study. Among many possible imaging techniques like computer tomography, magnetic resonance imaging and positron emission tomography; MRI is most promising brain imaging tool as it produces better contrast enhanced images. As different layers of overlapping cell types in different parts of human brain have non-identical responses in magnetic field of MRI, prominent edges are generally not obtained in MRI scans. This paper focuses on a novel edge detection technique specially designed for MRI brain scans.

A number of modified image processing techniques together with the novel proposition helps to achieve necessary edge enhancement for brain MRI scans. Associated techniques like *opening*, *morphological gradient*, *Fuzzy connectedness algorithm* and *Fuzzy pixel intensity correlation based segmentation algorithm* are subsequently introduced in this section with necessary mathematical illustration.

## 3.2.1   Pre-processing

All the input MRI scans are converted into corresponding gray scale image. The gray scale image $I$, thus received, can be expressed as [1, 2]:

$$I(i,j) = 0.299I_R(i,j) + 0.587I_G(i,j) + 0.114I_B(i,j) \ \forall i \in \{1,2,\dots,N_R\} \ and \ j \in \{1,2,\dots,N_C\}$$

$$(3.1)$$

where coefficients $I_R, I_G, I_B$ represent red, green and blue components of true colour (RGB) image respectively. $N_R \ and \ N_C$ symbolize the number of rows and columns present in the input image respectively. The hue and saturation information present in an RGB image are eliminated and luminance is conserved in (3.1).

## 3.2.2   Morphological Filtering

*Opening* and *closing* are two constituents of morphological filtering that are widely used to extract important features from digital images [1, 3]. The process of obtaining *opening* and *closing* is initiated with another two morphological processes namely *erosion* and *dilation*.

*Erosion* of test image $I$ by the proposed non-flat structuring element, $b_{NF}$ at any location (x, y) is given by [1]:

$$[I \ominus b_{NF}](x,y) = \min_{(s,t) \in b_{NF}} \{I(x+s,y+t) - b_{NF}(s,t)\}$$

$$(3.2)$$

Similarly, the *dilation* of image $I$ by the same SE at any arbitrary location (x, y) is given by:

$$[I \oplus b_{NF}](x,y) = \max_{(s,t) \in b_{NF}} \{I(x-s,y-t) + b_{NF}(s,t)\}$$

$$(3.3)$$

*Opening* and *closing* of gray scale test image $I$ is similar to *opening* and *closing* of binary image and can be written as:

$$[I \circ b_{NF}](x,y) = (I \ominus b_{NF}) \oplus b_{NF}$$

$$(3.4)$$

$$[I \bullet b_{NF}](x, y) = (I \oplus b_{NF}) \ominus b_{NF}$$

$$(3.5)$$

In order to find out lateral ventricle edge information, *opening* is implemented exclusively in the proposed algorithm. Moreover, any chance of overestimation in object boundary can also be avoided with the aid of *opening*.

## 3.2.3  Morphological Gradient

Morphological gradient (MG) is defined as the 'difference' between two adjacent pixel intensity and it is used to extract gradient information in a continuous image. The basic unit of gradient based boundary segmentation is gradient operator '$\nabla$' which can be defined for an input MRI gray scale test image $I$ in continuous space as [3, 4]:

$$\nabla I(Z_x, Z_y) = \frac{\partial I(Z_x, Z_y)}{\partial Z_x} a_x + \frac{\partial I(Z_x, Z_y)}{\partial Z_y} a_y$$

$$(3.6)$$

where $Z_x$ and $Z_y$ are two adjacent pixels, $a_x$ and $a_y$ are unit vectors along x and y axis respectively. The magnitude component of gradient vector in (3.6) determines the maximum rate of change in intensity at the location $(x_0, y_0)$ and is expressed as

$$|\nabla I(Z_x, Z_y)| = \sqrt{\left(\frac{\partial I(Z_x, Z_y)}{\partial Z_x} a_x\right)^2 + \left(\frac{\partial I(Z_x, Z_y)}{\partial Z_y} a_y\right)^2}$$

$$(3.7)$$

The counterpart of gradient, i.e. direction indicates maximum increase in intensity. For developing an edge detection strategy using MG, a local maxima of $\nabla I(Z_x, Z_y)$ is produced in many of the existing techniques. This is equivalent to a line segment for finding out a desired edge contour. As most of the medical images have graded transition between two regions, it becomes tough to choose right pixel for object boundary.

In connection to this, one pixel grid structure in a miniature $(3 \times 3)$ matrix within whole image is depicted in Fig.3.1. Any arbitrary single pixel $(Z_0)$ is considered to be surrounded by eight pixels formatting a $(3 \times 3)$ matrix as shown.
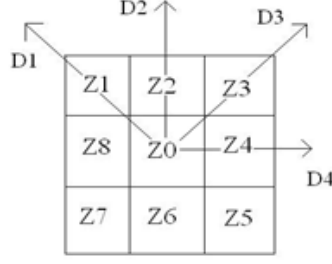
**Fig. 3.1:** $3 \times 3$ pixel matrix indicating associated arrangement and possible gradient directions $D_i$

Considering the center pixel as an edge pixel, the probable direction of edge which is calculated by possible gradients $D_i$ $\forall i \in \{1,2,3,4\}$ may be expressed as [4, 5]:

$$D_1 = \sqrt{(Z_0 - Z_1)^2 + (Z_0 - Z_5)^2} \quad D_2 = \sqrt{(Z_0 - Z_2)^2 + (Z_0 - Z_6)^2}$$
$$D_3 = \sqrt{(Z_0 - Z_3)^2 + (Z_0 - Z_7)^2} \quad D_4 = \sqrt{(Z_0 - Z_4)^2 + (Z_0 - Z_8)^2}$$

(3.9)

where $Z_0 = i(x,y), Z_1 = i(x-1,y+1), Z_2 = i(x,y+1), Z_3 = i(x+1,y+1), Z_4 = i(x+1,y), Z_5 = i(x+1,y-1), Z_6 = i(x,y-1), \ Z_7 = i(x-1,y-1), \ Z_8 = i(x-1,y)$

In conventional process, edge $E$ is calculated as:

$$E = D_1 + D_2 + D_3 + D_4$$

(3.10)

### 3.2.4 Fuzzy Connectedness Algorithm

Fuzzy connectedness algorithm is a theory of fuzzy object extraction from n-dimensional digital space based on fuzzy connected image elements. The fuzzy digital image space $I$ is an n-dimensional Euclidian space $R^n$, that can be subdivided into hyper cuboids (spels) into n mutually orthogonal families of parallel unit spaced hyper planes. Let $\gamma = (C, f)$ be a *membership scene* over a *fuzzy digital space* $(Z^n, \alpha)$. Let us also consider $\kappa$ be a *fuzzy spel affinity* in $\gamma$ and $\mathcal{N}$ be the fuzzy $\kappa$-net of $\gamma$. The set of all possible paths in $\gamma$ from k to l is denoted by $P_{k,l}$. The fuzzy $\kappa$-Net $\mathcal{N}$ of $\gamma$ is a fuzzy subset of $P_\gamma$ with its membership function defined as [6]:

$$\mu_{\mathcal{N}}(p) = \min\left[\mu_\kappa\left(c^{(1)}, c^{(2)}\right), \mu_\kappa\left(c^{(2)}, c^{(3)}\right), \dots, \mu_\kappa\left(c^{(m-1)}, c^m\right)\right]$$

(3.11)

*Fuzzy $\kappa$-Connectedness* in $\gamma$ denoted by K, is a fuzzy relation in C, defined as:

32

$$\mu_K(k,l) = \max_{p \in P_{kl}}[\mu_{\mathcal{N}}(p)] \ \forall \ k, l \ in \ C$$

Fuzzy connectedness algorithm basically assigns a *strength of connectivity* to every set of *spels* $(k, l)$. Among numerous possible paths between k and l, there exists a weakest link (defined by smallest affinity between *spels*) that determines the strength of connectivity along that path. The strength of connectivity from k to l is determined by the strongest path.

## 3.3 Proposed Algorithm

Input MRI scans are initially converted into gray level and subsequently processed with proposed morphological *opening* and finally executed through proposed fuzzy logic system (FLS).

Proposed algorithm has been explicitly described in this section with necessary mathematical illustration for the purpose of early detection of Alzheimer's disease. In connection to this, a fuzzifier has been proposed that uses one novel possible edge pixel selector depending upon individual fuzzy weights. Proposed method normalizes the intensity of each pixel and categorizes individual intensity value into five equidistant fuzzy levels. The fifth order deviation in fuzzy intensity levels provides higher flexibility of pixel segmentation. It also creates precise difference amongst those test pixels which are adjacent to edge pixel by avoiding near value congestion.

It has been observed that exclusive application of proposed fuzzy edge detection technique promises to reveal better gray matter and white matter boundary information while it shows less coherence on extracting important lateral ventricle information associated to hippocampus. This loss of information is considered to be extremely crucial for early AD detection. Present study reveals that prior *opening* of MRI scans with appropriate non uniform SE can expose lateral ventricle information which is a passive measure of hippocampus. Since lateral ventricle is surrounded by hippocampus, higher volumetric measure of lateral ventricle identifies noticeable tissue loss in AD. This has been applied in (3.13) as best fitted SE for *opening* in which general orientation and gross allocation of boundary objects in gray scale MRI scans have been taken into our consideration.

$$b_{NF} = \begin{bmatrix} 1 & 0 & 0 & 0 & 1 \\ 1 & 0 & 0 & 0 & 1 \\ 0 & 1 & 0 & 1 & 0 \\ 0 & 0 & 1 & 0 & 0 \\ 0 & 1 & 0 & 1 & 0 \\ 1 & 0 & 0 & 0 & 1 \\ 1 & 0 & 0 & 0 & 1 \end{bmatrix}$$

<div align="right">(3.13)</div>

Each pixel-intensity of input image matrix is weighted and associated with five Gaussian fuzzy equivalent membership functions; namely H (*High*), MH (*Moderate High*), M (*Medium*), ML (*Moderate Low*) and L (*Low*). In order to adapt different gray tones, intensity value of each pixel in image matrix is initially normalized to make it suitable for application under Gaussian membership function standards. These values have been used to calculate the mean of membership functions for each input $D_i \ \forall i \in \{1,2,3,4\}$. Proposed fuzzy inference system has single linguistic output values: *Edge (E) or No Edge (Not E)* in between the range [0, 1] where the fuzzy gradations can be represented in (3.14*a*) to (3.14*g*). The normalized crisp value *x* of individual pixel weight which lies between [0, 1] is mapped by singletone fuzzifier in accordance with (3.14j). For normalized input image gray tones, the output Gaussian membership functions are obtained from (3.14*l*) where the standard deviation ($\sigma$) and mean (m) of each function is calculated vide (3.14*h*) to (3.14*k*).

$Low_i = Min(D_i)$ <div align="right">(3.14*a*)</div>
$High_i = Max(D_i)$ <div align="right">(3.14*b*)</div>
$Medium_i = Low_i + (High_i - Low_i)/2$ <div align="right">(3.14*c*)</div>
$Moderate\ High_i = Medium_i + (High_i - Medium_i)/2$ <div align="right">(3.14*d*)</div>
$Moderate\ Low_i = Low_i + (Medium_i - Low_i)/2$ <div align="right">(3.14*e*)</div>
$Edge_i = 1$ <div align="right">(3.14*f*)</div>
$No\ Edge_i = 0$ <div align="right">(3.14*g*)</div>
$\sigma_x = Edge_i/4$ <div align="right">(3.14*h*)</div>
$m_1 = Edge_i$ <div align="right">(3.14*i*)</div>
$m_2 = m_1 + (m_1 \times \mu_x)$ where intensity equivalent $\mu_x$ is in [0,1] <div align="right">(3.14*j*)</div>
$m_x = (m_1 + m_2)/2$ <div align="right">(3.14*k*)</div>
$\mu_x^{'} = gaussmf(x, [\sigma_x, m_x]) = exp\left[-\frac{1}{2}\left(\frac{x - m_x}{\sigma_x}\right)^2\right]$ <div align="right">(3.14*l*)</div>

### 3.3.1 Proposed Fuzzy Rule-base

Proposed fuzzy rule-base is quite different from conventional ones. It uses Fuzzy type I Mamdani rule-base in a way that continuous checking and support for decision in favor of '*test pixels ($Z_i$) to be converted into edge pixels*' is carried out in parallel. This process itself follows

the natural rugged continuation of edges present in a digital image. Though the topological search and selection for *edge pixel* are concurrently executed in a complex hand shaking mode between rule-base and FIS; proposed rule-base, being a part of FLS, effectively generates a single output as either '*edge pixel*' or '*not an edge pixel*' as identified in Fig. 3.2. As a matter of fact, fuzzy rule-base with p inputs $x_1 \in X_1, x_2 \in X_2, \dots, x_p \in X_p$ produces single output $y \in Y$ which reflects a multiple input single output (MISO) system. With appropriate membership functions, input and output variables are modelled with proposed novel fuzzy rule-base as follows:

---

***Fuzzy rule-base***

    *If* $D_k$ *is H and* $D_l$ *is NOT H*
       *where* $k \in i, l \in i, l \neq k$ *and* $i = [1, 2, 3, 4]$
         *disp ('Z$_0$ is EDGE');*
      *Elseif*
         *$D_{k+1}$ or $D_{k-1}$ is NOT H and NOT MH*
         *disp ('Z$_0$ is Edge and $Z_i$ is PROBABLE EDGE PIXEL');*
         *Send a signal S$_1$ to FIS;*
         *Break;*
           *Elseif*
             *$D_k$ is MH and $D_l$ is NOT H and NOT MH*
             *disp ('Z$_0$ is EDGE');*
               *Elseif*
                 *$D_{k+1}$ or $D_{k-1}$ is NOT H and NOT MH and NOT M*
                 *disp ('Z$_0$ is EDGE and $Z_i$ is PROBABLE EDGE PIXEL');*
                 *Send a signal S$_2$ to FIS;*
                   *Else*
                   *disp ('Z$_0$ is NO EDGE');*
    *end if;*

---
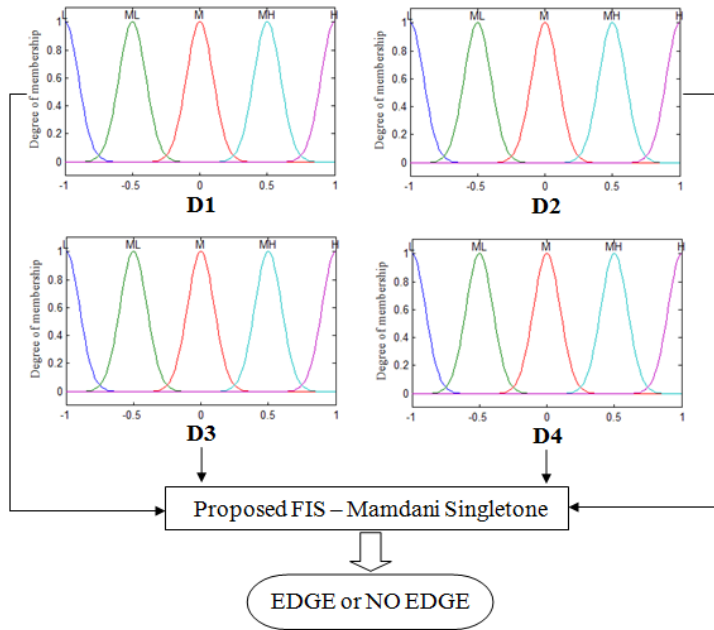
**Fig. 3.2:** Proposed FLS

Since the simple conventional execution of multiple input single outputs (MISO) rule-base is inefficient to search for possible edge pixel, rule-base is structured in a form so that it can synchronize with proposed FIS.

### 3.3.2 Proposed Fuzzy Inference System

In this proposal, selection of *next edge pixel* ($Z_i$) adjacent to *current edge pixel* ($Z_0$) at origin has been given utmost importance. A unique combination of Mamdani-type FLS logic with adjacent *edge pixel* selection topology has been incorporated. This combination traces down the most probable *edge pixels* and construct edge contour. Dynamic tracking and selection of *edge pixels* have made this algorithm novel compared to other state-of-the-art techniques. Topological selectivity of pixels in the algorithm automatically nullifies the chances of back-tracking. This algorithm, being inspired by common rugged continuation of edge topologies present in digital images, has been illustrated by means of a flow chart in Fig. 3.3.

Selection of associated fuzzy levels used in the proposed rule-base depends on mutual correlative difference of pixels. Proposed rule-base executes the center pixel $Z_0$ in Fig. 3.1 as *TEST PIXEL* and searches for selective *best fit* value (preferably H then MH). After obtaining the *best fit* value, it converts *TEST PIXEL* into *EDGE PIXEL* and searches for next associated *EDGE PIXEL* considering $Z_i$ as *TEST PIXEL* dynamically. The *best fit* values have been implemented in rule-

base to establish better precision of detected edge contour. The associability of *TEST PIXEL* with *CENTER PIXEL* can be approximated by appropriate fuzzy correlation function.

Fuzzy connectedness algorithm attempts to find the strongest path among weak links. This creates an ambiguity as the weakest link weighting is unknown and the situation becomes complicated for multiple tinny edges. Fundamentally, fuzzy connectedness algorithm and proposed method are close as both aims to find out fuzzy connectivity between *spels*. But instead of finding strongest fuzzy connectivity between two arbitrary *spels* as in [4], proposed algorithm focuses on choosing best fit correlated values of adjacent *spels* and accumulating them to find a desired link in fuzzy digital image space.
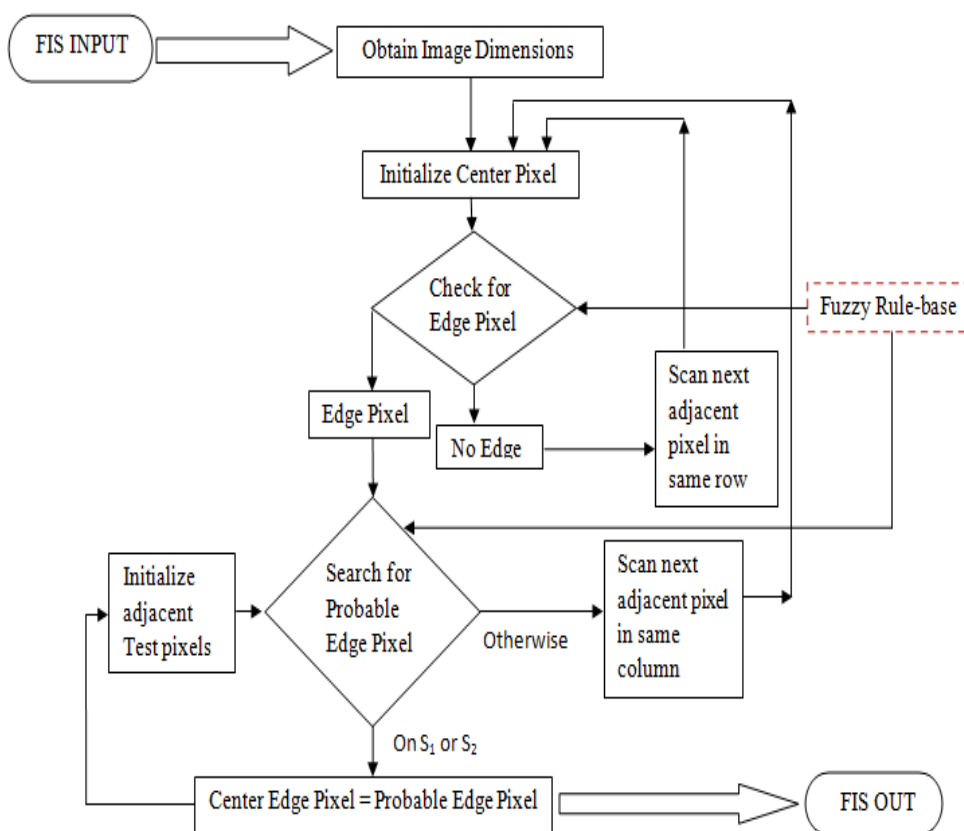


**Fig. 3.3:** Flow chart of proposed FIS

This algorithm terminates in abundance of best fit fuzzy weight so that segmented edges are traced with assured weight. Correlation between two adjacent pixel intensities is initially determined in this proposition. Let $I_k$ be any arbitrary *EDGE PIXEL* or *CENTER PIXEL* in Fig.

3.1 and adjacent *TEST PIXEL* is identified by $I_{k+i}$. Fuzzy correlation function in fuzzy image space is therefore defined as:

$$R_{I_k I_{k+i}}(\tau, a, b) = (I_k(t, a), I_{k+i}(t - \tau, b))_{L_f^2} = \int_{-\infty}^{+\infty} I_k(t, a) I_{k+i}{}^*(t - \tau, b) dt$$

(3.15)

Correlation between adjacent pixel intensities has been modeled by H and MH membership functions in the proposed approach. This strategy is implemented with the help of proposed rule-base and it settles optimum edge strength. With reference to a $(3 \times 3)$ pixel matrix as in Fig. 3.1 and considering $Z_0$ as an EDGE pixel, equation (3.11) in section 3.2.4 has been modified in (3.16). It expresses the membership function of associated *membership scene* over a *fuzzy digital space* $(Z^n, \alpha)$ as outlined below:

$$\mu_{\mathcal{N}}(p) = \begin{cases} Z_0 = Z_i & \text{when: } \max\left[R_{I_k I_{k\pm1}}(\tau, a, b)\right] \text{ is H} \\ Z_0 = Z_i & \text{when: } \max\left[R_{I_k I_{k\pm1}}(\tau, a, b)\right] \text{ is MH} \\ \quad 0 & Otherwise \end{cases}$$

(3.16)

Proposed *Fuzzy $\kappa$-Connectedness* in $\gamma$, denoted by K, is now a fuzzy relation in C. This effectively represents an edge in fuzzy digital image space and is defined as:

$$\mu_K = \sum_{p=1}^{P} [\mu_{\mathcal{N}}(p)] \text{ in a connected } C$$

(3.17)

In the absence of membership functions H or MH, algorithm terminates automatically and interprets this as an end of *edge*. This process is repeated in the entire image domain to find out all prominent edges. Proposed method in (3.17) moves on checking best fit individual *spel* intensity and accumulates them to construct strong and weak edges.

### 3.3.3   Defuzzification

After successful execution of proposed FIS, defuzzification is accomplished on test images to get desired result. Defuzzification reduces a fuzzy set into a crisp single valued quantity or set. There are several standard defuzzification methods such as maxima method, centroid method, weighted average method, middle-of-maxima method, first-of-maxima or last-of-maxima method in the literature out of which mean of maxima method has been employed in the present approach. Defuzzification provides the crisp tone in fuzzified adjacent pixel intensities of

detected edge contour. This process dispenses equivalent potential of input data set that was converted to fuzzified weights during FLS processing. For simulated mean of maxima method, defuzzification is obtained by

$$x^* = \frac{\sum_{x_i \in M} x_i}{|M|}$$

(3.18)

where,  $M = \{x_i | \mu_K(x_i) = h(C)\}$, $|M|$ is the cardinality of the set $M$  and $h(C)$ is the height off fuzzy set $C$.

## 3.4  Simulation Results

Supremacy of the proposed algorithm over other existing techniques has been demonstrated on twelve brain MRI images for the sake of comparison. All the test images are collected from ADNI database having different subject, age, series, slice and acquisition plane. The proposed algorithm is implemented in MATLAB R2014a platform with core i5 processor @ 3.20GHz, 4 GB RAM and Windows 7 Professional 32 bit operating system. Detailed description of the utilized dataset has been provided in Table 3.1 below.

**Table 3.1:** Imaging parameters for *Test images*

| Edge detector | Test image 1 | Test image 2 | Test image 3 | Test image 4 | Test image#5 | Test image 6 | Test image 7 | Test image 8 | Test image 9 | Test image 10 | Test image 11 | Test image 12 |
|---|---|---|---|---|---|---|---|---|---|---|---|---|
| ADNI image ID | 569634 | 569634 | 116582 | 116582 | 116582 | 13722 | 13722 | 13721 | 13721 | 13721 | 13721 | 863060 |
| Type details | T2 FLAIR | PD/T2 FSE | MP-RAGE | MP-RAGE | MP-RAGE | MP-RAGE | MP-RAGE | MP-R R | MP-R R | MP-R R | MP-R R | MP-R R |
| Slice | 18 of 35 | 17 of 35 | 85 of 170 | 128 of 256 | 128 of 256 | 156 of 256 | 164 of 256 | 70 of 166 | 102 of 166 | 100 of 256 | 90 of 256 | 122 of 256 |
| Acquisition plane | Axial | Axial | Sagittal | Coronal | Axial | Axial | Axial | Sagittal | Sagittal | Coronal | Coronal | Coronal |

In order to generate the *reference image*, five well established edge detection techniques namely Sobel, Canny, Prewitt, Roberts and Log have been collectively used by image addition. Image addition preserves the individual response of edge detectors which enriches the quality of *reference image*. Simulation result of the proposed algorithm has been depicted in Fig. 3.4 to 3.15 which includes original image, reference image, resultant images obtained with MG, combination of MG and type I FLS, an improved Ant Colony (AC) based edge detector [7],

39

Genetic algorithm (GA) based edge detector [8] and the proposed fuzzy pixel intensity correlation based segmentation algorithm combined with MG. Though proposed technique identifies the enhancement of edge information over the entire brain region, some prominent regions are highlighted with rectangular red boxes.
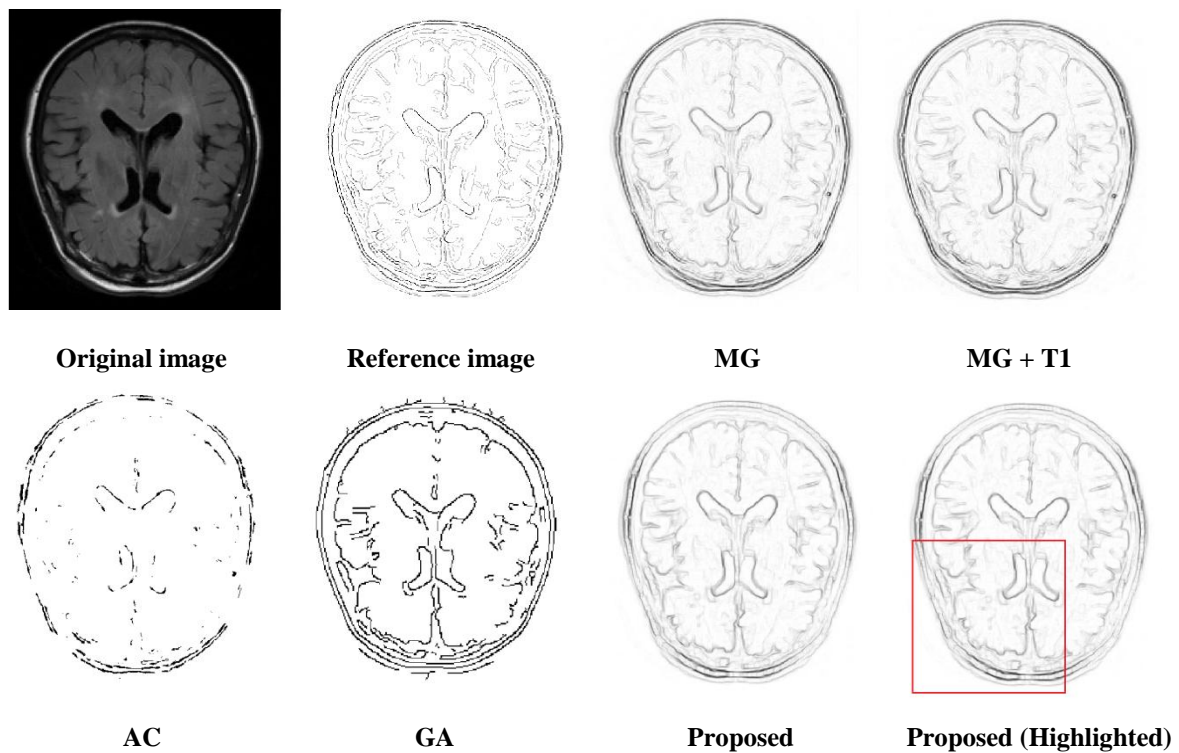


| Original image | Reference image | MG | MG + T1 |
|---|---|---|---|

| AC | GA | Proposed | Proposed (Highlighted) |
|---|---|---|---|

**Fig. 3.4** Comparative analysis for *Test image 1*

**Original image**   **Reference image**   **MG**   **MG + T1**

**AC**   **GA**   **Proposed**   **Proposed (Highlighted)**

**Fig. 3.5** Comparative analysis for *Test image 2*



**Original image**   **Reference image**   **MG**   **MG + T1**
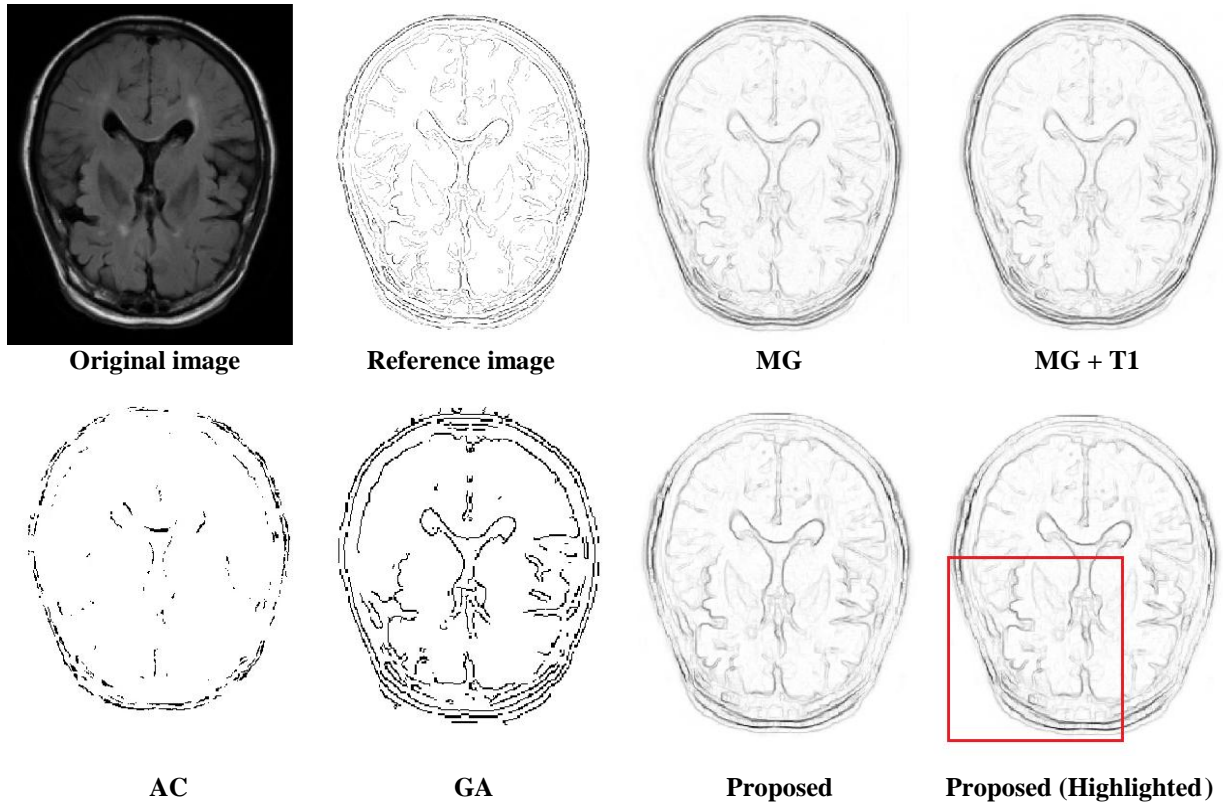
**AC**   **GA**   **Proposed**   **Proposed (Highlighted)**
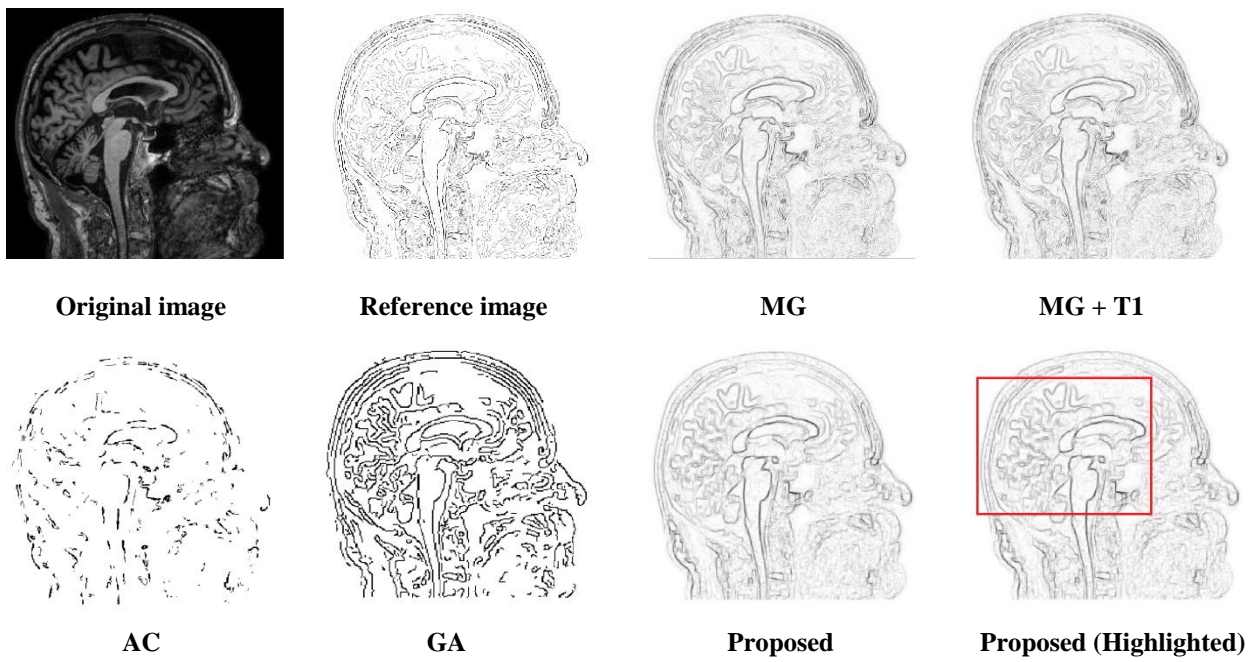
**Fig. 3.6** Comparative analysis for *Test image 3*
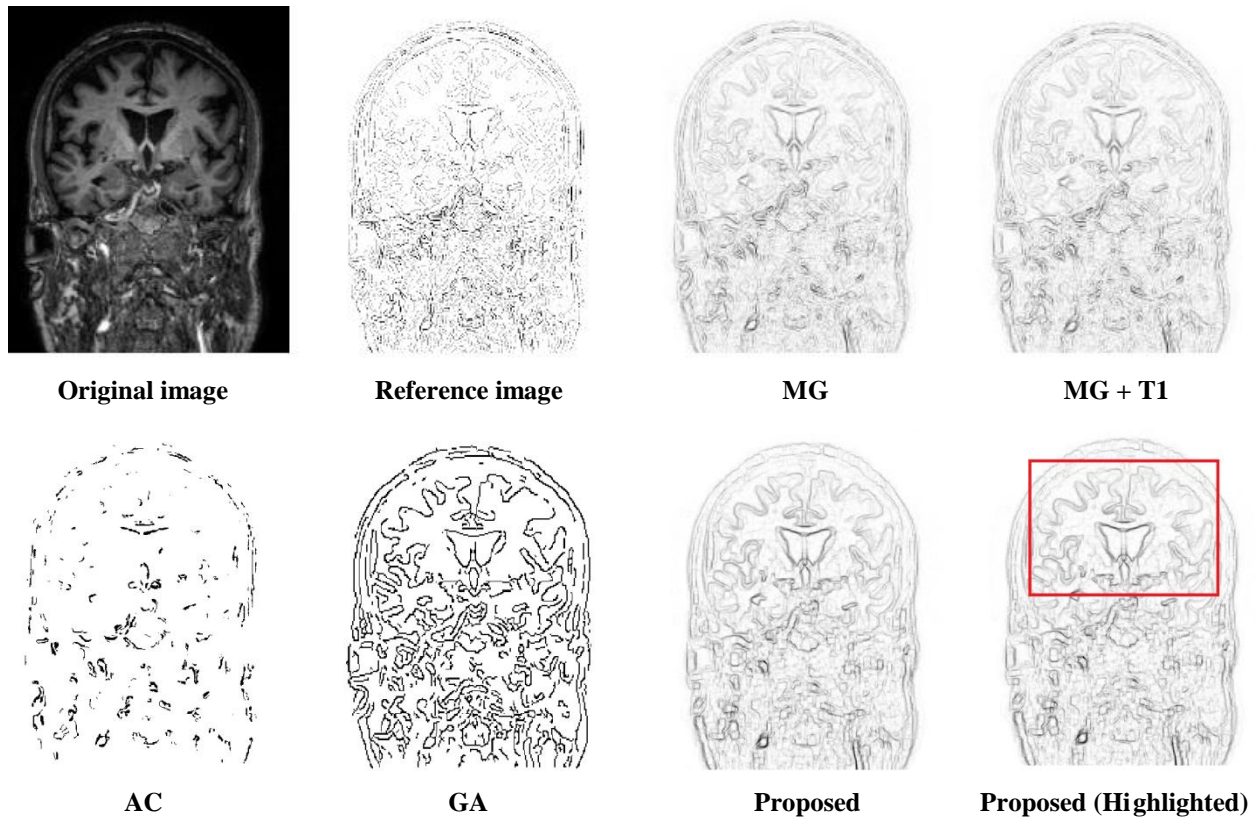
**Fig. 3.7** Comparative analysis for *Test image 4*
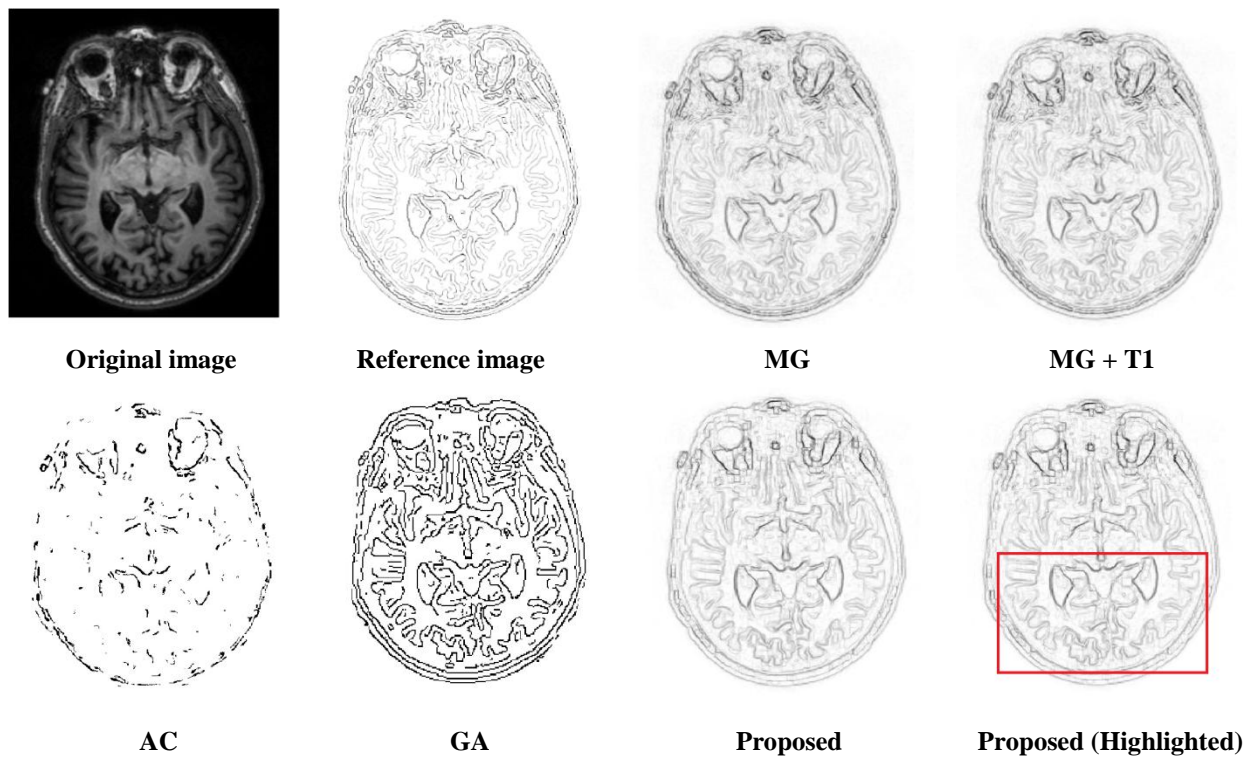


**Fig. 3.8** Comparative analysis for *Test image 5*
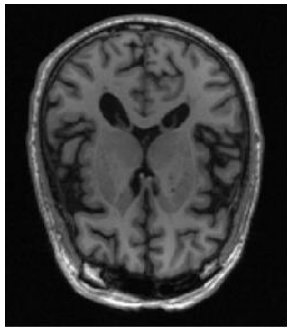
**Original image**     **Reference image**     **MG**     **MG + T1**
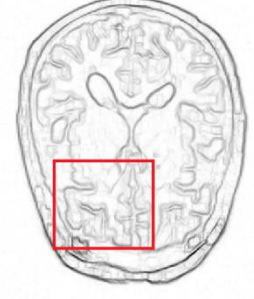
**AC**     **GA**     **Proposed**     **Proposed (Highlighted)**

**Fig. 3.9** Comparative analysis for *Test image 6*
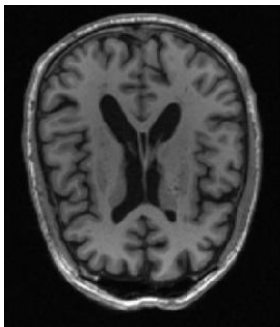


**Original image**     **Reference image**     **MG**     **MG + T1**
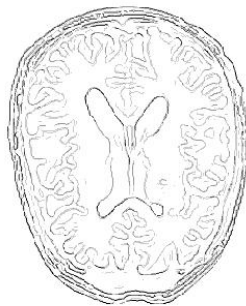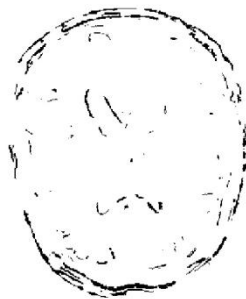
**AC**     **GA**     **Proposed**     **Proposed (Highlighted)**

**Fig. 3.10** Comparative analysis for *Test image 7*
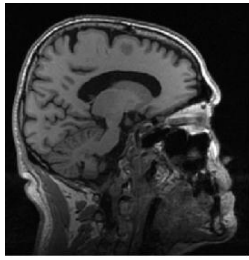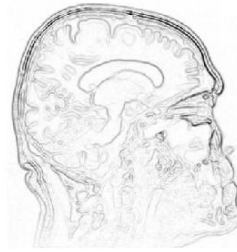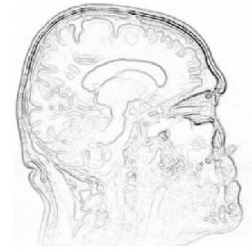
| **Original image** | **Reference image** | **MG** | **MG + T1** |

| **AC** | **GA** | **Proposed** | **Proposed (Highlighted)** |

**Fig. 3.11** Comparative analysis for *Test image 8*
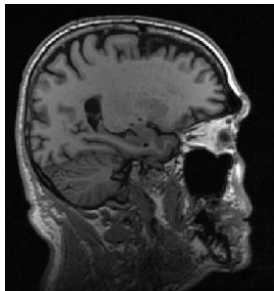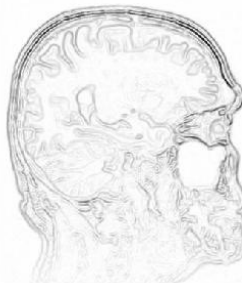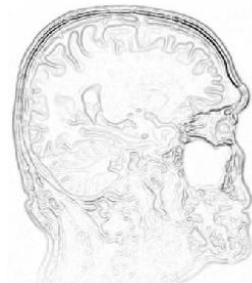


| **Original image** | **Reference image** | **MG** | **MG + T1** |

| **AC** | **GA** | **Proposed** | **Proposed (Highlighted)** |

**Fig. 3.12** Comparative analysis for *Test image 9*
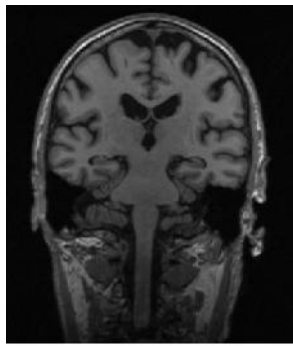
**Original image**     **Reference image**     **MG**     **MG + T1**
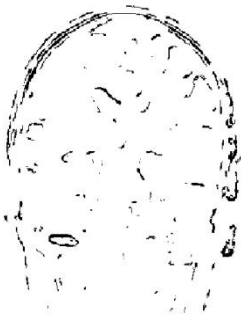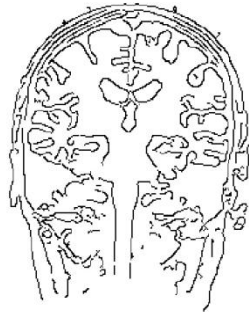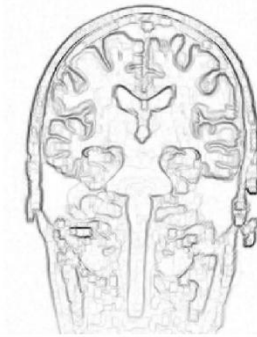
**AC**     **GA**     **Proposed**     **Proposed (Highlighted)**

**Fig. 3.13** Comparative analysis for *Test image 10*
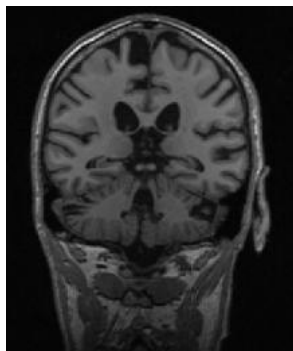


**Original image**     **Reference image**     **MG**     **MG + T1**
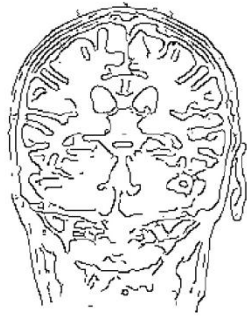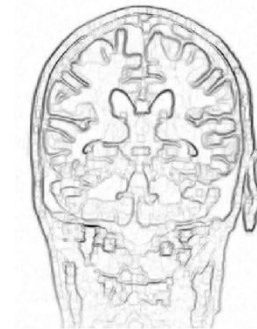
**AC**     **GA**     **Proposed**     **Proposed (Highlighted)**

**Fig. 3.14** Comparative analysis for *Test image 11*



| Original image | Reference image | MG | MG + T1 |



| AC | GA | Proposed | Proposed (Highlighted) |
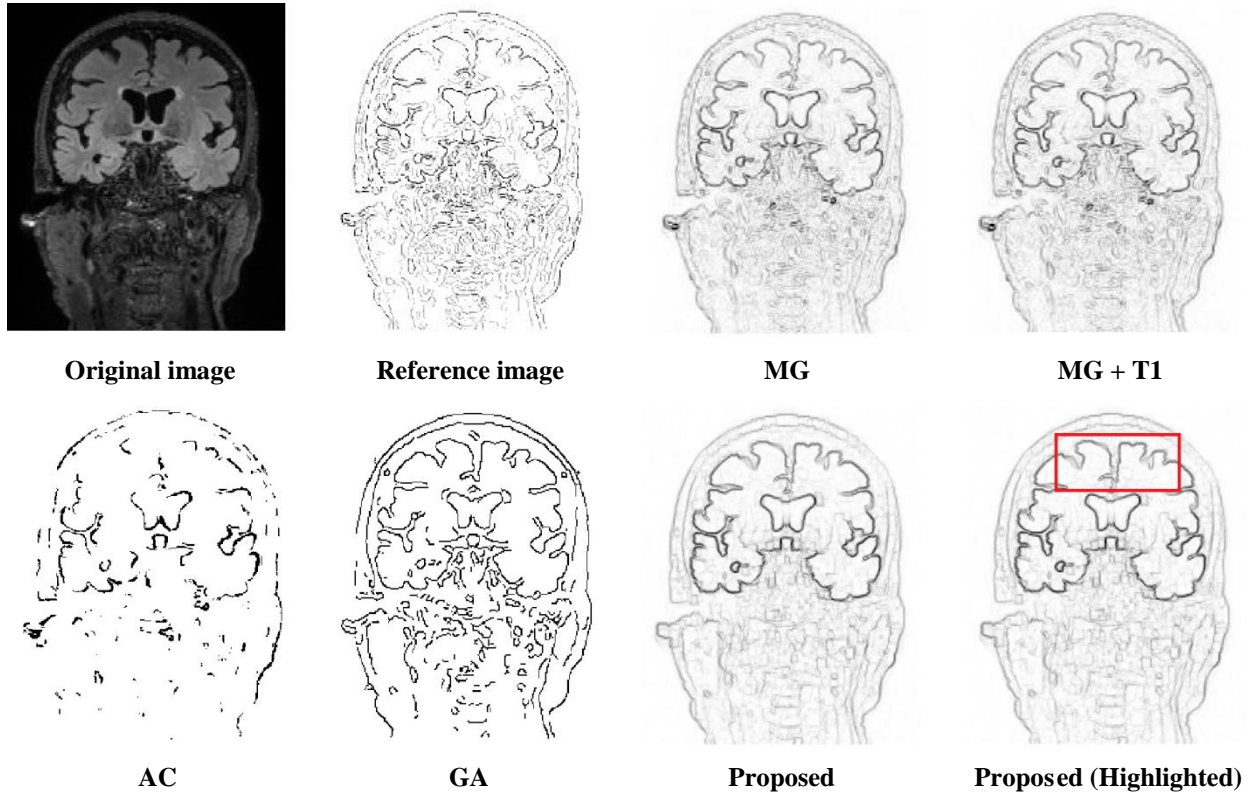
**Fig. 3.15** Comparative analysis for *Test image 12*

Comprehensive observations from the above images clearly identify that gray matter and white matter boundaries are quite evident, bold and contrast enhanced for the proposed scheme as compared to other existing algorithms. Weak and proxy edges are also getting eliminated using proposed strategy of edge detection. Moreover, the lateral ventricle region boundary is clear and prominent. In brief, the proposed algorithm reflects its qualitative supremacy towards prominent object boundary detection from brain MRI scans. This leads to trace whole brain tissue loss more accurately and subsequently helps in detecting MCI.

In addition to the qualitative discussion and visual impression, performance of the proposed edge detection technique is also evaluated in terms of a few quantitative performance parameters namely *Figure of Merit* and *Shannon's Entropy.* This has been clearly described in the following section.

### 3.4.1   Pratt's Figure of Merit (FOM)

FOM is a popularly used technique to verify the efficiency of any edge detector. FOM uses an ideal edge map to evaluate the relative difference for different edge detection techniques. It can be defined as [9]:

$$FOM = \frac{1}{\max\{N_I, N_D\}} \sum_{i=1}^{N_D} \frac{1}{1 + \tau D_i^2}$$

(3.19)

where, $N_I$: number of ideal detected edge points, $N_D$: number of actual detected edge points, $d_i$: distance between $i^{th}$ edge point detected and ideal edge point and $\tau$: scaling factor with set value of 1/9 [10]. One comparative analysis in terms of FOM has been carried out between MG, combination of MG and conventional type I fuzzy technique (MG+T1) [4], improved AC based edge detector, GA based edge detector and the proposed method. Experimentally obtained value of FOM has been listed in Table 3.2 below.

**Table 3.2:**  Comparative analysis in terms of FOM

| Edge detector | Test image 1 | Test image 2 | Test image 3 | Test image 4 | Test image 5 | Test image 6 | Test image 7 | Test image 8 | Test image 9 | Test image 10 | Test image 11 | Test image 12 |
|---|---|---|---|---|---|---|---|---|---|---|---|---|
| MG | 0.432 | 0.421 | 0.318 | 0.279 | 0.346 | 0.379 | 0.368 | 0.310 | 0.318 | 0.388 | 0.370 | 0.353 |
| MG+T1 [23] | 0.454 | 0.442 | 0.326 | 0.291 | 0.361 | 0.393 | 0.382 | 0.323 | 0.332 | 0.403 | 0.384 | 0.364 |
| AC [30] | 0.565 | 0.556 | 0.380 | 0.365 | 0.451 | 0.441 | 0.425 | 0.399 | 0.416 | 0.465 | 0.420 | 0.448 |
| GA [31] | 0.587 | 0.611 | 0.432 | 0.412 | 0.494 | 0.479 | 0.473 | 0.447 | 0.461 | 0.493 | 0.496 | 0.487 |
| Proposed Method | 0.667 | 0.671 | 0.498 | 0.489 | 0.541 | 0.545 | 0.538 | 0.533 | 0.534 | 0.577 | 0.564 | 0.539 |

From the entries in Table 3.2, it can be inferred that the proposed technique results in an improvement of 31% or more over conventional MG which is considered to be the most popular among all existing techniques. Corresponding FOM improvement over MG+T1 is calculated as 28% for the test images under consideration. It is also seen that proposed method exhibits at least 15% and 9% improvement over the techniques proposed in [7] and [8] respectively.

Performance of the proposed algorithm in terms of FOM rating has also been compared with some recently developed fuzzy techniques for edge detection in Table 3.3. While Table 3.2 shows an average improvement of 4.21% with MG+T1 FLS over conventional MG for MRI images; Table 3.3 indicates a corresponding improvement of 3.18% for standard images. Proposed algorithm, on the other hand, shows its supremacy over MG + Type I FLS, MG + Interval Type II FLS and MG + Generalized Type II FLS an improvement of 35.2% over conventional MG techniques.

**Table 3.3:** Comparative analysis with other edge detectors in terms of FOM

| Edge Detector | Image Type | Percentage improvement in FOM rating |
|---|---|---|
| MG + Type I FLS | Standard image | 3.18 |
| MG + Interval Type II FLS | Standard image | 11.57 |
| MG + Generalized Type II FLS | Standard image | 12.14 |
| Proposed algorithm | Standard image | 32.9 |
| | MRI image | 35.2 |

This experiment has also been run on public large scale brain image data set of suspected MCI subjects and the results have been substantiated in Table 3.4. Performance of the proposed algorithm shows a fair improvement in terms of FOM as compared to MG, MG + Type I FLS, AC and GA.

**Table 3.4:** Comparative analysis on public MRI image sets in terms of FOM

| Image Index | Edge Detector | | | | |
|---|---|---|---|---|---|
| | MG | MG+T1[4] | AC [7] | GA [8] | Proposed Method |
| Patient MRI 1 | 0.4602 | 0.4754 | 0.5169 | 0.5321 | 0.6181 |
| Patient MRI 2 | 0.4571 | 0.4724 | 0.5235 | 0.5478 | 0.5975 |
| Patient MRI 3 | 0.4658 | 0.4810 | 0.5440 | 0.5631 | 0.6021 |
| Patient MRI 4 | 0.4518 | 0.4672 | 0.5061 | 0.5328 | 0.5917 |
| Patient MRI 5 | 0.4570 | 0.4723 | 0.5183 | 0.5591 | 0.5957 |
| Patient MRI 6 | 0.4073 | 0.4218 | 0.4684 | 0.4977 | 0.5323 |
| Patient MRI 7 | 0.4370 | 0.4520 | 0.4992 | 0.5328 | 0.5757 |
| Patient MRI 8 | 0.4054 | 0.4198 | 0.4869 | 0.5108 | 0.5704 |

| | | | | | |
|---|---|---|---|---|---|
| *Patient MRI 9* | 0.3852 | 0.3990 | 0.4201 | 0.4645 | 0.5190 |
| *Patient MRI 10* | 0.4084 | 0.4228 | 0.4864 | 0.5149 | 0.5511 |
| *Patient MRI 11* | 0.4299 | 0.4454 | 0.4906 | 0.5112 | 0.5613 |
| *Patient MRI 12* | 0.4170 | 0.4323 | 0.4781 | 0.4990 | 0.5666 |
| *Patient MRI 13* | 0.4668 | 0.4824 | 0.5324 | 0.5611 | 0.6080 |
| *Patient MRI 14* | 0.4567 | 0.4727 | 0.5124 | 0.5446 | 0.6094 |
| *Patient MRI 15* | 0.4207 | 0.4356 | 0.4845 | 0.5119 | 0.5684 |
| *Patient MRI 16* | 0.4348 | 0.4506 | 0.4893 | 0.5121 | 0.5535 |
| *Patient MRI 17* | 0.4186 | 0.4338 | 0.4779 | 0.5027 | 0.5467 |
| *Patient MRI 18* | 0.3663 | 0.3817 | 0.4457 | 0.4923 | 0.5772 |
| *Patient MRI 19* | 0.3723 | 0.3875 | 0.4368 | 0.4729 | 0.5634 |
| *Patient MRI 20* | 0.3655 | 0.3809 | 0.4359 | 0.4637 | 0.5705 |
| *Patient MRI 21* | 0.3438 | 0.3588 | 0.3897 | 0.4231 | 0.5501 |
| *Patient MRI 22* | 0.3508 | 0.3659 | 0.4125 | 0.4724 | 0.5576 |
| *Patient MRI 23* | 0.3617 | 0.3769 | 0.4213 | 0.4651 | 0.5628 |
| *Patient MRI 24* | 0.3540 | 0.3689 | 0.4358 | 0.4711 | 0.5572 |
| *Patient MRI 25* | 0.3668 | 0.3795 | 0.4597 | 0.4782 | 0.5427 |
| *Patient MRI 26* | 0.4217 | 0.4351 | 0.4926 | 0.5214 | 0.5732 |
| *Patient MRI 27* | 0.6042 | 0.6178 | 0.6358 | 0.6502 | 0.7094 |
| *Patient MRI 28* | 0.4752 | 0.4896 | 0.5478 | 0.5532 | 0.6192 |
| *Patient MRI 29* | 0.4147 | 0.4272 | 0.4781 | 0.5071 | 0.5549 |
| *Patient MRI 30* | 0.4148 | 0.4280 | 0.4741 | 0.4956 | 0.5456 |
| *Patient MRI 31* | 0.4602 | 0.4743 | 0.5086 | 0.5127 | 0.5781 |
| *Patient MRI 32* | 0.4892 | 0.5033 | 0.5298 | 0.5402 | 0.5963 |
| *Patient MRI 33* | 0.4728 | 0.4873 | 0.5161 | 0.5441 | 0.5794 |
| *Patient MRI 34* | 0.4535 | 0.4682 | 0.5149 | 0.5477 | 0.5823 |
| *Patient MRI 35* | 0.4400 | 0.4553 | 0.5143 | 0.5287 | 0.5847 |

## 3.4.2  Shanon's Entropy

FOM generally compares the detected edge map with an ideal one in which information about weak edges does not contain much importance. Shannon's entropy, on the other hand, takes care of the problem of losing weak edge information. Hence, the proposed edge detection technique has also been tested in terms of Shannon's Entropy as well, which is defined as [11]:

$$H(I) = -\sum_{i=0}^{L-1} p_i \log_2 p_i$$

(3.20)

where $I$ indicates the image or edge map, $p_i$ represents the probability of a pixel having intensity $i$ and L signifies the total number of intensity levels.

Variation of entropy with image index has been shown in Fig. 3.16 below for different edge detection techniques under consideration. The plot in Fig. 3.16(a) and Fig. 3.16(b) apprises that proposed method exhibits higher value of entropy than reference image and the edge detectors in [7] and [8]. It suggests that more information about weak edge can be extracted from the proposed method as compared to [7] and [8]. At the same time, entropy values resulting from the proposed method are very close but slightly lower than

49

MG and MG+T1. This guarantees that proxy edge information can be removed by means of proposed method in comparison to MG and MG+T1. This exercise has also been carried out for public MRI image sets and one such entropy plot has been shown in Fig. 3.17 for the sake of completeness.
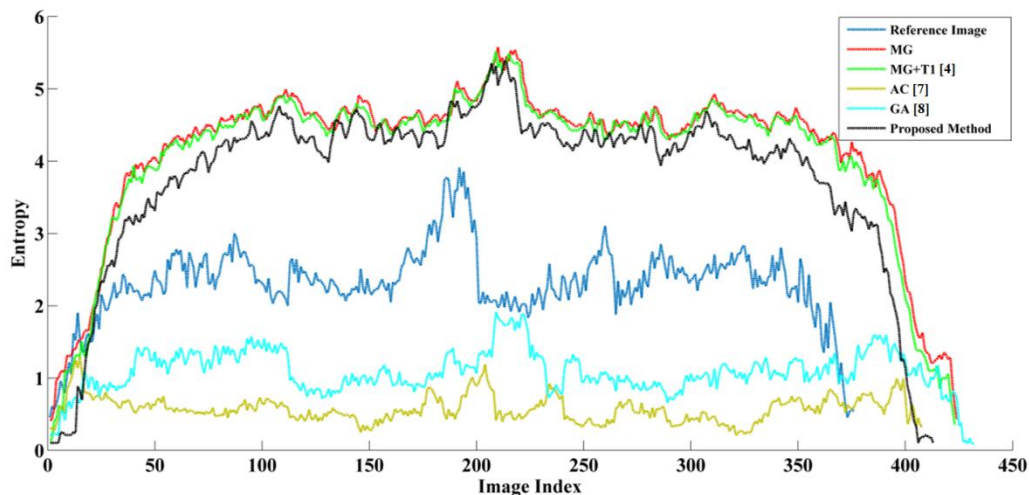


(a)
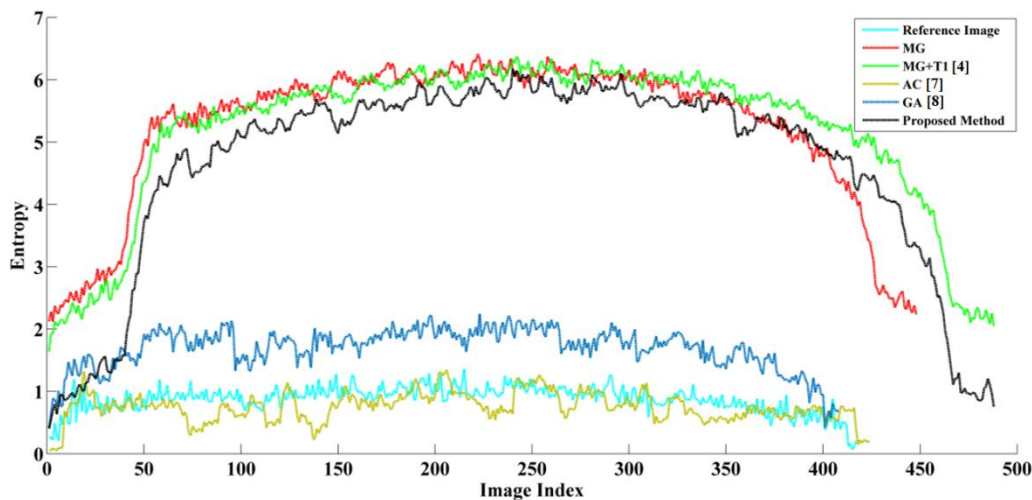


(b)

**Fig. 3.16** Variation of entropy with image index for **(a)** *Test image 1* and **(b)** *Test image 5*
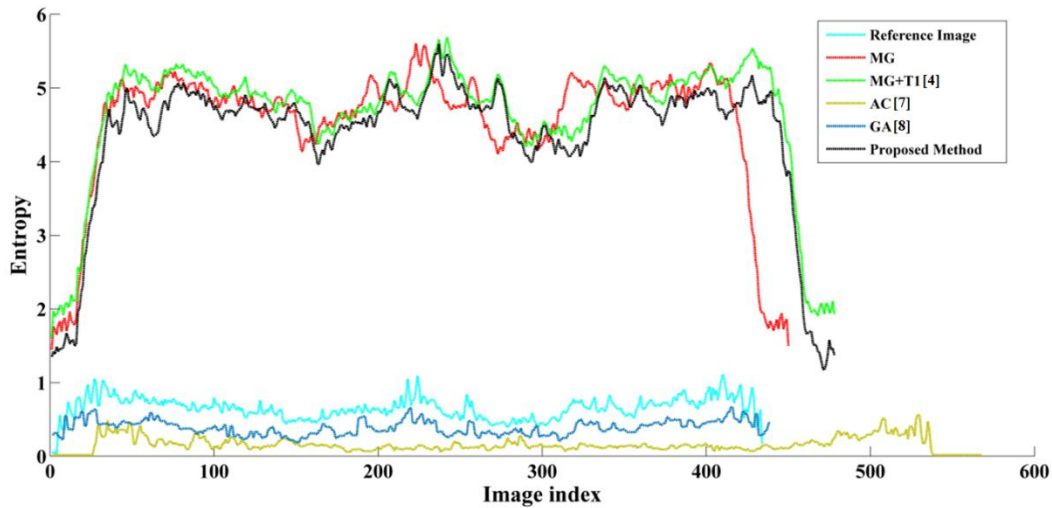
**Fig. 3.17** Variation of entropy with image index for *Patient MRI 34*

## 3.5 Discussion

In this chapter, a novel method comprising of filtering and fuzzy logic based segmentation algorithm is successfully implemented for brain MRI image object boundary detection. The presented topology based selection algorithm is developed with a novel fuzzy rule-base and inference system to provide improved boundary output. Experimental results show a promising improvement in edge detection and contrast enhancement both visually and quantitatively. Capability of presented algorithm in detecting edge boundaries for MRI test images has been substantiated. It proves to be useful for early detection of AD through more accurate detection of regional boundaries of brain and tracing of abnormal tissue losses.

## REFERENCES

1.  Rafael C. Gonzalez, Richard E. Woods, Digital Image Processing, 3$^{rd}$ ed., Pearson India.
2.  A. Chandra, S. Modal, "Amalgamation of iterative double automated thresholding and morphological filtering: A new proposition in the early detection of cerebral aneurysm. Multimedia Tools and Applications", Springer, vol.76, no.22, pp. 23957–23979, 2017.
3.  A. C. Bovik, "The essential guide to image processing. New York, NY, USA: Academic, pp. 498–500, 2009.
4.  P. Melin et al., "Edge detection method for image processing based on Generalized Type-2 fuzzy logic", IEEE Transactions on Fuzzy Systems, vol. 22, pp. 1515-1525, 2014.
5.  Y. Becerikli and T. M. Karan, "A new fuzzy approach for edge detection 2 detection of image edges", Computational Intelligence and Bioinspired Systems. Berlin, Germany: Springer Verlag, pp. 943–951, 2005.
6.  J. K. Udupa, S. Samarasekera, "Fuzzy connectedness and object definition: theory, algorithms and applications in image segmentation", Graphical Models and Image Processing, vol.58, no.3, pp. 246-261, 1996.
7.  Zhiping Chen et al., "The research and application of improved ant colony algorithm with multi-thresholds in edge detection", International conference on Industrial Informatics - Computing Technology, Intelligent Technology, Industrial Information Integration (ICIICII), pp. 5-9, 2017.
8.  Wenlong Fu, Mark Johnston and Mengjie Zhang, "Low level feature extraction for edge detection using genetic programming", IEEE Transactions on Cybernetics, vol.44, pp. 1459-1472, 2014.

9.      I. Abdou, W. Pratt, "Quantitative design and evaluation of enhancement/thresholding edge detectors", Proc. IEEE, vol. 67, no. 5, pp. 753-763, 1979.

10.     M. Setayesh, M. Zhang, M. Johnston, "A novel particle swarm optimization approach to detecting continuous, thin and smooth edges in noisy images", Information Sciences, vol. 246, pp. 28-51, 2013.

11.     C. E. Shannon, "A mathematical theory of communications". Bell System Technical Journal, vol. 27, pp. 379-423, 1948.

# Chapter 4

# A Composite Implementation of Robust Morphological Filtering and Self Adaptive Fuzzy Clustering for Improved Lateral Ventricle Classification

## 4.1 Introduction

The lateral ventricle (LV) region segmentation from brain MRI scans is challenging due to low contrast impression, tinny or proxy edges and presence of noise for overlapping regions. Morphological changes of LV like hypertrophy are prominently caused by the progression of cerebral cortical atrophy. In this chapter, a robust morphological filter is proposed which can eliminate noise, focus lateral ventricle and create an optimum estimation of object boundary as well. Subsequent implementation of a novel amalgamation of self adaptive fuzzy c-means (FCM) clustering algorithm, active contour without edge (ACWE) algorithm and a region growing (RG) method is executed to segregate lateral ventricular region. This unique combination of multiple algorithms provides an excellent qualitative improvement over LV region segmentation for AD and MCI subjects. Additionally, simulation results of the proposed method are evaluated quantitatively with multiple measures where a promising capability of LV segregation from brain MRI scans is unveiled.

## 4.2 Initial Works

### 4.2.1 Pre-processing

Input MRI test images of AD affected subject from ADNI dataset have been taken into our consideration in this study. All the input T1 brain MRI images are converted into its corresponding gray scale equivalent. The gray scale image $I$ hence can be expressed as [1]:

$$I(i,j) = 0.299 I_R(i,j) + 0.587 I_G(i,j) + 0.114 I_B(i,j)$$

$$\forall i \in \{1,2,\ldots,N_R\} \, and \, j \in \{1,2,\ldots,N_C\}$$

where $I_R, I_G, I_B$ coefficients represent red, green and blue (RGB) components in input true color image. $N_R$ $and$ $N_C$ symbolize the number of rows and columns present in the input image respectively. The hue and saturation information present in a RGB image are thus eliminated in (4.1).

## 4.2.2   Morphological Filtering

Morphological filtering (MF) is generally performed with two operations, namely opening and closing. Appropriate filtering can be employed to extract important features from a digital image while, at the same time, it can also decrease light dark details. Opening and closing are performed with two fundamental morphological processes, namely erosion and dilation. One of the most vital challenges for opening and closing is to choose appropriate 'structuring element' (SE) which determines its effectiveness and accuracy. Structuring elements are of two types, namely 'uniform structuring' element and 'non uniform structuring element'.

The set of Euclidian coordinates corresponding to the input MRI scan $I$ eroded with structuring element $b_{NF}$ is given by [2]:

$$I \ominus b_{NF} = \{w : b_{NFw} \subseteq I\}$$

(4.2)

where $b_{NFw}$ specifies translation of $b_{NF}$ at its origin 'w', i.e. for any

$$w = (x, y), b_{NFw} = \{(a, b) + (x, y) : (a, b) \in b_{NF}\}$$

In case the input binary image $I$ is dilated with structuring element $b_{NF}$, the set of euclidian coordinates becomes:

$$I \oplus b_{NF} = \bigcup_{w \in b_{NF}} I_w$$

(4.3)

where $I_w$ is any arbitrary pixel of interest at image space. Opening and closing are executed with these two fundamental morphological operations. For an input MRI image $I$ and structuring element $b_{NF}$, the opening of $I$ can be described as :

$$I \circ b_{NF} = (I \ominus b_{NF}) \oplus b_{NF} = \bigcup (b_{NFw} : b_{NFw} \subseteq I)$$

(4.4)

Similarly closing of $I$ with structuring element $b_{NF}$ is achieved by applying dilation followed by erosion:

$$I_{MF\sigma} \bullet b_{NF} = (I_{MF\sigma} \oplus b_{NF}) \ominus b_{NF} = \left\{ w : b_{NFw} \subseteq \bigcup_{w \in b_{NF}} I_{MF\sigma w} \right\}$$

(4.5)

### 4.2.3 Normalization of Test Images

Morphological filtering is followed by the process of normalization before applying fuzzy c-means clustering algorithm. In this step, pixel intensity values are scaled over the entire range of image intensity. The normalization process is carried out in accordance with the following sequential proceedings:

i) Considering $I$ as test image matrix, absolute difference between minimum and maximum gray scale values are calculated as:

$$D_I = |\max(I) - \min(I)| \tag{4.6}$$

ii) Pixel value at any arbitrary location $(x, y)$ is scaled within the range of (0-255) in accordance with:

$$I(x, y) = \left((\max(I))\frac{255}{D_I}\right) - \left((\min(I))\frac{255}{D_I}\right) \tag{4.7}$$

### 4.2.4 Fuzzy C-Means Clustering Algorithm

Dunn [3] introduced Fuzzy c-means (FCM) clustering algorithm which was further developed by Bezdek [4]. It is a dynamic optimization algorithm that creates two or more adjoint clusters in fuzzy space depending on associated fuzzy pixel intensity values. Given a finite dataset $X = \{x_1, x_2, \dots, x_n\}$ where n is the maximum number of sample point within the set; $x_i = \{x_{i1}, x_{i2}, \dots, x_{il}\}$ is an object of '$l$' dimension; '$i$' is object sequence; $x_{ij}$ is the $j^{th}$ property of $i^{th}$ object; $C = \{C_1, C_2, \dots, C_c\}$ denotes a total $c$ number of clusters and $V = \{v_1, v_2, \dots, v_c\}$ represents the $c$ number of one dimensional cluster centroids. FCM partitions the objects (n measured) into c-clusters through an iterative minimization of *objective function* outlined as:

$$J_m(U, V) = \sum_{j=1}^{c}\sum_{i=1}^{n} u_{ji}^m \|x_i - v_j\|_2^2$$

$$\tag{4.8}$$

where $u_{ji}$ is the membership function of $i^{th}$ object in $j^{th}$ cluster, $U = \{u_{ji}\}$, $i = 1,2, \dots, n$ and $j = 1,2, \dots, c$ and $m$ is a fuzzy factor which holds value between $[1, \infty]$ and usually set as 2. The symbol $\|\cdot\|$ expresses the distance between object $x_i$ and cluster center $v_j$. FCM is an iterative clustering method which finds the solution of *objective function*, $J_m$ as follows:

i) Set for c, m and threshold, $\varepsilon$

ii) Initialize partition matrix $U^0$

iii) Set for a loop counter $p = 0$.

iv) At step 't', calculate cluster centers $v_j^{(t)}$ as:

$$v_j^{(t)} = \frac{\sum_{i=1}^{n}\left(u_{ji}^{(t)}\right)^m x_i}{\sum_{i=1}^{n}\left(u_{ji}^{(t)}\right)^m} \quad for\, j = 1,2,\dots,c$$

v)   Calculate the membership matrix $U^{(t+1)}$ and new cluster centers $v_i^{(t+1)}$

$$u_{ji}^{(t+1)} = \left(\sum_{k=1}^{c}\left(\frac{\left\|x_i - v_j^{(t)}\right\|_2^2}{\left\|x_i - v_k^{(t)}\right\|_2^2}\right)^{\frac{1}{m-1}}\right)^{-1} \quad for\, i = 1,2,\dots,n \;and\; j = 1,2,\dots,c$$

$$v_i^{(t+1)} = \frac{\sum_{i=1}^{n}\left(u_{ji}^{(t+1)}\right)^m x_i}{\sum_{i=1}^{n}\left(u_{ji}^{(t+1)}\right)^m} \quad for\, i = 1,2,\dots,n \;and\; j = 1,2,\dots,c$$

vi)   If $\max\left\{U^{(t)} - U^{(t+1)}\right\} < \varepsilon$ then stop;

else set $t = t + 1$ and go to step (iv).

### 4.2.5   Fuzzy Local Information based C-Means Clustering Algorithm (FLICM)

Krinidis and Chatzis [5] proposed a novel fuzzy clustering method which incorporates local spatial information and gray level information. In *FLICM,* a novel fuzzy factor $G_{ji}$ was introduced which can be defined as:

$$G_{ji} = \sum_{\substack{r \in N_i \\ r \neq i}} \frac{1}{1 + d_{ir}}\left(1 - u_{jr}\right)^m \left\|x_r - v_j\right\|_2^2$$

(4.9)

where $N_i$ specifies a local window surrounded to $i^{th}$ pixel. In (4.9), $r$ is the adjacent neighbor pixel of $i$, $d_{ir}$ is the Euclidian distance between $i\; and\; r$ and $u_{jr}$ represents the membership function of $r$ to belong to $j^{th}$ cluster. So the objective function of FLICM incorporates $G_{ji}$ and it becomes:

$$J_m^{(FLICM)}(U,V) = \sum_{j=1}^{c}\sum_{i=1}^{n}\left[u_{ji}^m \left\|x_i - v_j\right\|_2^2 + G_{ji}\right]$$

(4.10)

### 4.2.6   Active Contour without Edges (ACWE)

Chan and Vese [6] proposed a boundary detection algorithm for image objects whose edges are likely not defined by gradient. In this model, the problem is formulated as "mean-curvature-flow" like evolving active contour which is set by curve evolution algorithm and terminated on Mumford-Shah functional segmentation conditions. ACWE starts with an initial curve like a square or circle and deforms its contour

until object boundary is estimated. Assuming $\Omega$ as a bounded open subset of $\mathbb{R}^2$ and $\partial\Omega$ as its boundary, let us consider the evolving curve $C$ in $\Omega$ is the boundary of open subset $\omega$ of $\Omega$ (i.e. $\omega \subset \Omega$ and $C = \partial\omega$). Therefore, the region $\omega$ denotes $inside\ (C)$ and region $\Omega\backslash\omega$ denotes $outside(C)$.

Let us assume that image $c_0$ is composed of two regions of near piecewise-constant intensity values $c_0^i$ and $c_0^o$. It is also assumed that image object to be detected is expressed by $c_0^i$ values and its boundary is $C_0$. Hence, it must be stated that $c_0 \approx c_0^i$ is valid for inside the object boundary (inside $C_0$) and $c_0 \approx c_0^o$ satisfies outside object boundary (outside $C_0$) condition. Based on energy of test image, the basic 'fitting' term of ACWE is defined as [6]:

$$F_1(C) + F_2(C) = \int_{inside\ (C)} |c_0(x,y) - c_1|^2 dxdy + \int_{outside\ (C)} |c_0(x,y) - c_2|^2 dxdy$$

(4.11)

where $c_1\ and\ c_2$ are the inside mean and outside mean of variable curve $C$ respectively. Energy function of ACWE algorithm is formulated as:

$$F(c_1, c_2, C) = \mu \cdot Length(C) + \vartheta \cdot Area\big(inside(C)\big) + \lambda_1 \int_{inside\ (C)} |c_0(x,y) - c_1|^2 dxdy$$

$$+ \lambda_2 \int_{outside\ (C)} |c_0(x,y) - c_2|^2 dxdy$$

(4.12)

where $\mu \geq 0, \vartheta \geq 0, \lambda_1, \lambda_2 > 0$ are constants and $Length(C)$ is smoothness parameter. By using level set method [6], the evolving curve $C(T)$ is represented through zero level set of Lipschitz function $\rho : \Omega \to \mathbb{R}$, such as:

$$\begin{cases} C = \partial\omega = \{(x,y) \in \Omega : \rho(x,y) = 0\} \\ inside(C) = \omega = \{(x,y) \in \Omega : \rho(x,y) > 0\} \\ outside(C) = \Omega\backslash\overline{\omega} = \{(x,y) \in \Omega : \rho(x,y) < 0 \end{cases}$$

(4.13)

The function $\rho$ is used to minimize the energy. Now Heaviside function $H$ and one-dimensional Dirac measure $\delta_0$ are defined as:

$$H(z) = \begin{cases} 1, if\ z \geq 0 \\ 0, if\ z < 0 \end{cases}$$
$$\delta_0(z) = \frac{d}{dz}H(z)$$

(4.14)

The energy term becomes:

$$\lambda_1 \int_\Omega |c_0(x,y) - c_1|^2 \cdot \big(1 - H\big(\rho(x,y)\big)\big) dxdy$$

$$+ \lambda_2 \int_\Omega |c_0(x,y) - c_2|^2 \cdot \big(1 - H\big(\rho(x,y)\big)\big) dxdy + \mu \int_\Omega \delta_0(\rho(x,y) \cdot |\nabla(x,y)|) dxdy$$

In order to settle the Eular-Lagrange equation for function, regularized versions of $H$ and $\delta_0$ are considered as $H_\alpha$ and $\delta_\alpha$ as $\alpha \to 0$. Consequently the equation of growth becomes:

$$\frac{\partial \rho}{\partial T} = \delta_\alpha \left[ \mu \, div \left( \frac{\nabla \rho}{|\nabla \rho|} \right) + \lambda_1 |I(x,y) - c_1|^2 - \lambda_2 |I(x,y) - c_2|^2 \right]$$

$$\text{and} \quad \frac{\delta_\alpha}{|\nabla \rho|} \cdot \frac{\partial \rho}{\rho \aleph} = 0 \; on \; \partial\Omega$$

where $\aleph$ specifies the exterior normal to the boundary $\partial\Omega$, and $\frac{\partial \rho}{\rho \aleph}$ denotes normal derivative of $\rho$ at $C$.

### 4.2.7   Region Growing (RG) Algorithm

Execution of RG starts with graphical insertion of a seed point of the designated region which needs to be segmented. For selecting adjacent pixels, a threshold is set which determines the minimum divergence of intensity compared to seed point [7]. In the proposed algorithm, RG checks and inserts threshold limited pixels to form up the ROI. The limit of boundary for RG is settled by ACWE and robust classified LV is obtained.

Here the mathematical elastration for RG algorithm is abbreviated as [7]:

(1) The process of fitting an appropriate surface over the image data field can be expressed as:

$$f(x, y, a, m) = \sum_{i+j \leq m} a_{ij} x^i y^j$$

where $f(x, y)$ is a smooth graph surface, $a$ is coefficient vector, $f(x, y)$ is the smooth graph surface, and $m$ is the surface order {1 (Planner), 2 (Biquadratic), 3 (Bicubic), 4 (Biquartic)}.

The partition the test image is initiated into seed regions $R_i^{(0)}$ (e.g., spliting the test image in preset $X \times Y$ regions) where $R$ signifies the support region.

(2) Fit a planner model for every seed region. If the error vector becomes small, accept $R_i^{(0)}$ for the same region; otherwise reject $R_i^{(0)}$.

$$E(R, a, m) = \sum_{(x,y) \in R} [g(x, y) - f(x, y, a, m)]^2$$

where $g(x, y)$ is the reconstructed image.

(3) To avoid outliers, for each region, figure out all neighbor points that are *compatible*.

$$C_i^{(k)} = [(x, y): (g(x, y) - f(x, y, a, m))^2 < \varepsilon \text{ and } (x, y) \text{ is a } 4 - neighbor \text{ of } R_i^{(k)}]$$

(4) If there is no compatible point, then increment $m$; e.g., $m = m + 1$. If $m > M$ ($M$ is the polynomial order), stop growing $R_i^{(k)}$ further; otherwise, go back to step 3.

(5) From the newly grown region, $R_i^{(k+1)} = R_i^{(k)} \cup C_i^{(k)}$, refit the model to $R_i^{(k+1)}$, and compute $E(R_i^{(k+1)}, a, m)$.

(6) Now calculate the difference error:

$$\rho^{(k)} = E\left(R_i^{(k+1)}, a, m\right) - E(R_i^{(k)}, a, m)$$

(7) If $\rho^{(k)} < T_1$, go back to step 3.

(8) $m = m + 1$; if $m > M$, stop growing the region further.

(9) Refit the region for the new model $f(x, y, a, m)$. If the error of fit decreases, consider the new model and go back to step 3; otherwise, stop growing the region further.

## 4.3   Proposed Methodology

In this work, a novel automated segmentation scheme is proposed to segment lateral ventricle of AD subject. Proposed method is a sequential combination of different algorithms with necessary alteration and advancements. General overview of entire process is demonstrated in Fig. 4.1. Since brain MRI input test

sets are of limited resolution, boundary region estimations should be very specific and overestimation needs to be ignored. Hence, MF *opening* has been employed only so as to avoid the chance of possible overestimation.
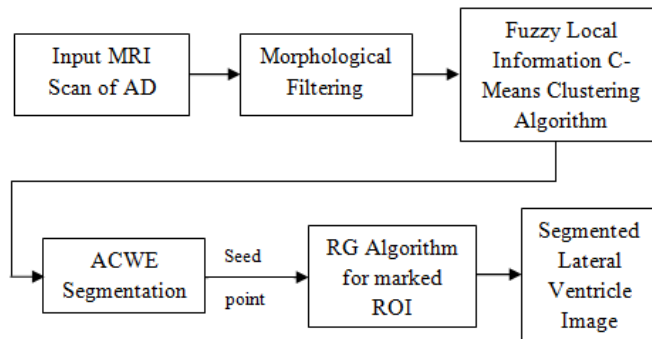


**Fig. 4.1** Proposed block architecture for LV segmentation.

As an attempt to fetch lateral ventricle domain information from low contrast input T1 MRI dataset in a best possible way, a robust non-uniform structuring element $b_{NF}$ has been utilized in this study as outlined next.

$$b_{NF} = \begin{bmatrix} 1 & 0 & 1 \\ 1 & 0 & 1 \\ 0 & 1 & 0 \\ 1 & 0 & 1 \\ 1 & 0 & 1 \end{bmatrix}$$

(4.17)

To find the optimum number of clusters ($c$), a self adaptive FCM is examined with different number of clusters in the search range. Each result of FCM execution is then evaluated with a *clustering validity index* which can be expressed as a checking parameter of quality in clustering results and subsequently an optimum value of $c$ is finalized. The entire process is constructed in the following steps:

(i) Find $[c_{min}, c_{max}]$ for the input image space

(ii) For each integer $k \in [c_{min}, c_{max}]$ and $k > Threshold$; run FCM

(iii) Calculate *clustering validity index* for $k$, stack in $\vartheta = \{c_{current}\}$ and search for another value of $k$

(iv) Repeat the steps for entire input domain

(v) Compare all the values stored in $\vartheta$ and find out optimum one, $c_{opt}$

The rough set of maximum number of clusters $c_{max}$ and corresponding cluster centers $v_{opt}$ are approximated by Density-based-algorithm (DBA). The initial cluster selection procedure of density based algorithm is executed by assembling pixels with higher local density surrounded by lower local density and relatively large distances with other cluster centroids. The local density $\varsigma_i$ of object $x_i$ can be defined as [8]:

$$\varsigma_i = \sum_{j=1}^{n} e^{-d_{ij}^2/d_c^2}$$

(4.18)

where $d_{ij}$ is the distance between objects $x_i$ and $x_j$ and $d_c$ is a cutoff distance. DBA sorts the distances between any two objects in a descending order and selects $d_c$ as the corresponding value to the first p% of the sorted distances (roughly $p \in [2, 5]$). The number of initial cluster centers is determined by the choice of $d_c$. Further an optimum number of cluster $c_{opt}$ is settled with the help of proposed fuzzy clustering index.

A fuzzy clustering validity index makes a tradeoff between compactness and separation which effectively helps to obtain an optimal clustering result. The index can be defined as [9]:

$$V_{XB}(u, v) = \frac{\left(\frac{1}{n}\right) \sum_{i=1}^{c} \sum_{j=1}^{n} u_{ij}^m \left\| v_i - x_j \right\|^2}{\min_{i \neq j} \left\| v_i - v_j \right\|^2}$$

(4.19)

In (4.19), the numerator finds the average distance from various objects to centroids, which is the effective measure of compactness. Similarly, the denominator part finds out the minimum distance between any two centroids, measuring the separation.

A validity-guided re-clustering (VGC) algorithm uses cluster-validity information to guide the clustering process. In this process, the initial clustering is estimated by a soft clustering algorithm and then iteratively altered by applying split-and-merge operations for clusters.

Partition modification that results in an improved partition validity index is retained and an optimum partition result is obtained. The Bensaid partition index is defined as [10]:

$$V_B(U, V) = \sum_{k=1}^{c} \frac{1/n_k \sum_{i=1}^{n} u_{ki}^m \|x_i - v_k\|^2}{n_k \sum_{j=1}^{c} \|v_j - v_k\|^2}$$

(4.20)

Where $n_k$ is the fuzzy cardinality of the $k^{th}$ cluster which is defined as:

$$n_k = \sum_{i=1}^{n} u_{ki}$$

(4.21)

$\sum_{i=1}^{n} u_{ki}^m \|x_i - v_k\|^2$ represents the $k^{th}$ fuzzy cluster variation. The numerator term in (4.20) expresses the compactness. Similarly the denominator component $\sum_{j=1}^{c} \|v_k - v_j\|^2$ signifies the separation of fuzzy cluster $(k)$ as the sum of distances from $k^{th}$ cluster centroid to the centroids of other $(c - 1)$ clusters. It is to be noted that a lower value of partition index indicates a better partition. As $c$ approaches to $n$, the distance component in compactness factor reduces to a very lower values and tends to zero:

61

$$\lim_{c \to n} \|x_i - v_k\|^2 \to 0$$

(4.22)

As a whole, the robustness of compactness factor for determining the optimal number of clusters is lost as $c$ approaches towards $n$. An improved Bensaid index, formulated as Ren index, can be defined as [8]:

$$V_R(U,V) = \sum_{k=1}^{c} \frac{^1/_{n_k} \sum_{i=1}^{n} u_{ik}^m \|x_i - v_k\|^2 + (1/c)\|v_k - \bar{v}\|^2}{(1/(c-1)) \sum_{j=1}^{c} \|v_j - v_k\|^2}$$

(4.23)

The imported second term in numerator of (4.23) works as a punishing function, $\zeta = (1/c)\|v_k - \bar{v}\|^2$. It adds cluster averaged distance from $k^{th}$ cluster centroid ($v_k$) to the average of all other cluster centroids ($\bar{v} = \frac{1}{c}\sum v_c$) with the existing compactness factor in (4.20). This can eliminate the monotonically decreasing tendency as the number of clusters is increased to $n$. The denominator of (4.23) represents separation function as the mean distance from the $k^{th}$ cluster centroid to the other cluster centroids.

The proposed algorithm is dedicatedly designed for segmenting LV from T1 gray converted MRI scans where different object regions have very close pixel weights. Additionally the determination of lateral ventricle boundaries through optimum selection of $V_R(U,V)$ plays a crucial role to detect dimensional changes. The settlement of LV boundary deserves utmost priority as it conveys disease progress information for AD. The punishing function, $\zeta$ in (4.23) should contribute higher value as $c$ approaches $n$ and contribute nominal as $c \ll n$. The $k^{th}$ cluster punishing function contribution is reflected in $V_R(U,V)$ through $\zeta$ in (4.23). As the $k^{th}$ clustering effect is calculated in a single instance, aggregating average values in clustering index estimation is found out to be less accurate. Instead of $\bar{v}$, a modified robust cluster center weighting component is proposed as:

$$v_{\bar{k}} = \left(1/k \sum_{\rho=1}^{k} v_c\right)$$

(4.24)

where $\rho = 1, 2, 3, \dots, k$ is an arbitrary counter variable, $1/k$ is an averaging factor for summed cluster centroids counted upto $k^{th}$ cluster. Here $v_{\bar{k}}$ provides an increasing weight at proposed partition index, $V_{PROPOSED}(U,V)$ as $k \to n$. The modified punishing index $\zeta_{\bar{k}}$ thus becomes:

$$\zeta_{\bar{k}} = \left(\frac{1}{k}\right)\left\|v_k - \left((1/k)\sum_{\rho=1}^{k} v_c\right)\right\|^2$$

(4.25)

Interestingly, a multiplying factor of $(1/k)$ is used in (4.25) instead of $(1/c)$ in (4.23) so as to strengthen the contribution of $\zeta_{\bar{k}}$ in $V_{PROPOSED}(U,V)$ for different values of $k$. However, the proposed multiplying

factor contributes higher weight in $\zeta_{\bar{k}}$ and also keeps robustness of $V_{PROPOSED}(U,V)$ as the ratio of compactness and separation is calculated for single instances of $k$. Now the separation function $\xi_s$ is proposed to be:

$$\xi_s = \sum_{j=1}^{c} \left\| v_k - v_j \right\|^2$$

(4.26)

$\xi_s$ in (4.26) specifies the sum of distances from $k^{th}$ cluster centroid to the centroids of other $(c-1)$ clusters. Eliminating the multiplying factor $(1/(c-1))$ in (4.26) effectively tends to increase $V_{PROPOSED}(U,V)$. This increment minimizes the partition index quality, but averaging $\xi_s$ with $(1/(c-1))$ is not found justified as the ratio of compactness and separation is calculated for single value of $k$. On the other hand, $\zeta_{\bar{k}}$ in $V_{PROPOSED}(U,V)$ will tend to increase the value of compactness. Now the proposed fuzzy clustering index is defined as:

$$V_{PROPOSED}(U,V) = \sum_{k=1}^{c} \frac{1/n_k \sum_{i=1}^{n} u_{ik}^m \|x_i - v_k\|^2 + \zeta_{\bar{k}}}{\xi_s} = \sum_{k=1}^{c} \frac{1/n_k \sum_{i=1}^{n} u_{ik}^m \|x_i - v_k\|^2 + (1/k)\left\|v_k - (1/k \sum_{\rho=1}^{k} v_c)\right\|^2}{\sum_{j=1}^{c} \|v_k - v_j\|^2}$$

(4.27)

The ratio of compactness function and separation function represents the clustering effect of the $k^{th}$ cluster. The summation of clustering effects for all clusters represents the clustering validity index. Lower value of clustering index indicates better clustering effect and the corresponding $c$ is considered to be the optimum number of clusters. Proposed separation factor in (4.27) tends to decrease the overall clustering index which ensures its constancy. Additionally, $\zeta_{\bar{k}}$ tends to increase $V_{proposed}(U,V)$ in (4.27) which preserves robustness of proposed clustering index and provides higher order segmentation accuracy for low contrast brain MRI scans of cerebral atrophy subject. Proposed clustering algorithm has been summarized next:

***Algorithm 4.1:*** *Proposed algorithm*

---

*Input:    MRI of AD subject, s, $I_{max}$ and $\varepsilon$*
*Output: $J_{best}$ , $c_{opt}$ , $U_{best}$*

$D = (d_{ij})_{n \times n}$ ;
$d_c = dis\_cutoff(\varsigma)$ ;   /* quantify the cutoff distance$d_c$ */
$\varsigma = (\varsigma_i)_n$ ;
$idx = arg(sort(\varsigma , descent))$ ;   /* determine the number of objects corresponding to sorted$\varsigma$ */
$k = 1$ ;
$cl = (-1)1 \times n$ ;                           /* cluster number that each object belongs to,  starting from -1. */
   for $i = 1$ to $n-1$ do
     if $cl_{idx_i}! = -1$ && #{$Neighbor(x_{idx_i}) > 1$} then       /* $x_{idx_i}$does not belong to any cluster and the
                                    number of its neighbors is greater than 1. */
        $v_k = x_{idx_i}$ ;
         for $j \in Neighbor(x_{idx_i})$ do
           $cl_j = k$ ;
           $k = k + 1$ ;
           $c_{max} = k$ ;

         for $kn = 2$ to $c_{max}$ do
           $t = 0$ ;                          /* the current iteration */
           $V_{kn}^{(t)} = (v_i)_{kn}$ ;       /* first kn cluster centroids of V */
           $U_{kn}^{(t)} = (u_{ik}^{(t)})_{n \times kn}$ ;
           $J_{kn}^{(t)} = V_{PROPOSED}(U_{kn}^{(t)}, V_{kn}^{(t)})$;       /* Fetch clustering validity index for first kn cluster
                                       centroids */

            while $t == 0 || t < I_{max}$ && $\left| J_{kn}^{(t)} - J_{kn}^{(t-1)} \right| > \varepsilon$ do
              Update $V_{kn}^{(t)}$ ;
              Update $U_{kn}^{(t)}$ ;
              Update $J_{kn}^{(t)}$ ;
              $t = t + 1$ ;
              $Jmin_{kn} = min_{i=1}^{t}(J_{kn}^{(i)})$ ;
              $idx = arg(min_{i=1}^{t}(J_{kn}^{(i)}))$ ;
              $U_{min\,kn} = U_{kn}^{(idx)}$ ;
              $J_{best} = min_{kn=2}^{cmax}(J_{min\,kn})$ ;     /* best value of clustering validity index */
              $c_{opt} = arg(J_{best})$ ;              /* optimum number of cluster centers */
              $U_{best} = U_{min\,c_{opt}}$ ;
            end while;
          end for;
        end for;
      end if;
    end for;

---

## 4.4   Simulation Results

Superiority of the proposed technique is evaluated with a number of T1 brain MRI test images of AD subject. All these test images have been collected from ADNI dataset. Amongst a large test set, five such images with different acquisition plane and MRI slice are demonstrated here for the purpose of comparison. Proposed algorithm is executed in MATLAB R2020a platform with core i5 processor @ 3.60GHz, 8 GB RAM and Windows 10, 64 bit operating system.

**Table 4.1** Imaging parameters of ADNI Test images 1-5.

|  | TI 1 | TI 2 | TI 3 | TI 4 | TI 5 | TI 6 |
|---|---|---|---|---|---|---|
| Type details | T2 FLAIR | PD/T2 FSE | MP-RAGE | MP-RAGE | MP-RAGE | MP-RAGE |
| Acquisition plane | Axial | Axial | Sagittal | Coronal | Axial | Axial |
| Slice | 18 of 35 | 17 of 35 | 85 of 170 | 128 of 256 | 128 of 256 | 156 of 256 |
| ADNI image ID | 569634 | 569634 | 116582 | 116582 | 116582 | 13722 |



**(a)**             **(b)**             **(c)**             **(d)**
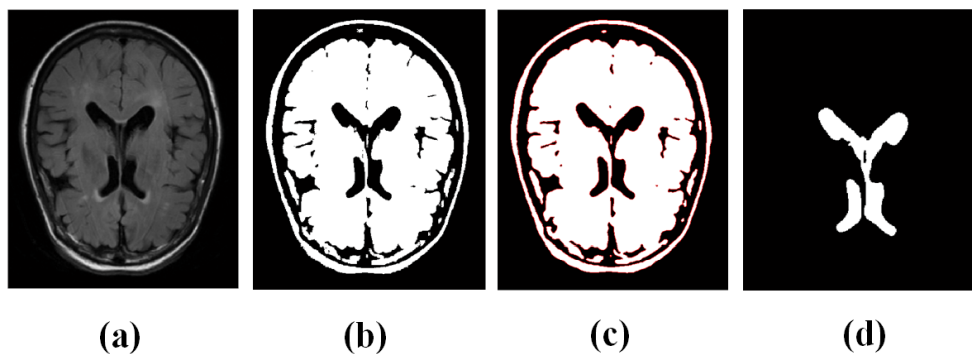
**Fig.4.2** Simulation results of proposed algorithm on Test image 1 (a) original image, (b) MF+FCM, (c) MF+FCM+ACWE, (d) MF+FCM+ACWE – LV segmented.



**(a)**             **(b)**             **(c)**             **(d)**
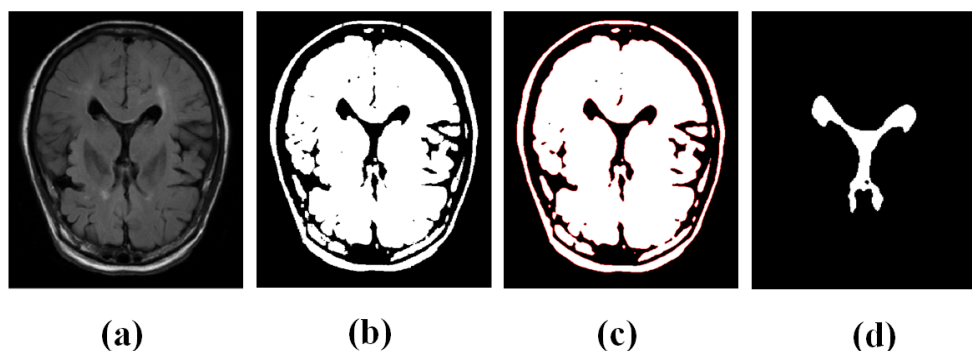
**Fig.4.3** Simulation results of proposed algorithm on Test image 2 (a) original image, (b) MF+FCM, (c)

MF+FCM+ACWE, (d) MF+FCM+ACWE – LV segmented.



**(a)**       **(b)**       **(c)**       **(d)**
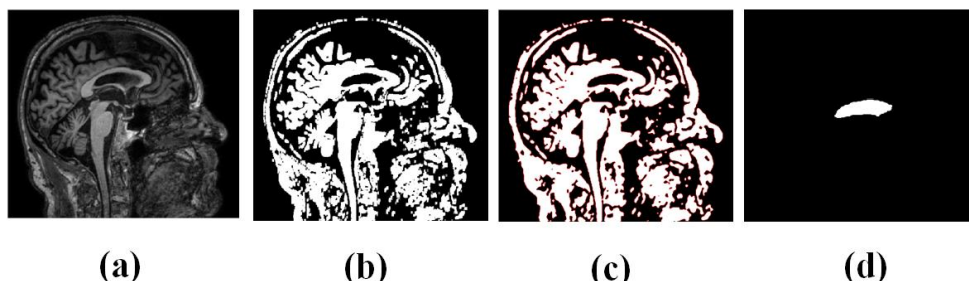
**Fig.4.4** Simulation results of proposed algorithm on Test image 3 (a) original image, (b) MF+FCM, (c) MF+FCM+ACWE, (d) MF+FCM+ACWE – LV segmented.



**(a)**       **(b)**       **(c)**       **(d)**
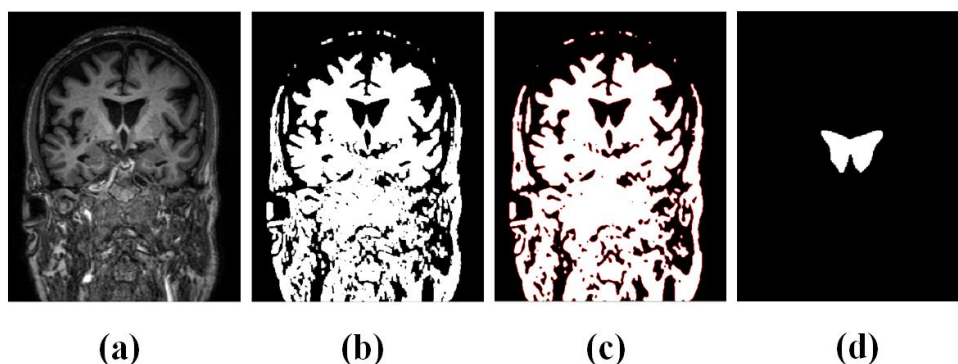
**Fig.4.5** Simulation results of proposed algorithm on Test image 4 (a) original image, (b) MF+FCM, (c) MF+FCM+ACWE, (d) MF+FCM+ACWE – LV segmented.



**(a)**       **(b)**       **(c)**       **(d)**
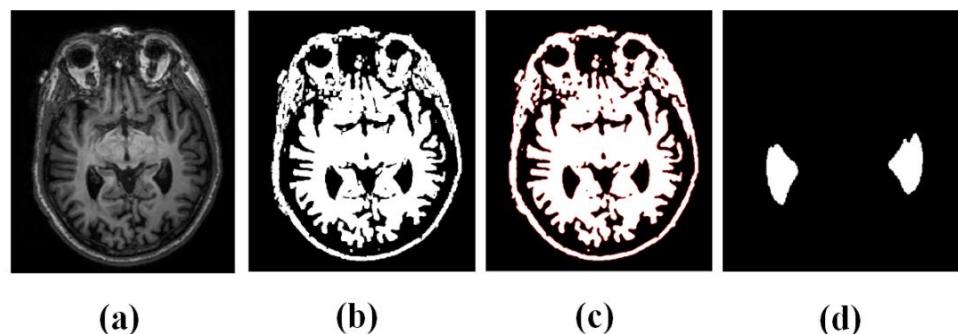
**Fig.4.6** Simulation results of proposed algorithm on Test image 5 (a) original image, (b) MF+FCM, (c) MF+FCM+ACWE, (d) MF+FCM+ACWE – LV segmented.

It is clearly seen that composite implementation of morphological filtering with FCM clustering algorithm eliminates majority of tinny and proxy edges while it retains major edges. Form the simulated results of *TEST IMAGE_01* and *TEST IMAGE_02*; it is evident that gray matter and white matter fine curvatures are mostly eliminated while major ones have been kept on hold in test results. Experimental result mostly helps to concentrate and focus only on ROI which is the ventricular region in this case. As far as the simulation results are concerned, entire ventricular object components appear as connected region which further helps to estimate gross area for the particular MRI slice. It can also be apprehended from simulated results of

*TEST IMAGE_03*, *TEST IMAGE_04* and *TEST IMAGE_05* that LV is classified with major and prominent object boundaries. Thus segmentation of LV is achieved with clinically acceptable higher degree of accuracy.

As the proposed algorithm focuses on ventricular information and represents it as a connected fuzzy clustered dataset, *Structural Similarity Index Measure (SSIM)*, *Jaccard Index (JI) and Pratt's Figure of Merit (FOM)* [11] are found to be best suitable for quantitative analysis. In addition to this, test outcomes of the proposed method are cross analyzed in terms of *Shanon's Entropy.* In particular, most of the quantitative analyzers compare test results with dedicated reference sets. Unlike *JI* or *FOM*, *Shanon's Entropy* calculates a statistical measure of randomness that is used to characterize the texture of test images. Numerical outcomes resulting from this comparison have been illustrated in Table 4.1

To verify the efficiency of the proposed method, test image classification is compared with several other state-of-the-art clustering algorithms like FGFCM_S1 [12], FGFCM_S2 [12], FRFCM [13], ARKFCM [14], EnFCM [15], DSFCM_N [16], FCM_S1 [17] and FCM_S2 [17] along with FCM [17].
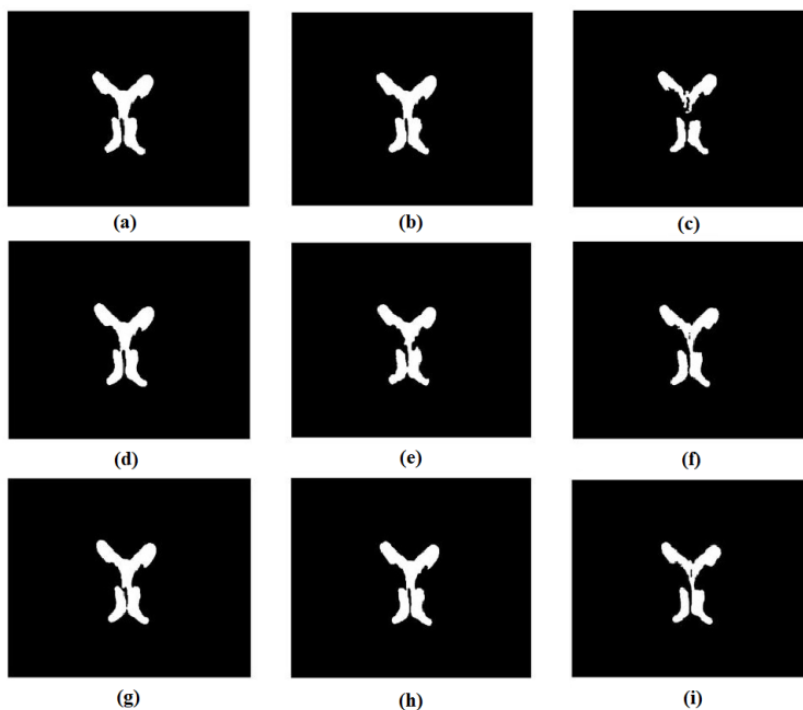


**Fig.4.7** LV segmentation comparison of different clustering algorithm for Test image 1 (a) FGFCM_S1, (b) FGFCM_S2, (c) FRFCM, (d) ARKFCM, (e) EnFCM, (f) DSFCM_N, (g) FCM_S1, (h) FCM_S2, (i) PROPOSED
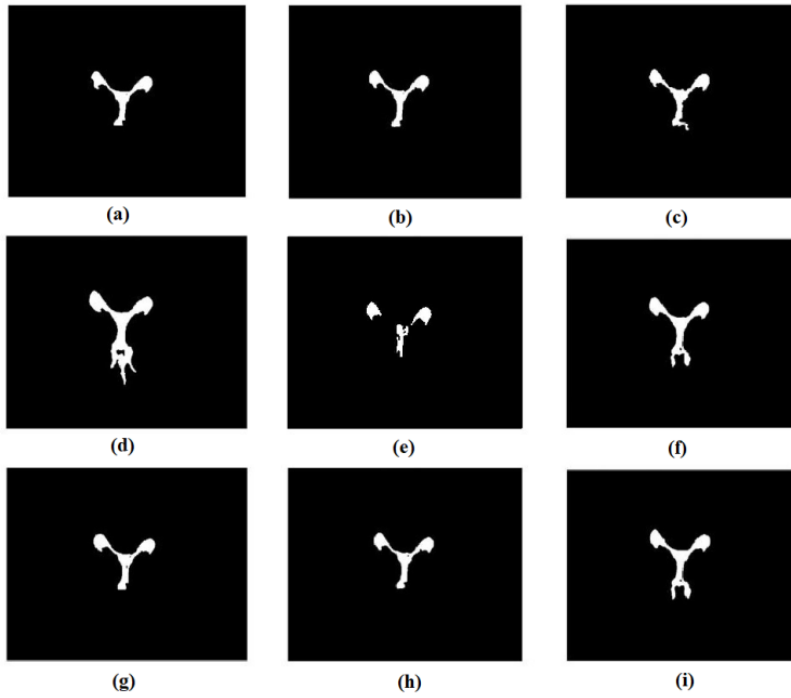
**Fig.4.8** LV segmentation comparison of different clustering algorithm for Test image 2 (a) FGFCM_S1, (b) FGFCM_S2, (c) FRFCM, (d) ARKFCM, (e) EnFCM, (f) DSFCM_N, (g) FCM_S1, (h) FCM_S2, (i) PROPOSED
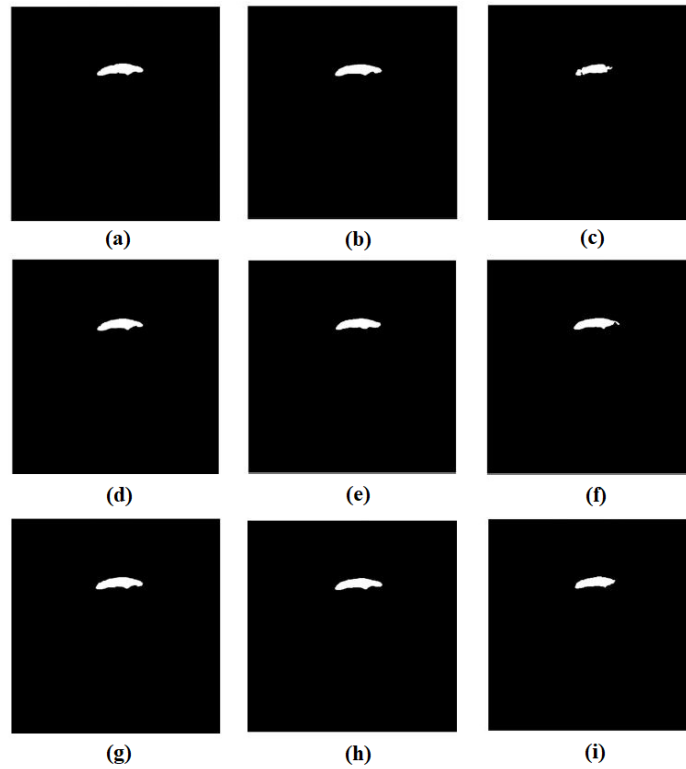


**Fig.4.9** LV segmentation comparison of different clustering algorithm for Test image 3 (a) FGFCM_S1, (b) FGFCM_S2, (c) FRFCM, (d) ARKFCM, (e) EnFCM, (f) DSFCM_N, (g) FCM_S1, (h) FCM_S2, (i) PROPOSED
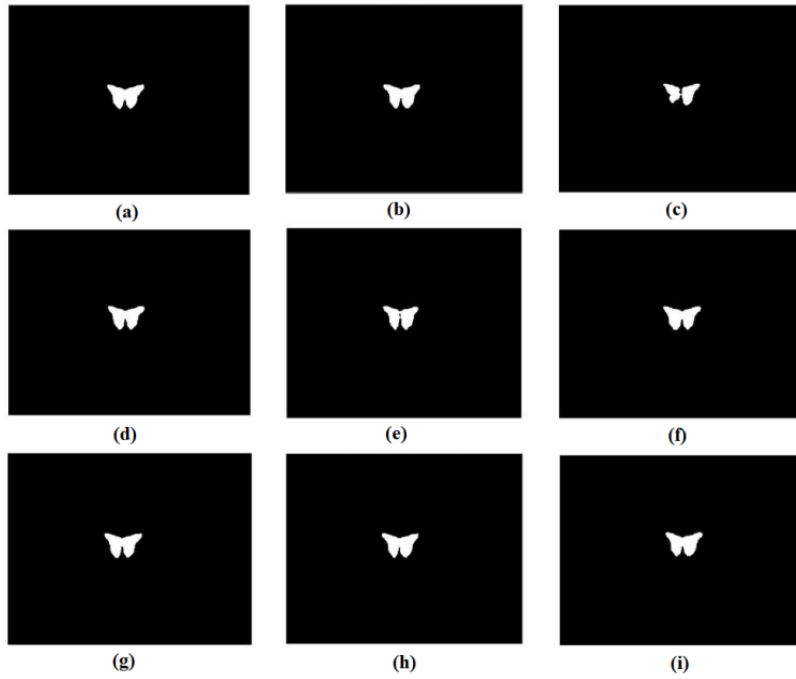
**Fig.4.10** LV segmentation comparison of different clustering algorithm for Test image 4 (a) FGFCM_S1, (b) FGFCM_S2, (c) FRFCM, (d) ARKFCM, (e) EnFCM, (f) DSFCM_N, (g) FCM_S1, (h) FCM_S2, (i) PROPOSED
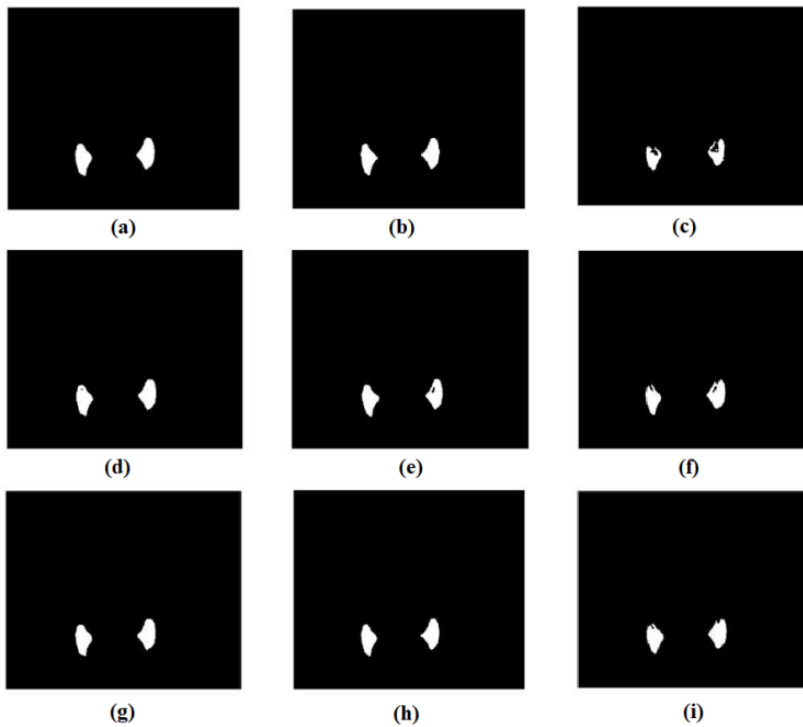


**Fig.4.11** LV segmentation comparison of different clustering algorithm for Test image 5 (a) FGFCM_S1, (b) FGFCM_S2, (c) FRFCM, (d) ARKFCM, (e) EnFCM, (f) DSFCM_N, (g) FCM_S1, (h) FCM_S2, (i) PROPOSED

**Table 4.2** Comparative analysis in terms of SSIM, JI and FOM

| | | SSIM | JI | FOM |
|---|---|---|---|---|
| *TEST IMAGE_01* | FGFCM_S1 | 0.7620 | 0.5765 | 0.5935 |
| | FGFCM_S2 | 0.7799 | 0.6068 | 0.6333 |
| | FRFCM | 0.7575 | 0.5868 | 0.5709 |
| | ARKFCM | 0.7532 | 0.5739 | 0.5693 |
| | EnFCM | 0.7771 | 0.6144 | 0.6252 |
| | DSFCM_N | 0.7844 | 0.6510 | 0.6325 |
| | FCM_S1 | 0.7458 | 0.5497 | 0.5498 |
| | FCM_S2 | 0.7529 | 0.5828 | 0.5692 |
| | PROPOSED | 0.8094 | 0.6525 | 0.6902 |
| *TEST IMAGE_02* | FGFCM_S1 | 0.7881 | 0.6574 | 0.6360 |
| | FGFCM_S2 | 0.7984 | 0.7130 | 0.6629 |
| | FRFCM | 0.7791 | 0.6415 | 0.6176 |
| | ARKFCM | 0.7406 | 0.5469 | 0.5559 |
| | EnFCM | 0.7652 | 0.6008 | 0.5792 |
| | DSFCM_N | 0.8145 | 0.7163 | 0.7084 |
| | FCM_S1 | 0.7764 | 0.6305 | 0.6076 |
| | FCM_S2 | 0.7788 | 0.6485 | 0.6139 |
| | PROPOSED | 0.8309 | 0.8008 | 0.7554 |
| *TEST IMAGE_03* | FGFCM_S1 | 0.7643 | 0.5081 | 0.5297 |
| | FGFCM_S2 | 0.7663 | 0.5079 | 0.5344 |
| | FRFCM | 0.7543 | 0.4968 | 0.4997 |
| | ARKFCM | 0.7606 | 0.5244 | 0.5213 |
| | EnFCM | 0.7740 | 0.5364 | 0.5533 |
| | DSFCM_N | 0.7648 | 0.5127 | 0.5300 |
| | FCM_S1 | 0.7342 | 0.4601 | 0.4558 |
| | FCM_S2 | 0.7456 | 0.4397 | 0.4857 |
| | PROPOSED | 0.7951 | 0.6156 | 0.6052 |
| *TEST IMAGE_04* | FGFCM_S1 | 0.7601 | 0.5502 | 0.5449 |
| | FGFCM_S2 | 0.7687 | 0.5682 | 0.5651 |
| | FRFCM | 0.7567 | 0.5143 | 0.5330 |
| | ARKFCM | 0.7796 | 0.5808 | 0.5918 |
| | EnFCM | 0.7791 | 0.6116 | 0.5889 |
| | DSFCM_N | 0.7897 | 0.6199 | 0.6158 |
| | FCM_S1 | 0.7638 | 0.5242 | 0.5525 |
| | FCM_S2 | 0.7713 | 0.5895 | 0.5717 |
| | PROPOSED | 0.7940 | 0.6555 | 0.6333 |
| *TEST IMAGE_05* | FGFCM_S1 | 0.7495 | 0.6462 | 0.6377 |
| | FGFCM_S2 | 0.7585 | 0.6507 | 0.6546 |
| | FRFCM | 0.7618 | 0.6443 | 0.6578 |
| | ARKFCM | 0.7538 | 0.6324 | 0.6465 |
| | EnFCM | 0.7461 | 0.6095 | 0.6318 |
| | DSFCM_N | 0.7795 | 0.7015 | 0.6974 |
| | FCM_S1 | 0.7549 | 0.6320 | 0.6485 |
| | FCM_S2 | 0.7647 | 0.6596 | 0.6674 |
| | PROPOSED | 0.8064 | 0.7380 | 0.7493 |

Looking at the entries of Table 4.2, it can be inferred that the proposed algorithm results in an SSIM

index improvement of 3.18% to 8.52% over other conventional fuzzy clustering techniques for *TEST IMAGE_01*. Corresponding SSSIM improvement of 2.01% to 12.19% for *TEST IMAGE_02*, 2.72% to 8.29% for *TEST IMAGE_03*, 0.54% to 4.92% for *TEST IMAGE_04* and 3.45% to 8.08% for *TEST IMAGE_05* had also been identified. Improvement quotients in *TEST IMAGE_03* and *TEST IMAGE_04* are comparatively less as the LV appears in smaller volume. As far as the improvement in terms of JI index is concerned, it varies from 0.23% to 18.70% for *TEST IMAGE_01*, 11.79% to 46.42% for *TEST IMAGE_02*, 14.76% to 40% for *TEST IMAGE_03*, 5.74% to 27.45% for *TEST IMAGE_04* and 5.20% to 21.08% for *TEST IMAGE_05* respectively.

Finally, the improvement in terms of FOM is calculated. It is found that the FOM improvement ranges from 8.98% to 25.53%, from 6.63% to 35.88%, from 9.38% to 32.77%, from 2.84% to 18.81% and from 7.44% to 18.59% for *TEST IMAGE_01* to *TEST IMAGE_05* respectively. The improvement quotient in *TEST IMAGE_04* is comparatively less as the LV appears in smaller volume. The proposed method, therefore, fairly segments LV as observed in Fig. 4.7 to Fig. 4.11.

In brief, it can be concluded from Table 4.1 that proposed method exhibits noticeable improvement in terms of SSIM, JI and FOM measures. Advanced methods have been reported in recent years which have introduced significant improvements in detection of various stages of Alzheimer's disease [18, 19]. It can also be inferred that proposed method yields better response in comparison with other fuzzy c-means clustering algorithms in terms of quantitative parameters. In most of the cases, LV is found to be represented by a small area compared to gray matter or white matter or total volume of the brain image.

Variation of entropy with image index has been shown in Fig. 4.12 below for nine different types of fuzzy c-means clustering methods along with the proposed one. Shanon's entropy reveals the information content of the test image. The higher entropy response for proposed method is achieved due to the containment of major boundary edge contours or prominent regions. The fluctuations present in the entropy plot reflect discontinuity in image objects. A higher value of entropy can be achieved due to minor or proxy edge boundary inclusiveness. Similarly lower entropy can reflect loss of major boundary edge contours or prominent                                                                                                                     regions.

(a)



(b)



(c)

72
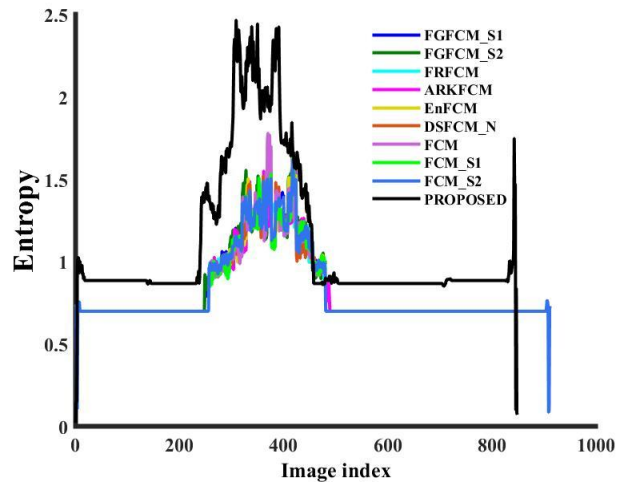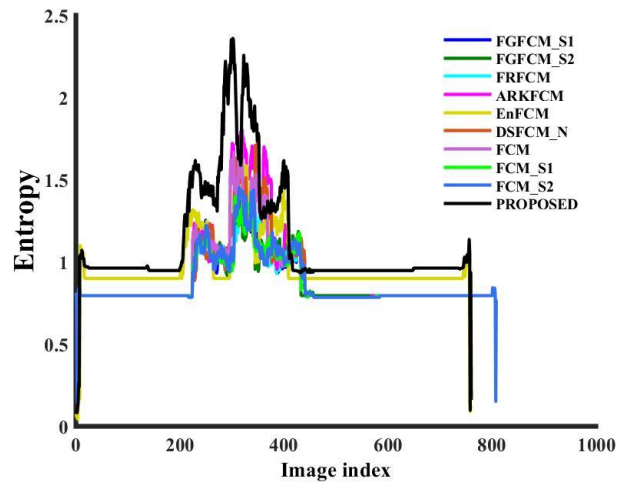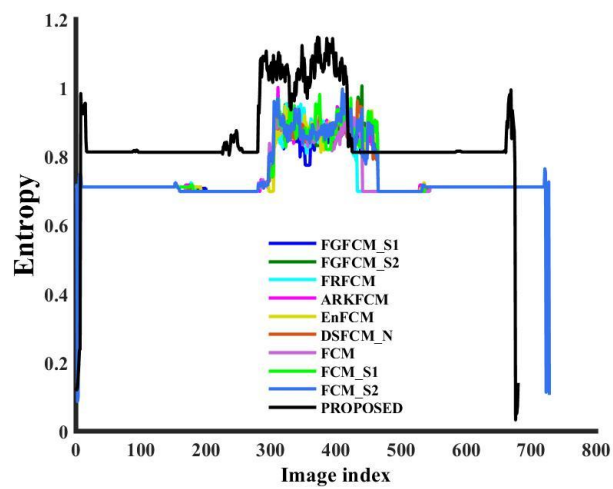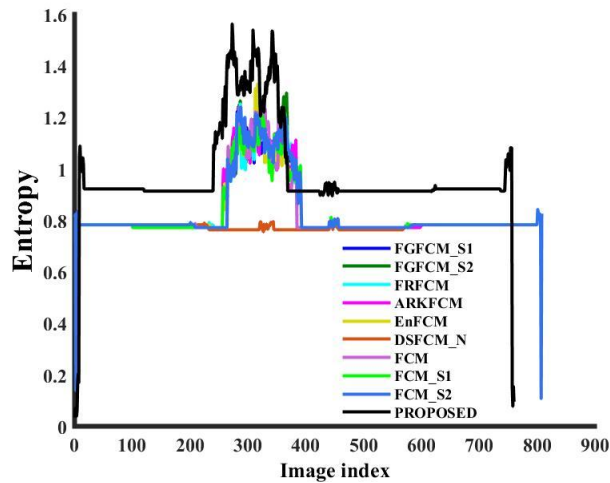
(d)
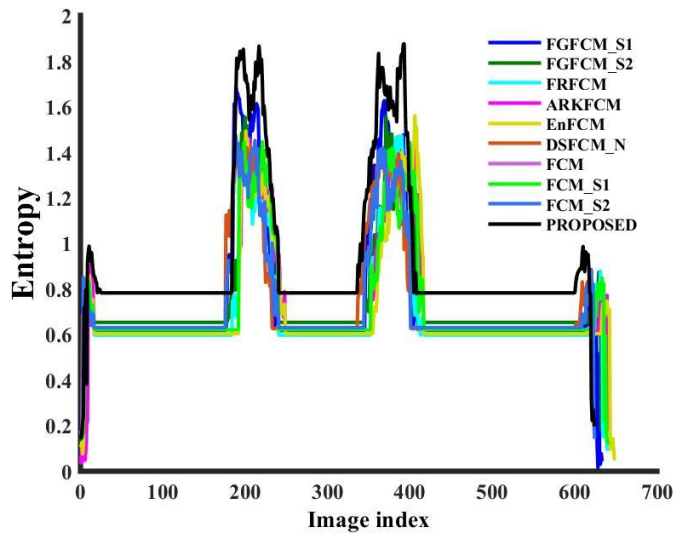


(e)

**Fig.4.12** Entropy plot for: (a) Test image 1, (b) Test image 2, (c) Test image 3, (d) Test image 4, (e) Test image 5

To substantiate the ability of proposed algorithm for classifying HC, MCI and AD in terms of segmented LV, a rigorous test is conducted that provides the LV area information. Simulated results are demonstrated in Table 4.3 for fifty standard ADNI images of HC, MCI and AD subjects. These results are subsequently plotted in Fig. 4.13 where a clear segregation is observed in between HC, MCI and AD.

**Table 4.3** Comparative analysis in terms of SSIM, JI and FOM

| Index | HC | MCI | AD |
|-------|-----|------|-----|
| 1_LV | 1.8154e+05 | 1.9452e+05 | 194312 |
| 2_LV | 181160 | 1.9548e+05 | 1.9451e+05 |
| 3_LV | 1.7872e+05 | 195617 | 1.9465e+05 |
| 4_LV | 1.8192e+05 | 1.9567e+05 | 1.9456e+05 |
| 5_LV | 1.8042e+05 | 1.9162e+05 | 1.9441e+05 |
| 6_LV | 1.7899e+05 | 1.8954e+05 | 1.9418e+05 |

73

| | | | |
|---|---|---|---|
| 7_LV | 1.8135e+05 | 1.9254e+05 | 194696 |
| 8_LV | 180381 | 193285 | 1.9530e+05 |
| 9_LV | 1.7982e+05 | 1.9472e+05 | 1.9580e+05 |
| 10_LV | 1.8128e+05 | 195501 | 1.9593e+05 |
| 11_LV | 1.8053e+05 | 1.9571e+05 | 1.9593e+05 |
| 12_LV | 1.8072e+05 | 195462 | 1.9715e+05 |
| 13_LV | 179275 | 1.9465e+05 | 1.9787e+05 |
| 14_LV | 1.7866e+05 | 1.9333e+05 | 1.9850e+05 |
| 15_LV | 1.7904e+05 | 1.9246e+05 | 1.9881e+05 |
| 16_LV | 1.7978e+05 | 1.9091e+05 | 1.9902e+05 |
| 17_LV | 179199 | 1.9059e+05 | 199147 |
| 18_LV | 1.8005e+05 | 1.9074e+05 | 1.9927e+05 |
| 19_LV | 1.8030e+05 | 1.9081e+05 | 1.9924e+05 |
| 20_LV | 178999 | 1.9122e+05 | 1.9929e+05 |
| 21_LV | 1.8039e+05 | 1.9136e+05 | 199228 |
| 22_LV | 1.8072e+05 | 1.9500e+05 | 1.9913e+05 |
| 23_LV | 1.8061e+05 | 1.9548e+05 | 1.9736e+05 |
| 24_LV | 1.8252e+05 | 1.9604e+05 | 1.9809e+05 |
| 25_LV | 1.8308e+05 | 1.9027e+05 | 1.9851e+05 |
| 26_LV | 180262 | 1.9042e+05 | 1.9865e+05 |
| 27_LV | 1.8219e+05 | 1.9103e+05 | 1.9868e+05 |
| 28_LV | 1.8049e+05 | 1.9181e+05 | 1.9868e+05 |
| 29_LV | 1.8009e+05 | 1.9299e+05 | 1.9451e+05 |
| 30_LV | 1.8029e+05 | 1.9287e+05 | 1.9457e+05 |
| 31_LV | 1.8282e+05 | 192739 | 1.9380e+05 |
| 32_LV | 1.7975e+05 | 1.9237e+05 | 1.9441e+05 |
| 33_LV | 1.7943e+05 | 1.9187e+05 | 1.9474e+05 |
| 34_LV | 1.8239e+05 | 1.9126e+05 | 1.9495e+05 |
| 35_LV | 1.7952e+05 | 1.9055e+05 | 194991 |
| 36_LV | 1.7955e+05 | 192762 | 1.9416e+05 |
| 37_LV | 1.8140e+05 | 1.9358e+05 | 1.9390e+05 |
| 38_LV | 1.8122e+05 | 1.9355e+05 | 1.9421e+05 |
| 39_LV | 1.7986e+05 | 1.9409e+05 | 1.9425e+05 |
| 40_LV | 1.8111e+05 | 1.9503e+05 | 1.9413e+05 |
| 41_LV | 1.8078e+05 | 1.9371e+05 | 194766 |
| 42_LV | 179682 | 1.9331e+05 | 1.9616e+05 |
| 43_LV | 1.7927e+05 | 1.9459e+05 | 1.9664e+05 |
| 44_LV | 1.7900e+05 | 1.9881e+05 | 2.1006e+05 |
| 45_LV | 180682 | 1.9981e+05 | 2.1064e+05 |
| 46_LV | 1.8030e+05 | 2.0401e+05 | 2.1128e+05 |
| 47_LV | 180480 | 1.9879e+05 | 211906 |
| 48_LV | 1.8281e+05 | 1.9364e+05 | 2.1507e+05 |
| 49_LV | 1.8181e+05 | 192764 | 2.1628e+05 |
| 50_LV | 1.8076e+05 | 1.9509e+05 | 2.1692e+05 |
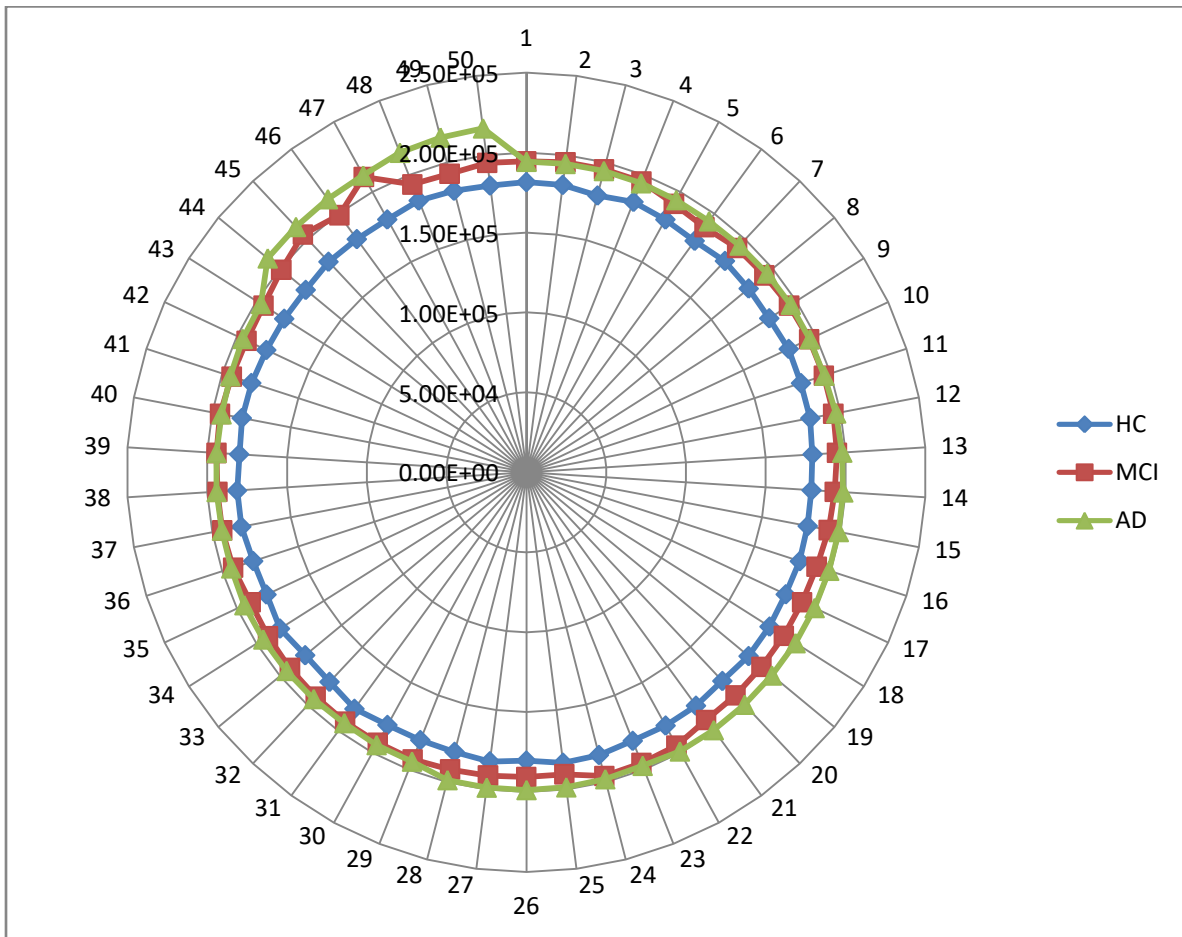
**Fig.4.13** Plot of area information for fifty ADNI images each for HC, MCI and AD

## 4.5 Discussion

In this chapter, a novel combination of a robust morphological image filtering and self adaptive fuzzy c means clustering algorithm is proposed and implemented. The presented method is designed to segregate lateral ventricle form low contrast brain MRI scans of cerebral atrophy subjects. Experimental results exhibit improved segmentation of ventricular regions both visually and quantitatively. Higher entropy response of the presented method identifies that the prominent or major regional boundary information is contained in the output results. The improved quantitative measures indicate that the false or proxy edge detection is avoided. The capacity of proposed method to segregate HC, MCI and AD by LV area information has also demonstrated successfully. With the proper implementation of proposed method, LV appears as a single connected region where selection of appropriate object boundary is ensured. This process leads to detect minor changes due to early intervention of AD.

## REFERENCES

[1]     A. Chandra and S. Mondal, "Amalgamation of iterative double automated thresholding and morphological filtering for early detection of cerebral aneurism," Multimedia tools and Application, Springer, vol. 76, no. 22, pp. 23957–23979, 2017.

[2]     R. C. Gonzalez and R. E. Woods, "Digital Image Processing", 3$^{rd}$ ed., Pearson India.

[3]     J. C. Dunn, "A fuzzy relative of the ISODATA process and its use in detecting compact well-separated clusters," 1973.

[4]     J. C. Bezdek, "Pattern Recognition with Fuzzy Objective Function Algorithms", Springer Berlin Heidelberg, 1981.

[5]     S. Krinidis and V.Chatzis, "A robust fuzzy local information C-means clustering algorithm," *IEEE Transactions on Image Processing*, vol. 19, no. 5, pp. 1328-1337, May 2010.

[6]     T. F. Chan and L. A. Vese, "Active Contours Without Edges," IEEE transactions on Image Processing, vol. 10, pp. 266-277, Feb. 2001.

[7]     P. J. Besl, R. C. Jain, "Segmentation through variable-order surface fitting", IEEE Transactions on pattern analysis and machine intelligence, vol. 10, no. 2, pp. 167-92, 1988.

[8]     M. Ren, P. Liu, Z. Wang and J. Yi, "A self-adaptive fuzzy c-means algorithm for determining optimal number of clusters," Computational Intelligence and Neuroscience, Hindawi, Article ID 2647389, 2016.

[9]     X. L. Xie and G. Beni, "A validity measure for fuzzy clustering," IEEE Transactions on Pattern Analysis and Machine Intelligence, vol. 13, no. 8, pp. 841–847, 1991.

[10]    A. M. Bensaid, L. O. Hall, J. C. Bezdek, L. P. Clarke, M. L. Sibiger, J. A. Arrington et al., "Validity-guided (re)clustering with applications to image segmentation," IEEE Trans on Fuzzy Sys, vol. 4, no. 2, pp. 112–123, 1996.

[11]    S. Pereira, A. Pinto, V. Alves, and C. A. Silva, ''Brain tumor segmentation using convolution neural networks in MRI images,'' IEEE Transactions on Medical Imaging, vol. 35, no. 5, pp. 1240–1251, May 2016.

[12]    M. N. Ahmed, S. M. Yamany, N. Mohamed, A. A. Farag, and T. Moriarty, "A modified fuzzy c-means algorithm for bias field estimation and segmentation of mri data," IEEE transactions on medical imaging, vol. 21, no. 3, pp. 193–199, 2002.

[13] T. Lei, X. Jia, Y. Zhang, L. He, H. Meng, and K. N. Asoke, "Significantly fast and robust fuzzy c-means clustering algorithm based on morphological reconstruction and membership filtering," IEEE Trans. Fuzzy Syst., vol. 26, no. 5, pp. 3027–3041, Oct. 2018.

[14] R. Fang, Y. Lu, X. Liu, and Z. Liu, "Segmentation of brain MR images using an adaptively regularized kernel FCM algorithm with spatial constraints," 10th International congress on image and signal processing, Biomedical Engineering and Informatics (CISP-BMEI 2017), 2017.

[15] M. Gong, Y. Liang, J. Shi, W. Ma, and J. Ma, "Fuzzy c-means clustering with local information and kernel metric for image segmentation," IEEE transactions on image processing, vol. 22, no. 2, pp. 573–584, 2012.

[16] Y. Zhang, X. Bai, R. Fan, and Z. Wang, "Deviation-sparse fuzzy c-means with neighbor information constraint," IEEE Transactions on Fuzzy Systems, vol. 27, no. 1, pp. 185–199, 2018.

[17] M. N. Ahmed, S. M. Yamany, N. Mohamed, A. A. Farag, and T. Moriarty. "A modified fuzzy c-means algorithm for bias field estimation and segmentation of MRI data," IEEE transactions on medical imaging, vol. 21, no. 3, pp. 193–199, 2002.

[18] S. Liang, Y. Gu, "Computer-aided diagnosis of Alzheimer's Disease through weak supervision deep learning framework with attention mechanism," Sensors, vol. 21, no. 1, pp. 220, 2020.

[19] A. Shah, D. Lalakiya, S. Desai, Shreya and V. Patel, "Early Detection of Alzheimer's Disease Using Various Machine Learning Techniques: A Comparative Study," 4th International Conference on Trends in Electronics and Informatics (ICOEI)(48184), Tirunelveli, India, pp. 522-526, 2020.

# Chapter 5

# An Adaptive Neighbor Constrained Deviation Sparse Variant Fuzzy C-Means Clustering Algorithm for Brain MRI of AD Subject

## 5.1 Introduction

Progression of early Alzheimer's disease (AD), the mild cognitive impairment (MCI) bears a close proximity with the tissue loss in certain regions of brain, especially in medial temporal lobe (MTL). For taking appropriate medical intervention, MCI can be traced by diagnosing the structural changes in brain MRI scans with advanced fuzzy c-means clustering algorithm. In this chapter, initially a very low intensity rician noise is imposed on brain MR scans of AD subject that too sparsity is incorporated in the clustering method. A novel method of neighbor pixel constrained fuzzy c-means clustering strategy is implemented where topology based selection of parsimonious neighbor pixel is automated. The adaptability in selection of neighbor pixel class provides more accurate object edge boundary which outperforms other clustering output. The proposed adaptive neighbor constrained deviation sparse variant fuzzy c-means clustering (AN_DsFCM) can withhold incorporated sparsity constraints. Experimental results are compared with several state of the art fuzzy clustering methods for test MRI scans. Visual study and statistical measures are evaluated to meet image processing and clinical neurophysiology standards. It has been proved that the performance of AN_DsFCM is significantly better than other clustering methods.

## 5.2 Initial Works

### 5.2.1 Fuzzy C-means (FCM)

Let us consider a finite data set $X = (x_1, x_2, \dots, x_m)$ where each object $x_j$ is an $l$- dimensional vector. FCM segregates m patterns or objects into $c$ number of clusters through an iterative minimization process. The objective function of the FCM is represented as shown below [1]:

$$J_m^{FCM}(U,V) = \sum_{j=1}^{c} \sum_{i=1}^{m} u_{i,j}^r \|x_i - v_j\|_2^2$$

(5.1)

Where $U = \{u_{ij}\}, j = 1, \dots, c$ and $i = 1, \dots, m$ represents the membership separation matrix with the constraint $\sum_{j=1}^{c} u_{ij} = 1$ for all $i = 1, \dots, m; V = \{v_1, v_2, \dots, v_c\}$ is the vector for cluster center; r ($>1$) is called the fuzzy factor and is generally set to 2. FCM uses an alternative optimization process to achieve optimal condition such as:

$$U^{(t+1)} = argmin\, J_m^{(FCM)}(U, V^{(t)})$$

(5.2)

$$V^{(t+1)} = argmin\, J_m^{(FCM)}(U^{(t+1)}, V)$$

(5.3)

where $t$ signifies iteration number. FCM randomly initializes $U^0$, $V^0$ and updates $U$ and $V$ alternatively till convergence. The membership partition or separation matrix and the vector of cluster center are obtained by using Langrage multiplier theorem as follows:

$$u_{ij}^{(t+1)} = \left( \sum_{k=1}^{c} \left( \frac{\left\|x_i - v_j^{(t)}\right\|_2^2}{\left\|x_i - v_k^{(t)}\right\|_2^2} \right)^{\frac{1}{m-1}} \right)^{-1}$$

(5.4)

$$v_j^{(t+1)} = \frac{\sum_{i=1}^{n} \left(u_{ij}^{(t+1)}\right)^m x_j}{\sum_{i=1}^{n} \left(u_{ij}^{(t+1)}\right)^m}$$

(5.5)

FCM provides better result for noise free data. However, it is unable to give proper cluster to data associated with artifacts such as noise and outliers. Due to lack of spatial information, FCM is generally sensitive to noise.

## 5.2.2 Modified FCM

A bias correction fuzzy C means method is proposed by Ahmed *et al.* [2] where a bias field in FCM for clustering of the data is used. The objective function is defined as follows:

$$J_m^{(BCFCM)}(U,V,\beta) = \sum_{j=1}^{c}\sum_{i=1}^{N} u_{ij}^m \|x_j - \beta_j - v_i\|_2^2 + \frac{\alpha}{N_R}\sum_{j=1}^{c}\sum_{i=1}^{N} u_{ij}\left(\sum_{r\epsilon N_w} \|x_r - \beta_j - v_i\|_2^2\right)$$

(5.6)

where $N_w$ is the cardinality of the local window used, $\alpha$ is a smoothing parameter, $\beta$ and $\beta_r$ are estimated additive bias field for pixel $i$ and its neighbor pixel $r$ respectively. This method does not use the sparsity on $\beta_j$, and hence makes the estimation unreasonable and unstable.

## 5.2.3   Fuzzy Local Information c-means Method (FLICM)

Krinidis and Chatzis proposed the robust fuzzy local information c means method (FLICM) [3]. They introduced a novel fuzzy factor $G_{ij}$ which is defines as:

$$G_{ij} = \sum_{r\epsilon N_w} \frac{1}{(1+d_{jr})}(1-u_{ir})^m \|x_r - v_i\|_2^2$$

(5.7)

where $N_w$ is the local window for central pixel $j$ and $r$ is the neighbor pixel around $j$. $d_{jr}$ is the Eucledian distance between $j$ and $r$. $u_{ir}$ represents the membership function for neighbor pixel $r$ to belong to the $i$-th cluster. The objective function along with $G_{ij}$ is given below:

$$J_m^{(FLICM)}(U,V,\beta) = \sum_{j=1}^{c}\sum_{i=1}^{n} [u_{ij}^m \|x_j - v_i\|_2^2 + G_{ij}]$$

(5.8)

The FLICM is appropriate for image affected by noise or outliers. The fuzzy factor $G_{ij}$ remains as constant in each iterative step of the framework if the neighbor membership function $u_{ir}$ interacts with $u_{ij}$. Some recent studies suggest that iterative updating formula of FLICM does not have enough ability to minimize the objective function [3].

## 5.2.4 Deviation Sparse Fuzzy C-Mean Clustering (DSFCM)

Yuxuan Zhag [4] proposed the Deviation Sparse Fuzzy C-Mean Clustering (DSFCM) by introducing sparse. It is seen that interference generally occurs during acquisition and transmission of data. As a matter of fact, the measured data vector $x_{\Delta j}$ deviates from its theoretical value $x_j$. The difference between $x_j$ and $x_{\Delta j}$ is called error and represented as $e_j$. So $x_{\Delta j}$ can be written as

$$x_{\Delta j} = x_j - e_j$$

(5.9)

By introducing sparsity on deviation matrix $E$ and utilizing $x_{\Delta j}$ for clustering in FCM, the objective function of DSFCM is defined as follows:

$$J_m^{(DSFCM)}(U,V,\beta) = \sum_{j=1}^{c}\sum_{i=1}^{n} u_{ij}^m \left\| x_j - e_j - v_i \right\|_2^2 + \sum_{p=1}^{l} \lambda_q \left\| E_p \right\|_q^q$$

(5.10)

expanding the above equation:

$$J_m^{(DSFCM)}(U,V,\beta) = \sum_{j=1}^{c}\sum_{i=1}^{n} u_{ij} \left\| x_j - e_j - v_i \right\|_2^2 + \sum_{p=1}^{l} \lambda_q \sum_{i=1}^{n} \left\| e_{jp} \right\|_q^q$$

(5.11)

Optimization of the DSFCM is carried out like FCM. The optimal condition is obtained as:

$$U^{(t+1)} = argmin\, J_m^{(DSFCM)}(U,V^{(t)},E^{(t)})$$

(5.12)

$$V^{(t+1)} = argmin\, J_m^{(DSFCM)}(U^{(t+1)},V,E^t)$$

(5.13)

$$E^{(t+1)} = argmin\, J_m^{(DSFCM)}(U^{(t+1)},V^{(t+1)},E^t)$$

(5.14)

By applying Lagrange multiplier method to equation (5.10), the iterative formulae for $U$ and $V$ are obtained as follows:

$$u_{ij}^{(t+1)} = \left( \sum_{k=1}^{c} \left( \frac{\left\| x_j - e_j^{(t)} - v_i^{(t)} \right\|_2^2}{\left\| x_j - e_j^{(t)} - v_k^{(t)} \right\|_2^2} \right) \right)^{-1}$$

(5.15)

$$v_{iq}^{(t+1)} = \frac{\sum_{i=1}^{n} (u_{ij}^{(t+1)})^m (x_{jq} - e_{jq}^t)}{\sum_{i=1}^{n} (u_{ij}^{(t+1)})^m}$$

<div align="right">(5.16)</div>

# 5.3 Adaptive Neighbor Information Constrained DSFCM (AN_DsFCM)

To improve the clustering performance, adaptive neighbor information constrained *DSFCM* is proposed in this chapter. In the proposed algorithm, influence of neighbor pixels has been estimated in the objective function. Let us consider,

$$d_0 = \left\| x_i - v_j \right\|_2^2$$
$$d_m = mean_{r \in N_i, r \neq i} \left\| x_r - v_j \right\|_2^2$$
$$d_t = \left\| d_m - d_0 \right\|_2^2$$

<div align="right">(5.17)</div>
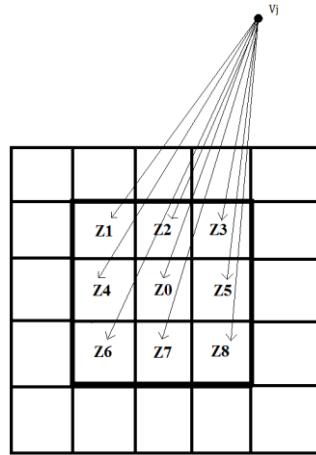


**Fig. 5.1** Relationship between central pixel and its neighbor pixel
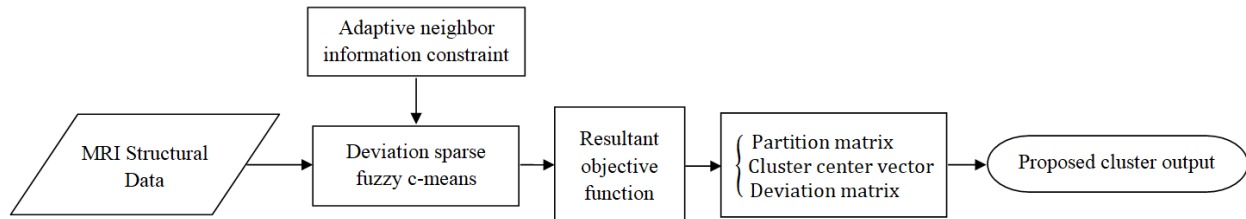


**Fig. 5.2** Graphical abstract of proposed AN_DsFCM

The aim is to segregate a subset $r'$ $(r' \in r)$ which is having larger probability to belong to $j$-th cluster. This is done by robust selection of distance measure parameters. Let us consider that $d'_r$ is the distance measure parameter associated with $r'$. Now considering $r \in N_i$ and $r \neq i$, let us set a relation among distance between neighboring pixel and current cluster center such that:

$$d'_r = \{\|x_i - v_j\|_2^2, (r' \subseteq r)$$
$$\text{and} \quad [(d_0 + d_t) > \|x_i - v_j\|_2^2 \geq (d_0 - d_t)]\}$$

(5.18)

Now considering $x'_r$ and associated error $e'_r$, the modified $d'_r$ will be:

$$d'_r = \{\|x'_r - e'_r - v_j\|_2^2\}$$

(5.19)

So, the first term of the objective function becomes:

$$J'_1 = \sum_{j=1}^{c} \sum_{i=1}^{n} u_{ij}^m \frac{1}{n(r')} \left( \sum_{r \in N_j} \|x'_r - e'_r - v_j\|_2^2 \right)$$

(5.20)

where $n(r')$ is the number of elements in $r'$. Now imposing sparsity on E, the second term of proposed *AN_DsFCM* becomes:

$$J'_2 = \sum_{q=1}^{l} \lambda_q \sum_{r' \in N_j} \frac{\sum_{i=1}^{n} \|e_{iq}\|^p}{1 + d_{r'i}}$$
$$\text{where} \quad d_{r'i} = \|x_{r'} - x_i\|_2^2$$

(5.21)

Now the proposed objective function is constructed as:

$$J'' = J'_1 + J'_2$$

(5.22)

So, the objective function of proposed *AN_DsFCM* becomes:

$$J'' = \sum_{j=1}^{c} \sum_{i=1}^{n} u_{ij}^m \frac{1}{n(r')} \left( \sum_{r \in N_j} \|x'_r - e'_r - v_j\|_2^2 \right) + \sum_{q=1}^{l} \lambda_q \sum_{r' \in N_j} \frac{\sum_{i=1}^{n} \|e_{iq}\|^p}{1 + d_{r'i}}$$

(5.23)

where $N_i$ represents a 3×3 local window centered at $i$.

Now the constraint $\sum_{r \in N_i} \|x_r' - e_r' - v_j\|_2^2$ in first term of equation (5.23) computes the summation of spatial weighted Eucledian distances between $j$-th cluster center and some selected neighbouring pixels as determined in equation (5.20). The closeness of $d_r$ towards $d_0$ determines the affinity of respective neighbour pixel to be included into same cluster that $i$ belongs to. The summation constraint is averaged out by multiplying it with $1/n(r')$. This attribute keeps the justified weight balance in proposed objective function. Since the effect of $r$ on $r'$ is not relayed in $u_{ij}^m$, it is relatively free from any influence and only relies on center pixel. The theoretical value of selective neighbor pixel $r'$ is estimated by eliminating successive error coefficients $e_r'$ so that it becomes $(x_r' - e_r')$. This incorporates robustness to rician noise or outliers in $J''$. Now the multiplying coefficient $1/1 + d_{r'j}$ in the second term of (5.23) reflects the error influence of neighbouring pixel depending on spatial distance from central pixel.

Now by adopting Lagrange multiplier theorem, Lagrange objective function can be constructed as:

$$L = \sum_{j=1}^{c} \sum_{i=1}^{n} u_{ij}^m \frac{1}{n(r')} \left( \sum_{r \in N_j} \|x_r' - e_r' - v_j\|_2^2 \right) + \sum_{q=1}^{l} \lambda_q \sum_{r' \in N_j} \frac{\sum_{i=1}^{n} \|e_{iq}\|^p}{1 + d_{r'i}} + \sum_{i=1}^{n} \mu_i \left( \sum_{j=1}^{c} u_{ij} - 1 \right)$$

(5.24)

where $\mu_i$ represents Lagrange multiplier. Now by fixing E, derivative of L is obtained with respect to $u_{ij}$, $v_j$ and $\mu_i$. By making these derivatives to zero, membership partition matrix and cluster center vector may be computed as shown below:

$$u_{ij}^{(t+1)} = \left( \sum_{k=1}^{c} \left( \frac{\sum_{r \in N_i} \|x_r' - e_r'^{(t)} - v_j^{(t)}\|_2^2}{\sum_{r \in N_i} \|x_r' - e_r'^{(t)} - v_k^{(t)}\|_2^2} \right)^{\frac{1}{m-1}} \right)^{-1}$$

(5.25)

$$v_j^{(t+1)} = \frac{\sum_{i=1}^{n} (u_{ij}^{(t+1)})^m \sum_{r' \in N_i} (x_r' - e_r'^{(t)})}{\sum_{r' \in N_i}^{n} \sum_{i=1}^{n} (u_{ij}^{(t+1)})^m}$$

(5.26)

To estimate the error $E$, both the components $e_i = (e_{i1}, e_{i2}, e_{i3}, \dots, e_{iq}, \dots, e_{il})$ and $e_r$ are not mutually exclusive to each other. $e_r$ cannot be considered as a constant while solving for $E$. Now being the adjacent neighbour, both $i$ and $j$ have mutual error influence on each other. So, in error

image space, $r \in N_i \cong i \in N_p$. While calculating the error influence around $i$-th pixel, we can infer that

$$\sum_{i=1}^{n} u_{ij}^{m} \left( f(e_i) + \sum_{r' \in N_i} f(e_r) \right) = \sum_{i=1}^{n} \sum_{r' \in N_i} u_{ir'}^{m} (f(r))$$

(5.27)

The error function is in $r$ other than $r'$ while $r'$ is eliminated as it has a minimal chance to retain in the same cluster where the $i$-th pixel currently retains. f(∙) in equation (5.27) is a function associated with $e_i$ and $e_r$. By using equation (5.27), we can rewrite equation (5.23) as:

$$J'' = \sum_{j=1}^{c} \sum_{i=1}^{n} u_{ij}^{m} \frac{1}{n(r')} \left( \sum_{r \in N_j} \| x_i' - e_i' - v_j \|_2^2 \right) + \sum_{q=1}^{l} \lambda_q \sum_{r' \in N_j} \frac{\sum_{i=1}^{n} \| e_{iq} \|^p}{1 + d_{r'i}}$$

(5.28)

For optimization of $E$, equation (5.28) can be decomposed into $n \times l$ sub problems as follows:

$$e_{iq}^{(t+1)} = argmin \sum_{j=1}^{c} \sum_{r' \in N_i} \frac{\left( u_{ir}^{(t+1)} \right)^m \left\| x_{iq}' - e_{iq}' - v_{jq}^{(t+1)} \right\|^2}{1 + d_{r'i}} + \sum_{r' \in N_i} \frac{\lambda_q \| e_{iq} \|^p}{1 + d_{r'i}}$$

(5.29)

The error matrix $E$ of the AN_DsFCM can be solved by using soft thresholding as below:

$$e_{iq}^{(t+1)} = \frac{soft \left( A, \dfrac{\lambda_q/2}{\sum_{r' \in N_i} (1 + d_{r'i})} \right)}{\sum_{j=1}^{c} \sum_{r' \in N_i} \dfrac{1}{1 + d_{r'i}} (u_{ir}^{(t+1)})}$$

(5.30)

where $A$ is given by:

$$A = \sum_{j=1}^{c} \sum_{r' \in N_i} \left( \frac{u_{ir}^{(t+1)m} (x^{iq} - v_{jq}^{(t+1)})}{1 + d_{r'i}} \right)$$

(5.31)

In the proposed AN_DsFCM algorithm, $N_i$ has been employed as a local window. Due to the introduction of sparse in the proposed algorithm, it becomes more sensitive to identify noise and can estimate a more accurate cluster center. Proposed algorithm has been illustrated by means of a block diagram in Fig. 5.2.

_____

***Algorithm 5.1:*** *Pseudo code for Adaptive Neighbour Information constrained DsFCM*

_____

**Input**: Intensity dataset $= (x_1, x_2, \dots, x_m)$, parameter vector $\lambda$.

**Initialize**: Candidate fuzzy factor $r$, permitted threshold $\varepsilon$, number of cluster $c$, window size $N_i$, Initial membership partition matrix $U^0$, error matrix $E=0$, loop counter $t=0$.

Step 1: Dimensional indices: *[$i_{max}$ ,$j_{max}$] = dim(X)*
Step 2: for *i = 2 to ($i_{max}$ - 1)*
        for *j= 2 to ($j_{max}$-1)*
            Update $d_0$, $d_n$, $d_m$ & $d_t$ using (5.17)
            Update $r' \in r$ where $r \in N_i$, $r \ne i$
             such that $(d_m + d_t) > d'_r \ge (d_m - d_t)$ using (5.18)
            Update $e'_r$ associated to $r'$ (5.19)
            Update $J'_1$ using (5.20)
            Update $d_{r'\,i}$ using (5.22) & $\lambda_q$ using (5.34)
            Update $J'_2$ using (5.21)
            Update resultant objective function $J''$ using (5.23)
            Update $U^{(t+1)}$ using (5.25) & $V^{(t+1)}$ using (5.26)
            Update deviation matrix $e^{(t+1)}$ using (5.30)
            Update loop counter $t$
             If $abs[U_t - U_{t+1}] < \varepsilon$ then terminate, otherwise rewind to Step 2
          end for
        end for

**Output**: Terminal partition matrix $U$, closing cluster center $V$ and estimated deviation matrix $E$.

_____

It can be seen from equation (5.30) that $\lambda_q$ is an important parameter in the proposed algorithm. As a matter of fact, appropriate selection of $\lambda_q$ is required for better clustering performance. The soft thresholding operator has the following property

$$soft\left(a, \frac{\lambda_q}{2}\right) = \frac{soft\left(ka, \frac{k\lambda_q}{2}\right)}{k}, \quad (k > 0)$$

(5.32)

Using this property, it can be found that

$$e_{jq}^{(t+1)} = \frac{soft\left(\dfrac{\sum_{j=1}^{c}\sum_{r'\in N_i}\dfrac{1}{1+d_{r'i}}\left(u_{ir}^{(t+1)}\right)^m\left(x_{iq}-v_{iq}^{(t+1)}\right),\dfrac{\lambda_q}{2}}{\sum_{r'\in N_i}(1+d_{r'i})}\right)}{\sum_{j=1}^{c}\sum_{r'\in N_i}\left(\dfrac{1}{1+d_{r'i}}\left(u_{ir}^{(t+1)}\right)\right)/\sum_{r'\in N_i}\dfrac{1}{1+d_{r'i}}}$$

(5.33)

where $\lambda_q = [\lambda_{q1}, \lambda_{q2}, \lambda_{q3}, \dots, \lambda_{ql}]$ is used as deviation tolerance distance vector.

Let us assume that the measured data is close to center $v_i$ and if the weighted distance between $x_i$ and $v_i$ becomes $\Delta\lambda_q$ then the other extra part will be considered as an error. When the weighted distance between a point to its cluster center crosses $\Delta\lambda_q$ (where $\Delta\lambda_q$ is different for different point corresponding to center), the rest fragment is considered as noise or outlier.
In this experiment, $\lambda_q$ has been chosen as follows:

$$\Delta\lambda_q = 0.8\,\sigma_q, \quad q = 1, \dots, l$$

(5.34)

where $l$ is the dimension of observed data and $\sigma_q$ is the standard deviation in $q$-th channel. In view of conserving majority of data population in dispersion of $\sigma_q$, a multiplying factor of 80% is justified for brain MR scans. Proposed algorithm has been tested in different MRI and fMRI scans and it is found that $\Delta\lambda_q$ achieves good performance.

## 5.4 Simulation Results

Performance of the proposed algorithm is analyzed through qualitative discussion and visual impression. Behavior of AN_DsFCM has also been evaluated in terms of quantitative metrics such as structural similarity index measure (SSIM), dice coefficient (DC), segmentation accuracy (SA), sensitivity and jaccard index (JI) to assess the clustering efficiency [5]. The proposed clustering method is adopted to cross-analyze in terms of figure of merit (FOM) and Shanon's entropy response [6, 7]. In addition to this, the performance of proposed algorithm is evaluated with several other well established fuzzy clustering methods including FCM_S1 [8], FCM_S2 [8], FCMLSM [9], FGFCM_S1 [8], FGFCM_S2 [8], FRFCM [10], ARKFCM [11], EnFCM [12] and DSFCM_N [4].

There are a few advanced methods reported for classification of Alzheimer's disease in recent years [13 - 15]. Proposed algorithm is tested on a large dataset of brain MRI scans focused on AD and MCI subjects. To demonstrate the performance of proposed algorithm, twelve such MRI test images from ADNI database and eight more real time images are taken into consideration for the purpose of illustration. All the images are deliberately chosen with different subject, series, patient age, slice and acquisition plane which are abbreviated in Table 5.1 and 5.2. MATLAB R2019a platform with core i5 processor @3.6 GHz, 8GB RAM and Windows 10 Professional 64 bit operating system has been successfully used for analyzing the images by means of proposed algorithm.

**Table 5.1** Imaging parameters for Test images 1-6

|  | **TI 1** | **TI 2** | **TI 3** | **TI 4** | **TI 5** | **TI 6** |
|---|---|---|---|---|---|---|
| ADNI image ID | 569634 | 569634 | 116582 | 116582 | 116582 | 13722 |
| Type details | T2 FLAIR | PD/T2 FSE | MP-RAGE | MP-RAGE | MP-RAGE | MP-RAGE |
| Acquisition plane | Axial | Axial | Sagittal | Coronal | Axial | Axial |
| Slice | 18 of 35 | 17 of 35 | 85 of 170 | 128 of 256 | 128 of 256 | 156 of 256 |

**Table 5.2** Imaging parameters for Test images 7-12

|  | **TI 7** | **TI 8** | **TI 9** | **TI 10** | **TI 11** | **TI 12** |
|---|---|---|---|---|---|---|
| ADNI image ID | 13722 | 13721 | 13721 | 13721 | 13721 | 863060 |
| Type details | MP-RAGE | MP-R R | MP-R R | MP-R R | MP-R R | MP-R R |
| Acquisition plane | Axial | Sagittal | Sagittal | Coronal | Coronal | Coronal |
| Slice | 164 of 256 | 70 of 166 | 102 of 166 | 100 of 256 | 90 of 256 | 122 of 256 |

The base pixel neighbor information constraint is ignored for all nine clustering techniques except DSFCM_N. The fuzzy clustering window is fixed at 3×3 with a common constant fuzzy factor for all eight methods. All the test images in DSFCM_N are examined by exposing them to

Gaussian noise, salt & pepper noise, uniform noise and mixed noise. The proposed AN_DsFCM is designed to mitigate the accuracy requirement for MR images. Thus, in proposed demonstration, a very low intensity rician noise is imposed on all the AD test MRI images and tested further.

Comparative analysis among different clustering methods has been presented qualitatively in Fig. 5.3 to 5.14 and quantitatively in Table 5.3 to 5.24 respectively. In order to analyze the computational complexity of different techniques, time complexity has been depicted in Table 5.25. Looking at those images, it can be identified that the GM and WM boundaries are bold and contrast is significantly enhanced for AN_DsFCM compared to other clustering methods. The LV region is clear and prominent with the aid of proposed algorithm. It can be inferred that the proposed algorithm, besides improving the clustering accuracy, is also capable of identifying explicit object boundary for brain MRI scans.



**Fig. 5.3** Qualitative analysis among different algorithms on Test image 1 (a) original image, (b) ground truth, (c) FCM_S1, (d) FCM_S2, (e) ARKFCM, (f) EnFCM, (g) FCMLSM, (h) FGFCM_S1 , (i) FGFCM_S2, (j) FRFCM, (k) DSFCM_N, (l) AN_DsFCM (Proposed)

**Fig. 5.4** Qualitative analysis among different algorithms for Test image 2 (a) original image, (b) ground truth, (c) FCM_S1, (d) FCM_S2, (e) ARKFCM, (f) EnFCM, (g) FCMLSM, (h) FGFCM_S1 , (i) FGFCM_S2, (j) FRFCM, (k) DSFCM_N, (l) AN_DsFCM (Proposed)

**Fig. 5.5** Qualitative analysis among different algorithms for Test image 3 (a) original image, (b) ground truth, (c) FCM_S1, (d) FCM_S2, (e) ARKFCM, (f) EnFCM, (g) FCMLSM, (h) FGFCM_S1 , (i) FGFCM_S2, (j) FRFCM, (k) DSFCM_N, (l) AN_DsFCM (Proposed)

**Fig. 5.6** Qualitative analysis among different algorithms for Test image 4 (a) original image, (b) ground truth, (c) FCM_S1, (d) FCM_S2, (e) ARKFCM, (f) EnFCM, (g) FCMLSM, (h) FGFCM_S1 , (i) FGFCM_S2, (j) FRFCM, (k) DSFCM_N, (l) AN_DsFCM (Proposed)
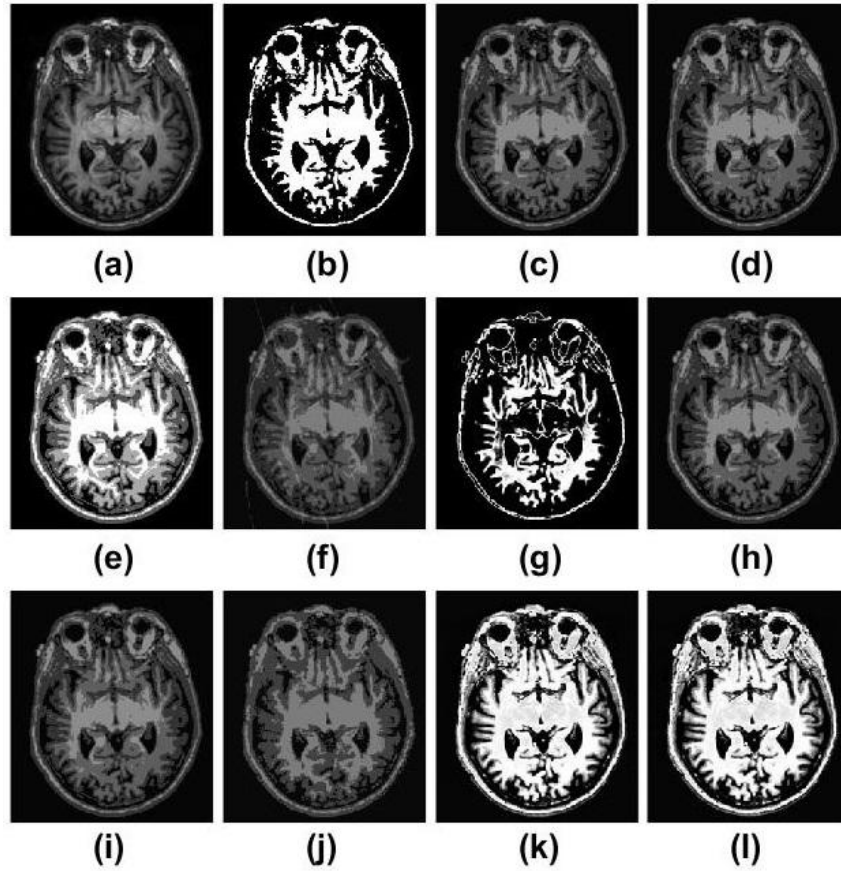
**Fig. 5.7** Qualitative analysis among different algorithms for Test image 5 (a) original image, (b) ground truth, (c) FCM_S1, (d) FCM_S2, (e) ARKFCM, (f) EnFCM, (g) FCMLSM, (h) FGFCM_S1 , (i) FGFCM_S2, (j) FRFCM, (k) DSFCM_N, (l) AN_DsFCM (Proposed)
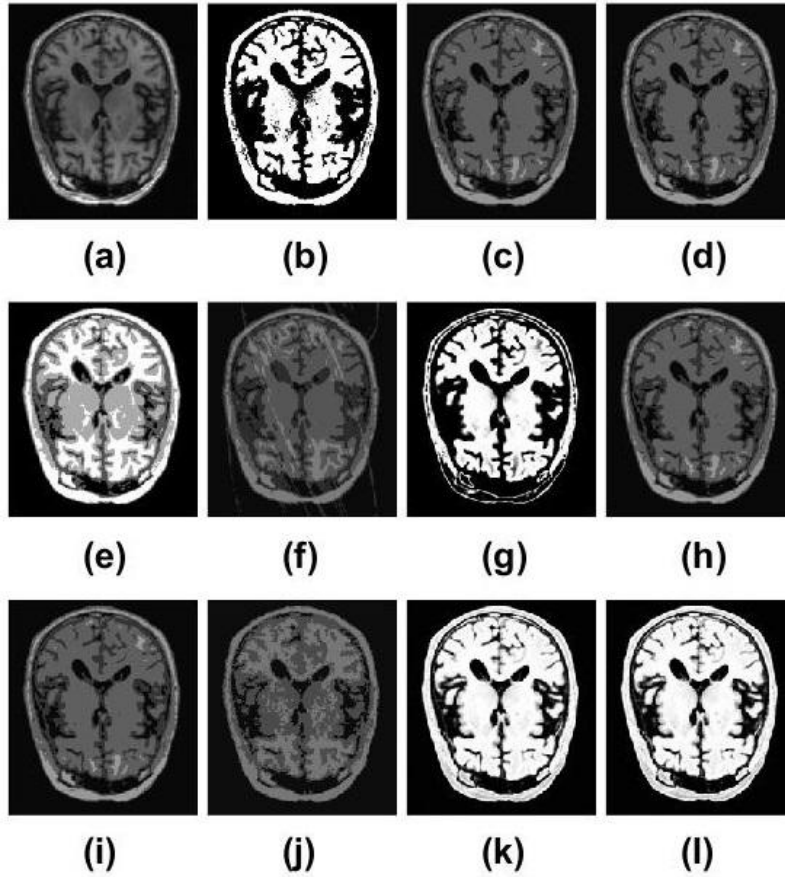
**Fig. 5.8** Qualitative analysis among different algorithms for Test image 6 (a) original image, (b) ground truth, (c) FCM_S1, (d) FCM_S2, (e) ARKFCM, (f) EnFCM, (g) FCMLSM, (h) FGFCM_S1 , (i) FGFCM_S2, (j) FRFCM, (k) DSFCM_N, (l) AN_DsFCM (Proposed)
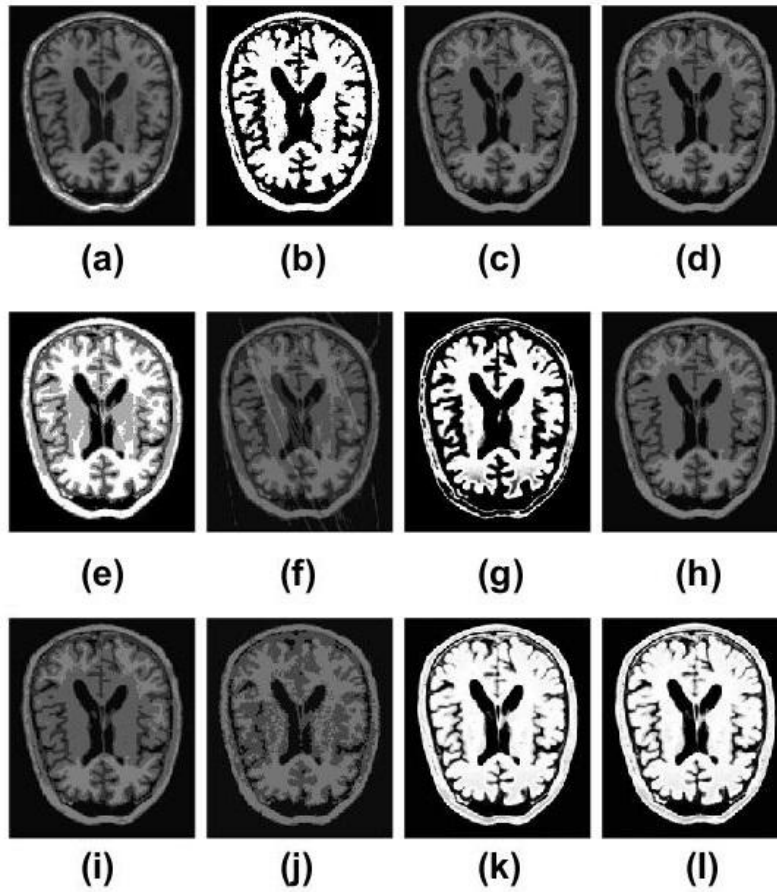
**Fig. 5.9** Qualitative analysis among different algorithms for Test image 7 (a) original image, (b) ground truth, (c) FCM_S1, (d) FCM_S2, (e) ARKFCM, (f) EnFCM, (g) FCMLSM, (h) FGFCM_S1 , (i) FGFCM_S2, (j) FRFCM, (k) DSFCM_N, (l) AN_DsFCM (Proposed)
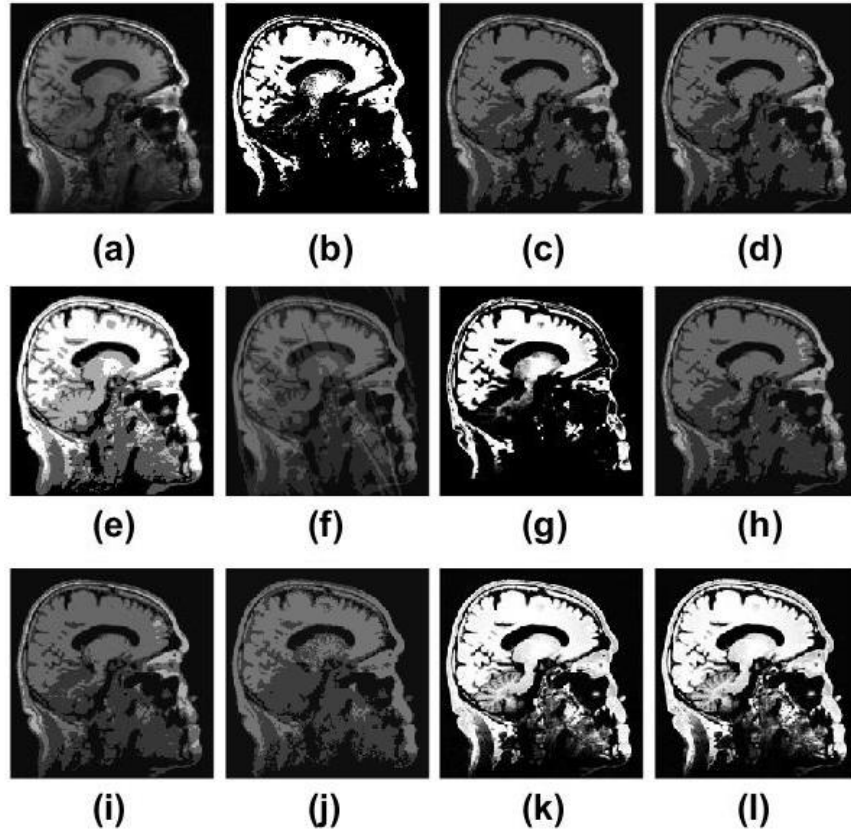
**Fig. 5.10** Qualitative analysis among different algorithms for Test image 8 (a) original image, (b) ground truth, (c) FCM_S1, (d) FCM_S2, (e) ARKFCM, (f) EnFCM, (g) FCMLSM, (h) FGFCM_S1 , (i) FGFCM_S2, (j) FRFCM, (k) DSFCM_N, (l) AN_DsFCM (Proposed)
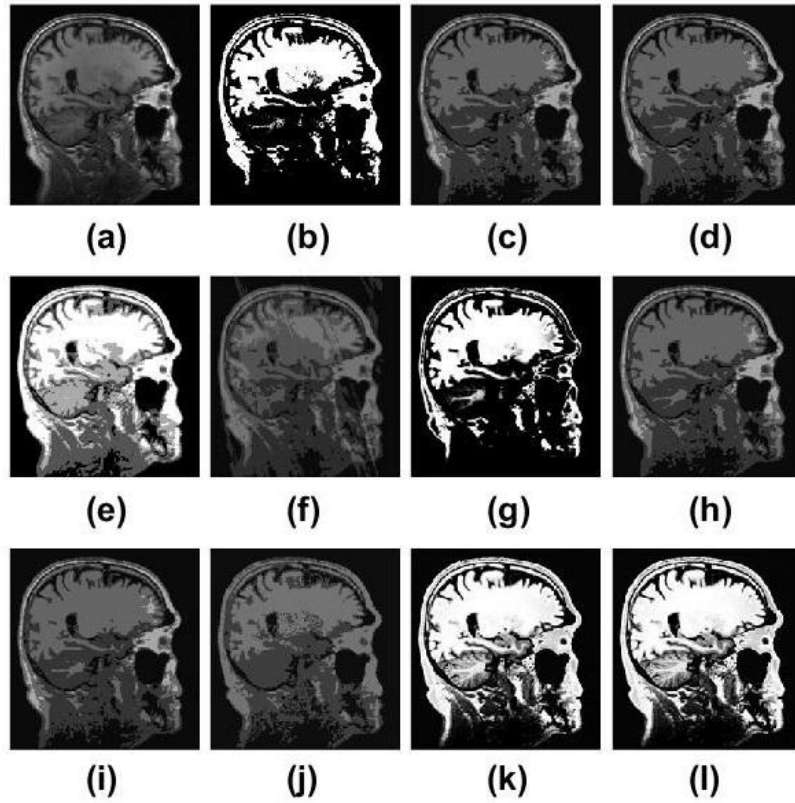
**Fig. 5.11** Qualitative analysis among different algorithms for Test image 9 (a) original image, (b) ground truth, (c) FCM_S1, (d) FCM_S2, (e) ARKFCM, (f) EnFCM, (g) FCMLSM, (h) FGFCM_S1 , (i) FGFCM_S2, (j) FRFCM, (k) DSFCM_N, (l) AN_DsFCM (Proposed)
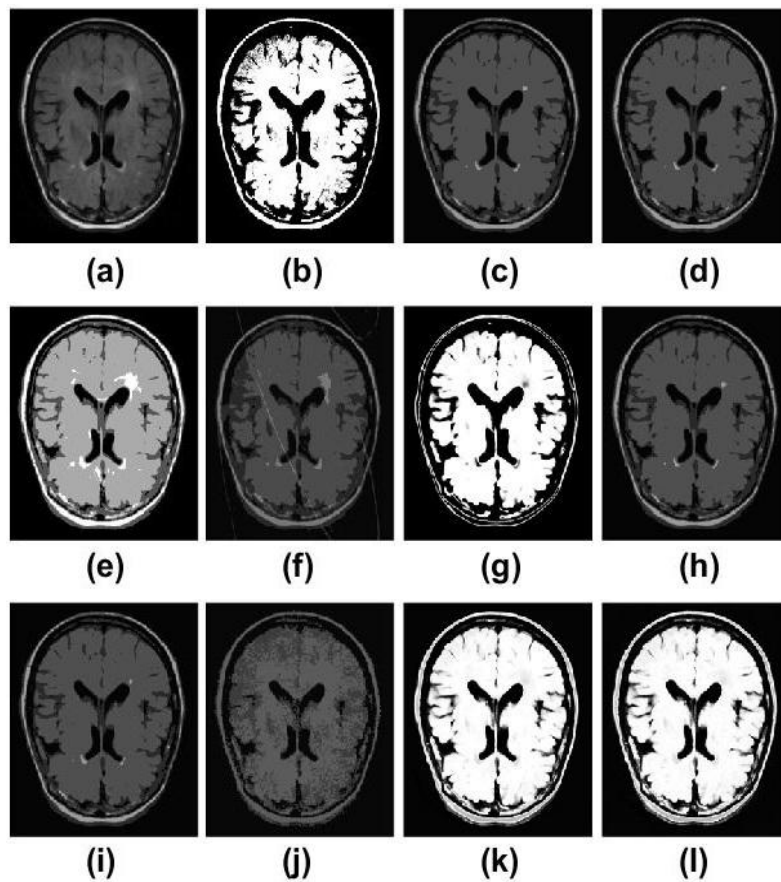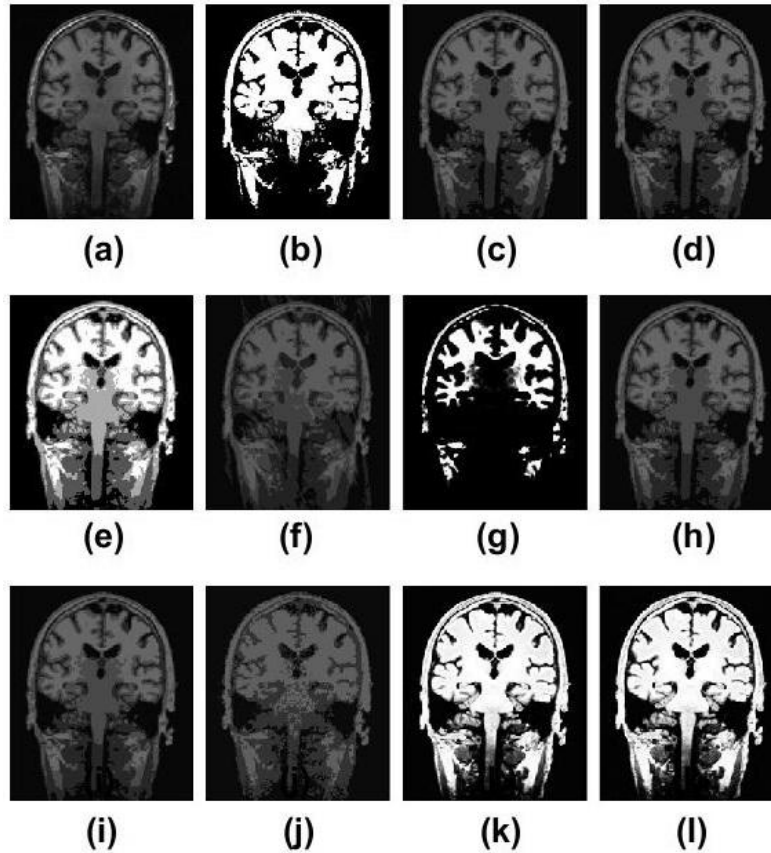
**Fig. 5.12** Qualitative analysis among different algorithms for Test image 10 (a) original image, (b) ground truth, (c) FCM_S1, (d) FCM_S2, (e) ARKFCM, (f) EnFCM, (g) FCMLSM, (h) FGFCM_S1 , (i) FGFCM_S2, (j) FRFCM, (k) DSFCM_N, (l) AN_DsFCM (Proposed)
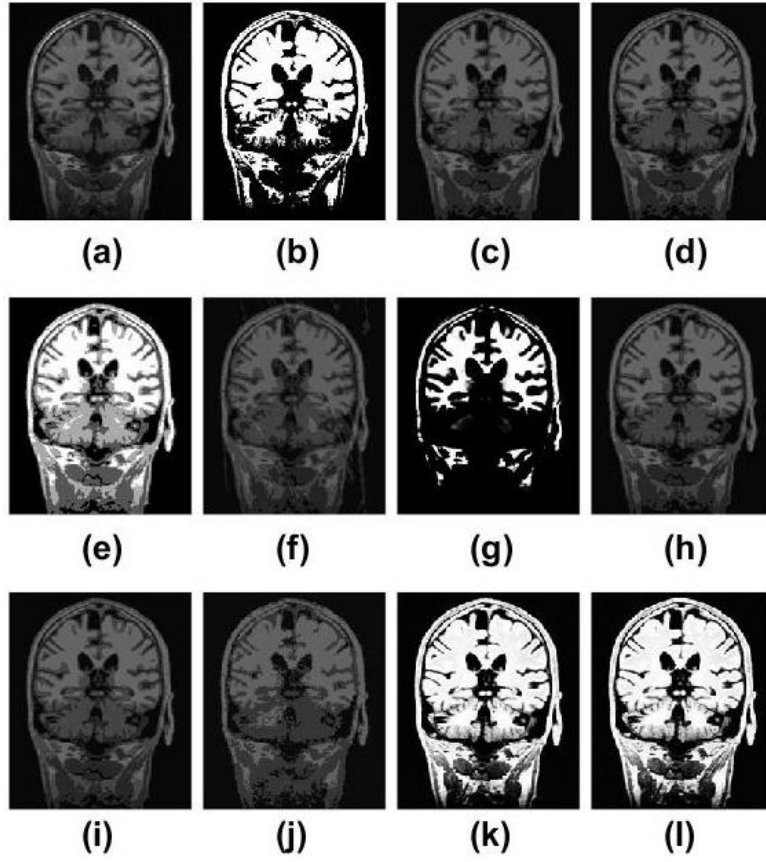
**Fig. 5.13** Qualitative analysis among different algorithms for Test image 11 (a) original image, (b) ground truth, (c) FCM_S1, (d) FCM_S2, (e) ARKFCM, (f) EnFCM, (g) FCMLSM, (h) FGFCM_S1 , (i) FGFCM_S2, (j) FRFCM, (k) DSFCM_N, (l) AN_DsFCM (Proposed)
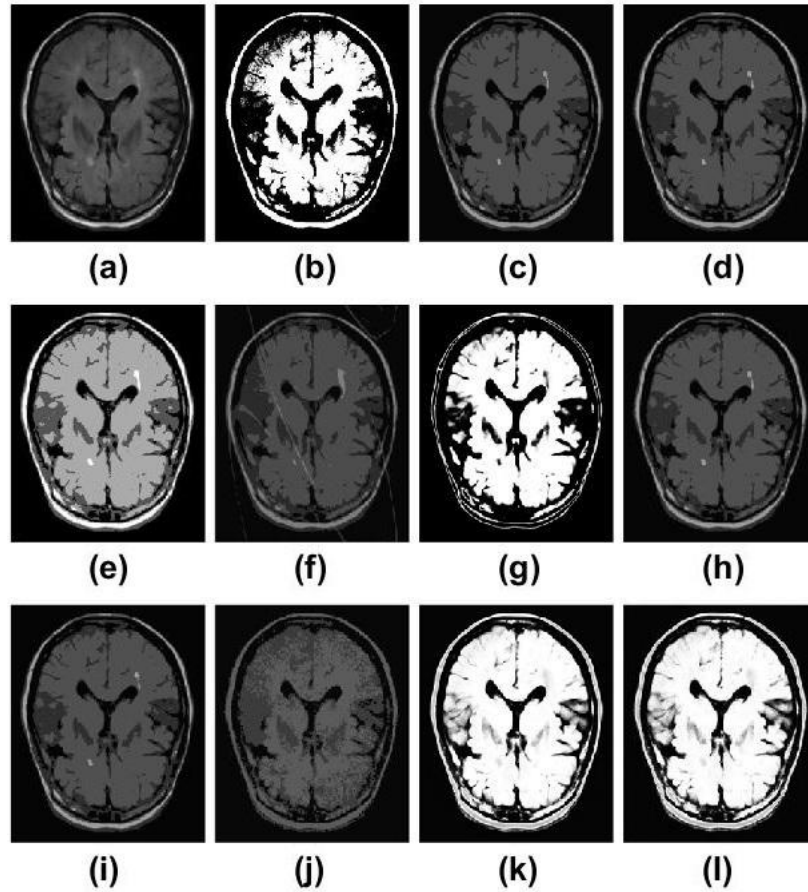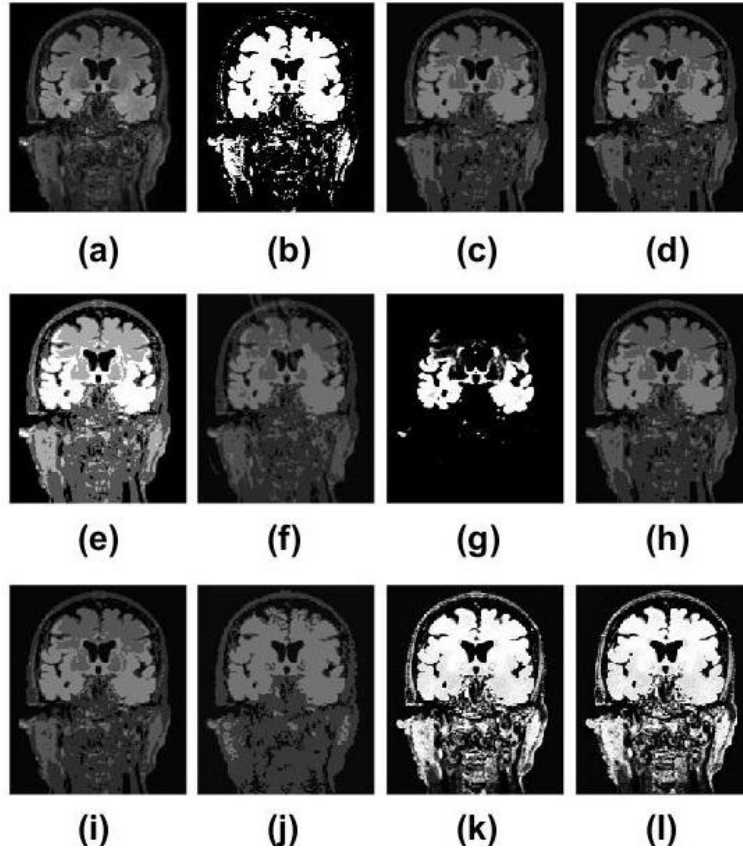
**Fig. 5.14** Qualitative analysis among different algorithms for Test image 12 (a) original image, (b) ground truth, (c) FCM_S1, (d) FCM_S2, (e) ARKFCM, (f) EnFCM, (g) FCMLSM, (h) FGFCM_S1 , (i) FGFCM_S2, (j) FRFCM, (k) DSFCM_N, (l) AN_DsFCM (Proposed)
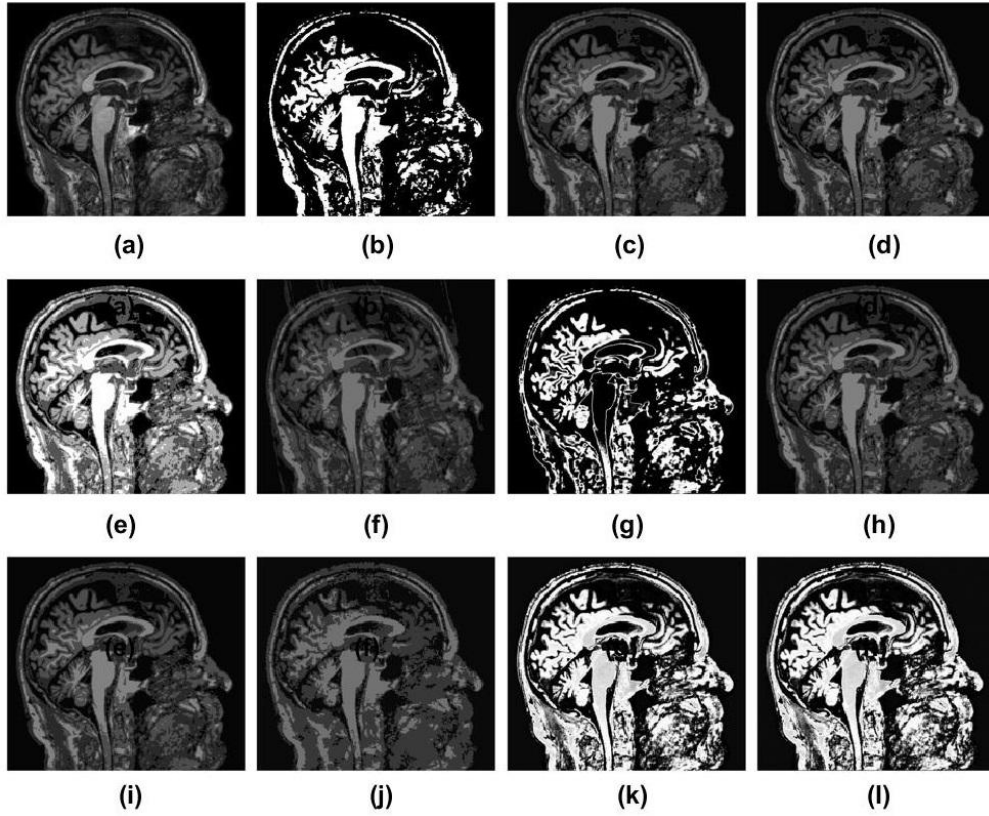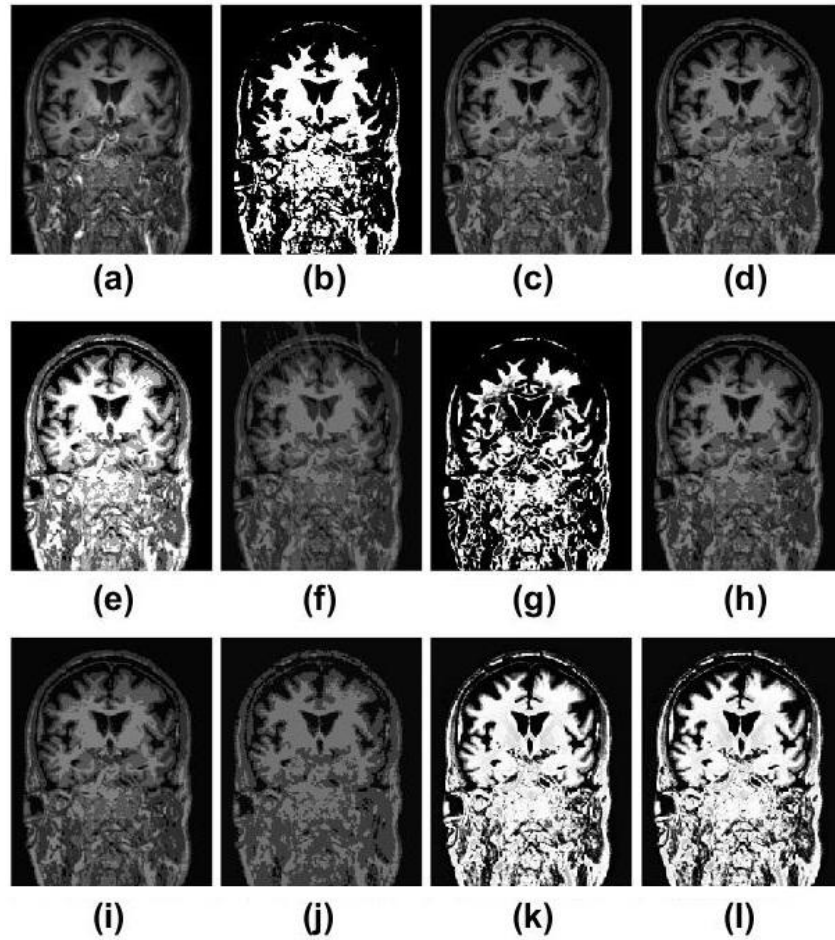
**Table 5.3** Quantitative analysis among different clustering algorithms on Test image 1

| Test image 1 | SSIM | DICE | SA | Sensitivity | JI |
|---|---|---|---|---|---|
| FCM_S1 | 0.6154 | 0.8422 | 0.8167 | 0.7274 | 0.7234 |
| FCM_S2 | 0.6165 | 0.8431 | 0.8177 | 0.7288 | 0.7233 |
| ARKFCM | 0.6539 | 0.9210 | 0.9440 | 0.9748 | 0.7259 |
| EnFCM | 0.5807 | 0.8321 | 0.8067 | 0.7125 | 0.7213 |
| FCMLSM | 0.6338 | 0.8925 | 0.8669 | 0.8896 | 0.7286 |
| FGFCM_S1 | 0.6152 | 0.8422 | 0.8167 | 0.7274 | 0.7232 |
| FGFCM_S2 | 0.6167 | 0.8431 | 0.8176 | 0.7287 | 0.7234 |
| FRFCM | 0.5757 | 0.8321 | 0.8067 | 0.7125 | 0.7232 |
| DSFCM_N | 0.6671 | 0.9590 | 0.9570 | 0.9776 | 0.7340 |
| AN_DsFCM | 0.6845 | 0.9682 | 0.9559 | 0.9893 | 0.7331 |

**Table 5.4** Quantitative analysis among different clustering algorithms on Test image 2

| Test image 2 | SSIM | DICE | SA | Sensitivity | JI |
|---|---|---|---|---|---|
| FCM_S1 | 0.5972 | 0.8565 | 0.8350 | 0.7490 | 0.7119 |
| FCM_S2 | 0.6083 | 0.8574 | 0.8359 | 0.7504 | 0.7130 |
| ARKFCM | 0.7724 | 0.9327 | 0.9168 | 0.9996 | 0.7190 |
| EnFCM | 0.5748 | 0.8451 | 0.8237 | 0.7318 | 0.7103 |
| FCMLSM | 0.6274 | 0.9386 | 0.9182 | 0.9184 | 0.9141 |
| FGFCM_S1 | 0.5973 | 0.8565 | 0.8350 | 0.7491 | 0.7117 |
| FGFCM_S2 | 0.6079 | 0.8573 | 0.8358 | 0.7503 | 0.7130 |
| FRFCM | 0.5722 | 0.8451 | 0.8237 | 0.7318 | 0.7126 |
| DSFCM_N | 0.6307 | 0.9436 | 0.9260 | 0.9193 | 0.7178 |
| AN_DsFCM | 0.6531 | 0.9534 | 0.9357 | 0.9294 | 0.7216 |

**Table 5.5** Quantitative analysis among different clustering algorithms on Test image 3

| Test image 3 | SSIM | DICE | SA | Sensitivity | JI |
|---|---|---|---|---|---|
| FCM_S1 | 0.5491 | 0.8879 | 0.8839 | 0.7984 | 0.6561 |
| FCM_S2 | 0.5504 | 0.8893 | 0.8867 | 0.7983 | 0.6562 |
| ARKFCM | 0.5699 | 0.9294 | 0.9126 | 0.9583 | 0.6672 |
| EnFCM | 0.5319 | 0.8878 | 0.8839 | 0.7983 | 0.6557 |
| FCMLSM | 0.5764 | 0.9254 | 0.9141 | 0.9246 | 0.6678 |
| FGFCM_S1 | 0.5499 | 0.8879 | 0.8839 | 0.7983 | 0.6561 |
| FGFCM_S2 | 0.5521 | 0.8879 | 0.8839 | 0.7984 | 0.6561 |
| FRFCM | 0.5327 | 0.8878 | 0.8839 | 0.7983 | 0.6557 |
| DSFCM_N | 0.5662 | 0.9361 | 0.9144 | 0.9675 | 0.6698 |
| AN_DsFCM | 0.5781 | 0.9424 | 0.9298 | 0.9874 | 0.6702 |

**Table 5.6** Quantitative analysis among different clustering algorithms on Test image 4

| Test image 4 | SSIM | DICE | SA | Sensitivity | JI |
|---|---|---|---|---|---|
| FCM_S1 | 0.5760 | 0.8675 | 0.8522 | 0.7661 | 0.6980 |
| FCM_S2 | 0.5769 | 0.8675 | 0.8522 | 0.7661 | 0.6981 |
| ARKFCM | 0.5832 | 0.8964 | 0.9124 | 0.9689 | 0.7021 |
| EnFCM | 0.5573 | 0.8675 | 0.8522 | 0.7661 | 0.6765 |
| FCMLSM | 0.5863 | 0.9168 | 0.9115 | 0.9209 | 0.6983 |
| FGFCM_S1 | 0.5764 | 0.8675 | 0.8522 | 0.7661 | 0.6982 |
| FGFCM_S2 | 0.5767 | 0.8675 | 0.8522 | 0.7661 | 0.6981 |
| FRFCM | 0.5656 | 0.8675 | 0.8522 | 0.7661 | 0.6980 |
| DSFCM_N | 0.5979 | 0.9211 | 0.9251 | 0.9725 | 0.7076 |
| AN_DsFCM | 0.6112 | 0.9494 | 0.9327 | 0.9885 | 0.7096 |

**Table 5.7** Quantitative analysis among different clustering algorithms on Test image 5

| Test image 5 | SSIM | DICE | SA | Sensitivity | JI |
|---|---|---|---|---|---|
| FCM_S1 | 0.5797 | 0.8727 | 0.8629 | 0.7742 | 0.6779 |
| FCM_S2 | 0.5803 | 0.8729 | 0.8631 | 0.7745 | 0.6681 |
| ARKFCM | 0.6192 | 0.9231 | 0.9341 | 0.9389 | 0.6747 |

| | | | | | |
|---|---|---|---|---|---|
| EnFCM | 0.6135 | 0.8721 | 0.8623 | 0.7731 | 0.6654 |
| FCMLSM | 0.8672 | 0.9250 | 0.9372 | 0.9225 | 0.6716 |
| FGFCM_S1 | 0.5792 | 0.8726 | 0.8628 | 0.7740 | 0.6679 |
| FGFCM_S2 | 0.5804 | 0.8729 | 0.8631 | 0.7745 | 0.6683 |
| FRFCM | 0.5565 | 0.8721 | 0.8623 | 0.7732 | 0.6676 |
| DSFCM_N | 0.6289 | 0.9446 | 0.9454 | 0.9586 | 0.6781 |
| AN_DsFCM | 0.6330 | 0.9624 | 0.9527 | 0.9884 | 0.6804 |

**Table 5.8** Quantitative analysis among different clustering algorithms on Test image 6

| Test image 6 | SSIM | DICE | SA | Sensitivity | JI |
|---|---|---|---|---|---|
| FCM_S1 | 0.6637 | 0.8924 | 0.8599 | 0.8057 | 0.7722 |
| FCM_S2 | 0.6646 | 0.8982 | 0.8668 | 0.8153 | 0.7722 |
| ARKFCM | 0.7490 | 0.9471 | 0.9162 | 0.9433 | 0.7812 |
| EnFCM | 0.6437 | 0.8870 | 0.8536 | 0.7970 | 0.7720 |
| FCMLSM | 0.8886 | 0.9791 | 0.9412 | 0.9546 | 0.7789 |
| FGFCM_S1 | 0.6626 | 0.8916 | 0.8589 | 0.8043 | 0.7721 |
| FGFCM_S2 | 0.6639 | 0.8989 | 0.8676 | 0.8164 | 0.7722 |
| FRFCM | 0.6430 | 0.8870 | 0.8536 | 0.7970 | 0.7723 |
| DSFCM_N | 0.7666 | 0.9530 | 0.9419 | 0.9698 | 0.7810 |
| AN_DsFCM | 0.7746 | 0.9722 | 0.9589 | 0.9890 | 0.7826 |

**Table 5.9** Quantitative analysis among different clustering algorithms on Test image 7

| Test image 7 | SSIM | DICE | SA | Sensitivity | JI |
|---|---|---|---|---|---|
| FCM_S1 | 0.6822 | 0.8810 | 0.8414 | 0.7872 | 0.7976 |
| FCM_S2 | 0.6828 | 0.8810 | 0.8414 | 0.7872 | 0.7976 |
| ARKFCM | 0.7759 | 0.9857 | 0.9384 | 0.8929 | 0.8009 |
| EnFCM | 0.6649 | 0.8810 | 0.8414 | 0.7872 | 0.7975 |
| FCMLSM | 0.7613 | 0.9430 | 0.9750 | 0.9488 | 0.7930 |
| FGFCM_S1 | 0.6819 | 0.8810 | 0.8414 | 0.7872 | 0.7977 |
| FGFCM_S2 | 0.6834 | 0.8810 | 0.8414 | 0.7872 | 0.7977 |
| FRFCM | 0.6652 | 0.8810 | 0.8414 | 0.7872 | 0.7976 |
| DSFCM_N | 0.7963 | 0.9682 | 0.9567 | 0.9385 | 0.8034 |
| AN_DsFCM | 0.8014 | 0.9770 | 0.9650 | 0.9889 | 0.8112 |

**Table 5.10** Quantitative analysis among different clustering algorithms on Test image 8

| Test image 8 | SSIM | DICE | SA | Sensitivity | JI |
|---|---|---|---|---|---|
| FCM_S1 | 0.6145 | 0.9152 | 0.8993 | 0.8371 | 0.6971 |
| FCM_S2 | 0.6169 | 0.9146 | 0.8987 | 0.8427 | 0.6971 |
| ARKFCM | 0.6597 | 0.9577 | 0.9230 | 0.9699 | 0.7072 |
| EnFCM | 0.5972 | 0.9009 | 0.8838 | 0.8197 | 0.6970 |
| FCMLSM | 0.9084 | 0.9819 | 0.9769 | 0.9755 | 0.9351 |
| FGFCM_S1 | 0.6144 | 0.9152 | 0.8993 | 0.8437 | 0.6971 |
| FGFCM_S2 | 0.6171 | 0.9146 | 0.8987 | 0.8427 | 0.6971 |
| FRFCM | 0.6063 | 0.9009 | 0.8838 | 0.8197 | 0.6974 |
| DSFCM_N | 0.6670 | 0.9616 | 0.9313 | 0.9793 | 0.7154 |
| AN_DsFCM | 0.6890 | 0.9618 | 0.9489 | 0.9883 | 0.7200 |

**Table 5.11** Quantitative analysis among different clustering algorithms on Test image 9

| Test image 9 | SSIM | DICE | SA | Sensitivity | JI |
|---|---|---|---|---|---|
| FCM_S1 | 0.6264 | 0.9131 | 0.8944 | 0.8400 | 0.7117 |
| FCM_S2 | 0.6274 | 0.9128 | 0.8942 | 0.8396 | 0.7118 |
| ARKFCM | 0.6428 | 0.9498 | 0.9302 | 0.9699 | 0.7190 |
| EnFCM | 0.6041 | 0.8976 | 0.8774 | 0.8142 | 0.7117 |
| FCMLSM | 0.6499 | 0.9597 | 0.9234 | 0.9753 | 0.7211 |
| FGFCM_S1 | 0.6255 | 0.9131 | 0.8945 | 0.8401 | 0.7117 |
| FGFCM_S2 | 0.6276 | 0.9128 | 0.8941 | 0.8395 | 0.7118 |
| FRFCM | 0.6198 | 0.8976 | 0.8774 | 0.8142 | 0.7120 |
| DSFCM_N | 0.6598 | 0.9536 | 0.9391 | 0.9728 | 0.7228 |
| AN_DsFCM | 0.6839 | 0.9618 | 0.9476 | 0.9885 | 0.7271 |

**Table 5.12** Quantitative analysis among different clustering algorithms on Test image 10

| Test image 10 | SSIM | DICE | SA | Sensitivity | JI |
|---|---|---|---|---|---|
| FCM_S1 | 0.6459 | 0.8868 | 0.8581 | 0.7966 | 0.7440 |
| FCM_S2 | 0.6464 | 0.8868 | 0.8581 | 0.7966 | 0.7439 |
| ARKFCM | 0.7390 | 0.9677 | 0.9526 | 0.9499 | 0.7516 |
| EnFCM | 0.6302 | 0.8868 | 0.8581 | 0.7966 | 0.7439 |
| FCMLSM | 0.7254 | 0.8696 | 0.8893 | 0.9143 | 0.7405 |
| FGFCM_S1 | 0.6452 | 0.8868 | 0.8581 | 0.7966 | 0.7440 |
| FGFCM_S2 | 0.6468 | 0.8868 | 0.8581 | 0.7966 | 0.7440 |
| FRFCM | 0.6315 | 0.8868 | 0.8581 | 0.7966 | 0.7444 |
| DSFCM_N | 0.7392 | 0.9696 | 0.9653 | 0.9598 | 0.7570 |
| AN_DsFCM | 0.7506 | 0.9793 | 0.9706 | 0.9872 | 0.7566 |

**Table 5.13** Quantitative analysis among different clustering algorithms on Test image 11

| Test image 11 | SSIM | DICE | SA | Sensitivity | JI |
|---|---|---|---|---|---|
| FCM_S1 | 0.6447 | 0.8896 | 0.8614 | 0.8012 | 0.7534 |
| FCM_S2 | 0.6459 | 0.8896 | 0.8614 | 0.8012 | 0.7535 |
| ARKFCM | 0.6930 | 0.9471 | 0.9373 | 0.9299 | 0.7599 |
| EnFCM | 0.6310 | 0.8896 | 0.8614 | 0.8012 | 0.7533 |
| FCMLSM | 0.6989 | 0.9500 | 0.9336 | 0.9048 | 0.9196 |
| FGFCM_S1 | 0.6449 | 0.8896 | 0.8614 | 0.8012 | 0.7533 |
| FGFCM_S2 | 0.6456 | 0.8896 | 0.8614 | 0.8012 | 0.7535 |
| FRFCM | 0.6326 | 0.8896 | 0.8614 | 0.8012 | 0.7539 |
| DSFCM_N | 0.7144 | 0.9756 | 0.9651 | 0.9486 | 0.7616 |
| AN_DsFCM | 0.7367 | 0.9728 | 0.9611 | 0.9872 | 0.7646 |

**Table 5.14** Quantitative analysis among different clustering algorithms on Test image 12

| Test image 12 | SSIM | DICE | SA | Sensitivity | JI |
|---|---|---|---|---|---|
| FCM_S1 | 0.6801 | 0.9177 | 0.8948 | 0.8480 | 0.7549 |
| FCM_S2 | 0.6823 | 0.9177 | 0.8948 | 0.8480 | 0.7547 |
| ARKFCM | 0.6948 | 0.9425 | 0.9396 | 0.9282 | 0.7596 |
| EnFCM | 0.6602 | 0.9177 | 0.8948 | 0.8480 | 0.7537 |
| FCMLSM | 0.7953 | 0.9489 | 0.9327 | 0.9027 | 0.7465 |
| FGFCM_S1 | 0.6796 | 0.9177 | 0.8948 | 0.8480 | 0.7547 |
| FGFCM_S2 | 0.6823 | 0.9177 | 0.8948 | 0.8480 | 0.7547 |
| FRFCM | 0.6631 | 0.9177 | 0.8948 | 0.8480 | 0.7543 |
| DSFCM_N | 0.7011 | 0.9522 | 0.9448 | 0.9596 | 0.7458 |
| AN_DsFCM | 0.7120 | 0.9766 | 0.9670 | 0.9851 | 0.7651 |

**Table 5.15** Quantitative analysis among different clustering algorithms on Real image 1

| Real image 1 | SSIM | DICE | SA | Sensitivity | JI |
|---|---|---|---|---|---|
| FCM_S1 | 0.6689 | 0.8578 | 0.8145 | 0.7510 | 0.7852 |
| FCM_S2 | 0.6692 | 0.8578 | 0.8145 | 0.7510 | 0.7852 |
| ARKFCM | 0.8184 | 0.8939 | 0.9309 | 0.9590 | 0.7787 |
| EnFCM | 0.6543 | 0.8578 | 0.8145 | 0.7510 | 0.7852 |
| FCMLSM | 0.7995 | 0.9374 | 0.9122 | 0.8821 | 0.7806 |
| FGFCM_S1 | 0.6691 | 0.8578 | 0.8145 | 0.7510 | 0.7852 |
| FGFCM_S2 | 0.6692 | 0.8578 | 0.8145 | 0.7510 | 0.7852 |
| FRFCM | 0.6518 | 0.8578 | 0.8145 | 0.7510 | 0.7852 |
| DSFCM_N | 0.8345 | 0.9634 | 0.9649 | 0.9789 | 0.7869 |
| AN_DsFCM | 0.8580 | 0.9825 | 0.9734 | 0.9890 | 0.8013 |

**Table 5.16** Quantitative analysis among different clustering algorithms on Real image 2

| Real image 2 | SSIM | DICE | SA | Sensitivity | JI |
|---|---|---|---|---|---|
| FCM_S1 | 0.6445 | 0.8483 | 0.8055 | 0.7365 | 0.7794 |
| FCM_S2 | 0.6447 | 0.8483 | 0.8055 | 0.7365 | 0.7794 |
| ARKFCM | 0.8146 | 0.9482 | 0.9224 | 0.9579 | 0.7758 |
| EnFCM | 0.6326 | 0.8483 | 0.8055 | 0.7365 | 0.7794 |
| FCMLSM | 0.7714 | 0.9207 | 0.8916 | 0.8531 | 0.7641 |
| FGFCM_S1 | 0.6444 | 0.8483 | 0.8055 | 0.7365 | 0.7794 |
| FGFCM_S2 | 0.6456 | 0.8483 | 0.8055 | 0.7365 | 0.7794 |
| FRFCM | 0.6242 | 0.8483 | 0.8055 | 0.7365 | 0.7795 |
| DSFCM_N | 0.8250 | 0.9689 | 0.9481 | 0.9742 | 0.7841 |
| AN_DsFCM | 0.8318 | 0.9783 | 0.9672 | 0.9832 | 0.7942 |

**Table 5.17** Quantitative analysis among different clustering algorithms on Real image 3

| Real image 3 | SSIM | DICE | SA | Sensitivity | JI |
|---|---|---|---|---|---|
| FCM_S1 | 0.6519 | 0.8380 | 0.7926 | 0.7212 | 0.7830 |
| FCM_S2 | 0.6522 | 0.8380 | 0.7926 | 0.7212 | 0.7831 |
| ARKFCM | 0.8122 | 0.9349 | 0.9123 | 0.9464 | 0.7849 |

| | | | | | |
|---|---|---|---|---|---|
| EnFCM | 0.6355 | 0.8380 | 0.7926 | 0.7212 | 0.7831 |
| FCMLSM | 0.7680 | 0.9101 | 0.8773 | 0.8350 | 0.7882 |
| FGFCM_S1 | 0.7516 | 0.8330 | 0.7926 | 0.7212 | 0.7830 |
| FGFCM_S2 | 0.6522 | 0.8380 | 0.7926 | 0.7212 | 0.7830 |
| FRFCM | 0.6258 | 0.8380 | 0.7926 | 0.7212 | 0.7831 |
| DSFCM_N | 0.8285 | 0.9732 | 0.9546 | 0.9887 | 0.7815 |
| AN_DsFCM | 0.8531 | 0.9824 | 0.9735 | 0.9974 | 0.7962 |

**Table 5.18** Quantitative analysis among different clustering algorithms on Real image 4

| Real image 4 | SSIM | DICE | SA | Sensitivity | JI |
|---|---|---|---|---|---|
| FCM_S1 | 0.6543 | 0.8361 | 0.7901 | 0.7184 | 0.7815 |
| FCM_S2 | 0.6545 | 0.8361 | 0.7901 | 0.7184 | 0.7815 |
| ARKFCM | 0.8225 | 0.9561 | 0.9342 | 0.9484 | 0.7968 |
| EnFCM | 0.6382 | 0.8361 | 0.7901 | 0.7184 | 0.7814 |
| FCMLSM | 0.7419 | 0.8685 | 0.8268 | 0.7676 | 0.7989 |
| FGFCM_S1 | 0.6541 | 0.8361 | 0.7901 | 0.7184 | 0.7815 |
| FGFCM_S2 | 0.6547 | 0.8361 | 0.7901 | 0.7184 | 0.7814 |
| FRFCM | 0.6270 | 0.8361 | 0.7901 | 0.7184 | 0.7815 |
| DSFCM_N | 0.8549 | 0.9666 | 0.9698 | 0.9712 | 0.7938 |
| AN_DsFCM | 0.8641 | 0.9855 | 0.9781 | 0.9887 | 0.8012 |

**Table 5.19** Quantitative analysis among different clustering algorithms on Real image 5

| Real image 5 | SSIM | DICE | SA | Sensitivity | JI |
|---|---|---|---|---|---|
| FCM_S1 | 0.6471 | 0.8481 | 0.8072 | 0.7362 | 0.7747 |
| FCM_S2 | 0.6495 | 0.8483 | 0.8072 | 0.7362 | 0.7748 |
| ARKFCM | 0.8175 | 0.9345 | 0.9320 | 0.9676 | 0.7818 |
| EnFCM | 0.6302 | 0.8481 | 0.8072 | 0.7362 | 0.7747 |
| FCMLSM | 0.7546 | 0.8723 | 0.8514 | 0.8846 | 0.7749 |
| FGFCM_S1 | 0.6472 | 0.8481 | 0.8072 | 0.7362 | 0.7747 |
| FGFCM_S2 | 0.6491 | 0.8481 | 0.8072 | 0.7362 | 0.7747 |
| FRFCM | 0.6273 | 0.8481 | 0.8072 | 0.7362 | 0.7748 |
| DSFCM_N | 0.8392 | 0.9733 | 0.9586 | 0.9864 | 0.7838 |
| AN_DsFCM | 0.8441 | 0.9811 | 0.9719 | 0.9987 | 0.7889 |

**Table 5.20** Quantitative analysis among different clustering algorithms on Real image 6

| Real image 6 | SSIM | DICE | SA | Sensitivity | JI |
|---|---|---|---|---|---|
| FCM_S1 | 0.6338 | 0.8458 | 0.8061 | 0.7328 | 0.7685 |
| FCM_S2 | 0.6338 | 0.8458 | 0.8061 | 0.7328 | 0.7685 |
| ARKFCM | 0.7533 | 0.9325 | 0.9191 | 0.9683 | 0.7716 |
| EnFCM | 0.6186 | 0.8458 | 0.8061 | 0.7328 | 0.7685 |
| FCMLSM | 0.6384 | 0.8626 | 0.8314 | 0.7849 | 0.7652 |
| FGFCM_S1 | 0.6338 | 0.8458 | 0.8061 | 0.7328 | 0.7686 |
| FGFCM_S2 | 0.6339 | 0.8458 | 0.8061 | 0.7328 | 0.7686 |
| FRFCM | 0.6139 | 0.8458 | 0.8061 | 0.7328 | 0.7686 |
| DSFCM_N | 0.7785 | 0.9560 | 0.9381 | 0.9879 | 0.7741 |
| AN_DsFCM | 0.7825 | 0.9680 | 0.9521 | 0.9998 | 0.7813 |

**Table 5.21** Quantitative analysis among different clustering algorithms on Real image 7

| Real image 7 | SSIM | DICE | SA | Sensitivity | JI |
|---|---|---|---|---|---|
| FCM_S1 | 0.6715 | 0.8624 | 0.8200 | 0.7581 | 0.7878 |
| FCM_S2 | 0.6720 | 0.8624 | 0.8200 | 0.7581 | 0.7877 |
| ARKFCM | 0.8316 | 0.9646 | 0.9320 | 0.9289 | 0.7893 |
| EnFCM | 0.6566 | 0.8624 | 0.8200 | 0.7581 | 0.7877 |
| FCMLSM | 0.7929 | 0.9383 | 0.9135 | 0.8838 | 0.7914 |
| FGFCM_S1 | 0.6713 | 0.8624 | 0.8200 | 0.7581 | 0.7877 |
| FGFCM_S2 | 0.6720 | 0.8624 | 0.8200 | 0.7581 | 0.7878 |
| FRFCM | 0.6548 | 0.8624 | 0.8200 | 0.7581 | 0.7878 |
| DSFCM_N | 0.8522 | 0.9737 | 0.9593 | 0.9812 | 0.7930 |
| AN_DsFCM | 0.8537 | 0.9828 | 0.9740 | 0.9870 | 0.7976 |

**Table 5.22** Quantitative analysis among different clustering algorithms on Real image 8

| Real image 8 | SSIM | DICE | SA | Sensitivity | JI |
|---|---|---|---|---|---|
| FCM_S1 | 0.6936 | 0.8727 | 0.8298 | 0.7741 | 0.7850 |
| FCM_S2 | 0.6938 | 0.8727 | 0.8298 | 0.7741 | 0.7850 |
| ARKFCM | 0.8225 | 0.9447 | 0.9328 | 0.9507 | 0.7958 |
| EnFCM | 0.6713 | 0.8727 | 0.8298 | 0.7741 | 0.7849 |
| FCMLSM | 0.8038 | 0.9394 | 0.9140 | 0.8858 | 0.7825 |
| FGFCM_S1 | 0.6939 | 0.8727 | 0.8298 | 0.7741 | 0.7850 |
| FGFCM_S2 | 0.6929 | 0.8727 | 0.8298 | 0.7741 | 0.7850 |
| FRFCM | 0.6746 | 0.8727 | 0.8298 | 0.7741 | 0.7850 |
| DSFCM_N | 0.8714 | 0.9753 | 0.9655 | 0.9816 | 0.8265 |
| AN_DsFCM | 0.8772 | 0.9847 | 0.9766 | 0.9872 | 0.8323 |

**Table 5.23** Comparative analysis on ADNI Test images in terms of FOM

| | TI 1 | TI 2 | TI 3 | TI 4 | TI 5 | TI 6 | TI 7 | TI 8 | TI 9 | TI 10 | TI 11 | TI 12 |
|---|---|---|---|---|---|---|---|---|---|---|---|---|
| FCM_S1 | 0.7492 | 0.7700 | 0.9237 | 0.8995 | 0.9032 | 0.8648 | 0.8926 | 0.8701 | 0.8677 | 0.7971 | 0.8016 | 0.9175 |
| FCM_S2 | 0.7488 | 0.7696 | 0.9245 | 0.8987 | 0.9040 | 0.8603 | 0.8911 | 0.8678 | 0.8618 | 0.7959 | 0.8006 | 0.9185 |
| ARKFCM | 0.8928 | 0.8666 | 0.9037 | 0.9065 | 0.9191 | 0.9152 | 0.9119 | 0.9038 | 0.9043 | 0.9258 | 0.9251 | 0.9380 |
| EnFCM | 0.7491 | 0.7751 | 0.8429 | 0.7926 | 0.8837 | 0.8816 | 0.7972 | 0.8202 | 0.8320 | 0.7953 | 0.8016 | 0.8523 |
| FCMLSM | 0.9163 | 0.8741 | 0.9181 | 0.9101 | 0.9348 | 0.9305 | 0.9338 | 0.8928 | 0.8925 | 0.8376 | 0.9177 | 0.9262 |
| FGFCM_S1 | 0.7489 | 0.7700 | 0.9215 | 0.9000 | 0.9020 | 0.8659 | 0.8926 | 0.8697 | 0.8677 | 0.7871 | 0.8016 | 0.9189 |
| FGFCM_S2 | 0.7488 | 0.7695 | 0.9259 | 0.9029 | 0.9050 | 0.8592 | 0.8900 | 0.8675 | 0.8767 | 0.7961 | 0.8016 | 0.9189 |
| FRFCM | 0.7846 | 0.7539 | 0.8542 | 0.8290 | 0.9263 | 0.8980 | 0.8688 | 0.8930 | 0.8760 | 0.7982 | 0.8123 | 0.8912 |
| DSFCM_N | 0.9187 | 0.8801 | 0.9318 | 0.9086 | 0.9265 | 0.9263 | 0.9258 | 0.9167 | 0.9147 | 0.9331 | 0.9393 | 0.9499 |
| AN_DsFCM | 0.9384 | 0.9106 | 0.9535 | 0.9304 | 0.9554 | 0.9465 | 0.9556 | 0.9261 | 0.9253 | 0.9621 | 0.9490 | 0.9581 |

**Table 5.24** Comparative analysis on Real images in terms of FOM

|  | RI 1 | RI 2 | RI 3 | RI 4 | RI 5 | RI 6 | RI 7 | RI 8 |
|---|---|---|---|---|---|---|---|---|
| FCM_S1 | 0.7515 | 0.7373 | 0.7234 | 0.7457 | 0.7563 | 0.8225 | 0.7634 | 0.9476 |
| FCM_S2 | 0.7515 | 0.7370 | 0.7234 | 0.7461 | 0.7593 | 0.8298 | 0.7626 | 0.9477 |
| ARKFCM | 0.9398 | 0.9168 | 0.8950 | 0.9154 | 0.8819 | 0.8682 | 0.9117 | 0.9288 |
| EnFCM | 0.7515 | 0.7370 | 0.7234 | 0.7185 | 0.7363 | 0.7578 | 0.7583 | 0.9176 |
| FCMLSM | 0.9146 | 0.9099 | 0.8925 | 0.8094 | 0.8327 | 0.8861 | 0.9206 | 0.9498 |
| FGFCM_S1 | 0.7515 | 0.7370 | 0.7238 | 0.7354 | 0.7565 | 0.8247 | 0.7608 | 0.9487 |
| FGFCM_S2 | 0.7515 | 0.7370 | 0.7234 | 0.7413 | 0.7725 | 0.8307 | 0.7633 | 0.9476 |
| FRFCM | 0.7543 | 0.7453 | 0.7253 | 0.7315 | 0.7394 | 0.7681 | 0.7782 | 0.9446 |
| DSFCM_N | 0.9520 | 0.9387 | 0.9384 | 0.9523 | 0.9495 | 0.9137 | 0.9587 | 0.9578 |
| AN_DsFCM | 0.9660 | 0.9580 | 0.9676 | 0.9721 | 0.9632 | 0.9361 | 0.9663 | 0.9721 |

**Table 5.25** Time complexity (sec) of different clustering algorithms

|  | TI 1 | TI 2 | TI 3 | TI 4 | TI 5 | TI 6 | TI 7 | TI 8 | TI 9 | TI 10 | TI 11 | TI 12 |
|---|---|---|---|---|---|---|---|---|---|---|---|---|
| FCM_S1 | 2.68 | 3.32 | 3.29 | 3.81 | 4.12 | 2.01 | 1.83 | 2.64 | 2.15 | 1.45 | 1.90 | 1.57 |
| FCM_S2 | 3.04 | 3.26 | 3.26 | 4.00 | 4.02 | 2.05 | 1.90 | 2.69 | 2.11 | 1.35 | 1.77 | 1.56 |
| ARKFCM | 14.24 | 13.62 | 15.23 | 13.79 | 13.81 | 12.42 | 7.342 | 10.62 | 9.10 | 7.288 | 7.35 | 6.18 |
| EnFCM | 2.410 | 2.255 | 1.380 | 1.14 | 2.267 | 1.969 | 1.418 | 2.711 | 1.416 | 2.555 | 1.47 | 2.47 |
| FCMLSM | 7.601 | 8.829 | 10.54 | 12.18 | 10.32 | 8.841 | 8.640 | 10.257 | 6.718 | 4.650 | 6.23 | 7.17 |
| FGFCM_S1 | 2.686 | 2.638 | 2.635 | 1.82 | 2.751 | 5.915 | 1.695 | 3.463 | 1.881 | 1.806 | 1.77 | 1.75 |
| FGFCM_S2 | 1.392 | 3.228 | 1.434 | 1.612 | 1.521 | 1.205 | 1.159 | 1.972 | 1.303 | 1.358 | 0.97 | 0.83 |
| FRFCM | 2.926 | 2.473 | 2.510 | 2.52 | 2.413 | 1.486 | 1.542 | 1.575 | 1.576 | 3.314 | 1.48 | 1.50 |
| DSFCM_N | 3.747 | 3.686 | 4.323 | 4.12 | 4.241 | 1.533 | 1.541 | 1.846 | 1.873 | 1.744 | 1.59 | 2.92 |
| AN_DsFCM | 2.580 | 3.070 | 3.562 | 3.45 | 3.312 | 1.574 | 1.492 | 1.833 | 1.741 | 1.650 | 1.72 | 1.74 |

Qualitative and quantitative analysis among different state-of-the-art clustering techniques have been presented in this section. Looking at the entries of these tables, it can be inferred that the SSIM score is maximum for AN_DsFCM as compared to other methods. A dynamic content of spatial information makes the AN_DsFCM more effective to obtain promising score in terms of SSIM. The DICE coefficient value is obtained between 0.94 and 0.97 for AN_DsFCM which is the best among all other clustering methods. The higher value of DICE coefficient indicates that

proposed model performs better to segregate white matter regional information which is disturbed by intensity in homogeneity.

It is also seen that proposed AN_DsFCM attains higher value of segmentation accuracy as compared to other existing clustering methods. The accuracy value is within 0.92 and 0.96 for all the test images under consideration. Higher value of SA indicates that AN_DsFCM is capable to provide improved clustering accuracy by suppressing rician noise interventions. While considering the improved values of sensitivity and JI, it has been observed that proposed algorithm is capable to minimize the possibility of missed detection (false negative) and provides regional segmentation accuracy to a significant extent. An impressive response has also been found in terms of FOM which varies from 0.91 to 0.96. Enhanced FOM score indicates that edge detection efficiency is uplifted for AN_DsFCM. A similar improved simulated quantitative response is also found for patient MRI practical data which proves the robustness of the proposed clustering algorithm.

Entropy plots for all the twelve test images are shown in Fig. 5.15 to 5.26. From these plots, it can be clearly inferred that the gross entropy response of AN_DsFCM is greater than all other ten FCM based clustering methods. It indicates more information content about weak regional object boundary constraints at proposed clustering output. The dynamic neighbor information constraint module has provided the potential to classify selective object boundary pixels. The entropy plot dedicatedly emphasizes only on the information content of projected response while other quantitative parameters run through a comparison process with ground truth by different means. It has also been pointed out that entropy plot response of practical patient MRI data is quite similar to ADNI test MRI entropy response. Overall entropy response of the proposed algorithm expresses a justified clustering output which indicates to contain improved clustering boundary constraints based on dynamic neighbor information.
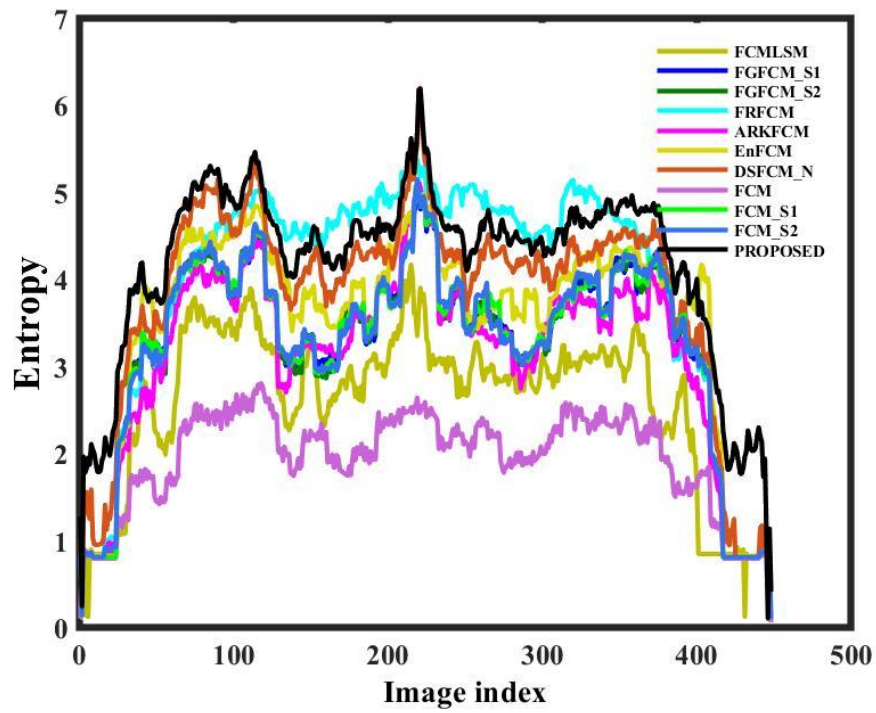
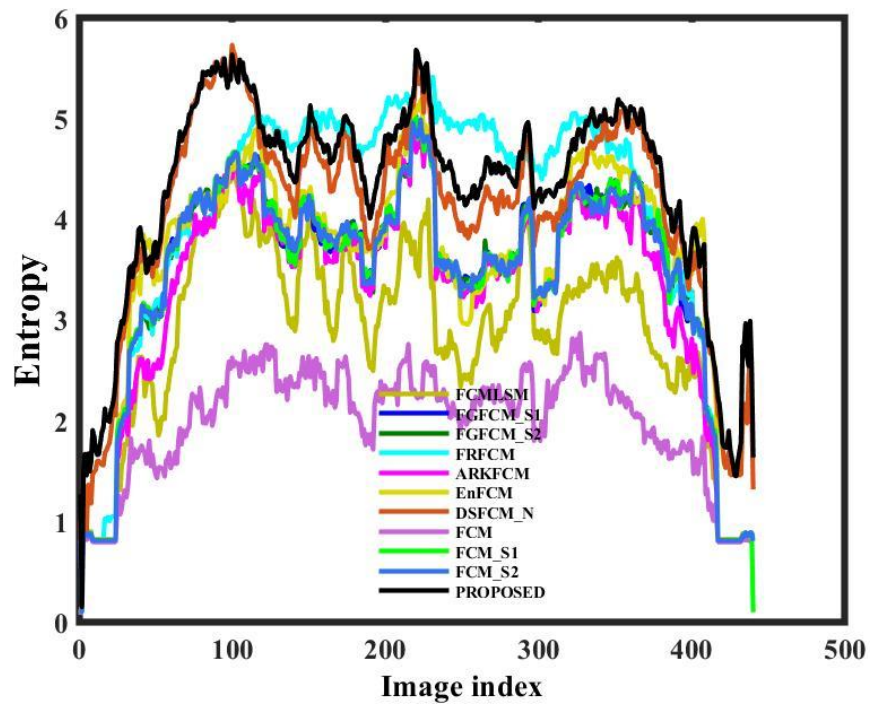**Fig. 5.15** Entropy plot for Test image 1
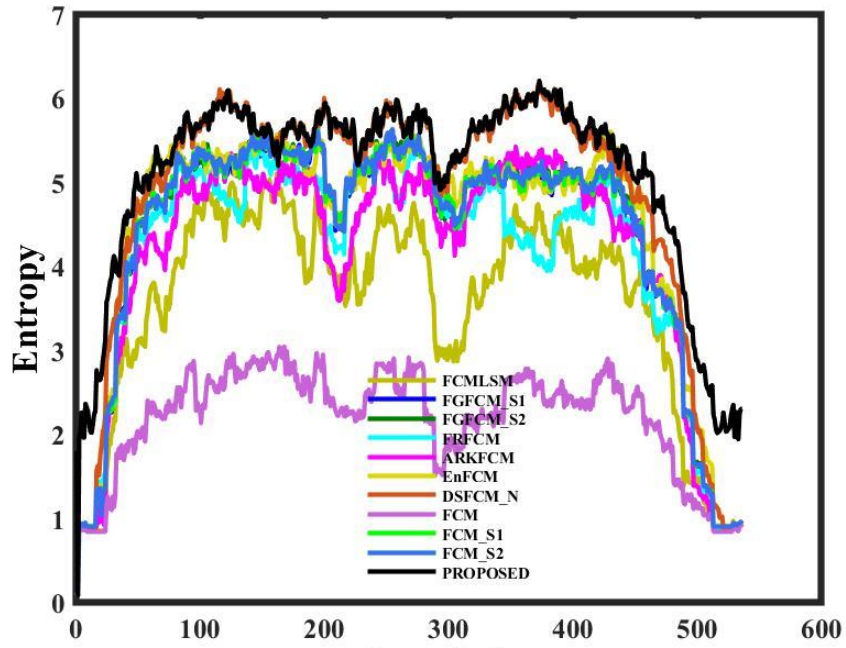


**Fig. 5.16** Entropy plot for Test image 2

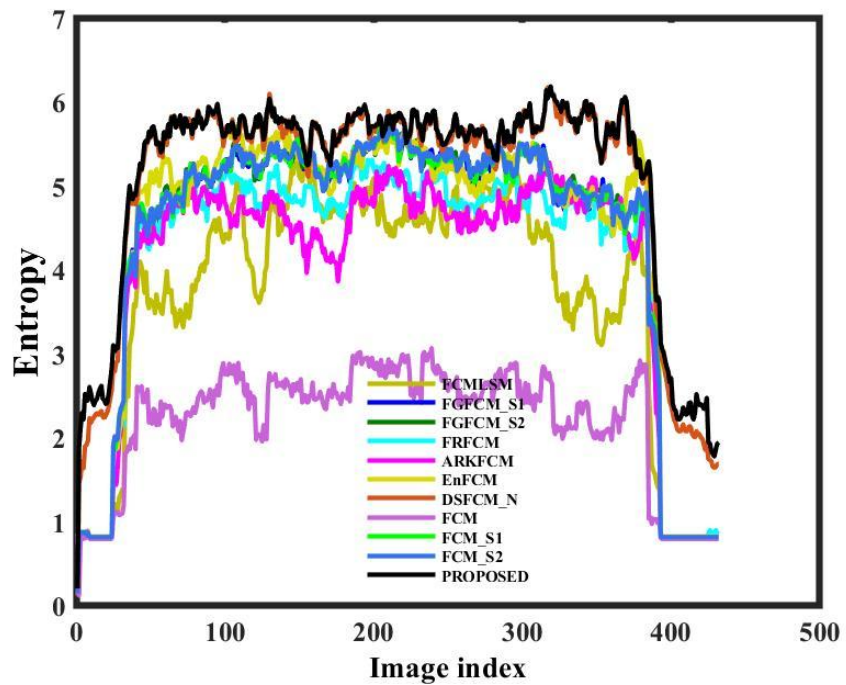**Fig. 5.17** Entropy plot for Test image 3



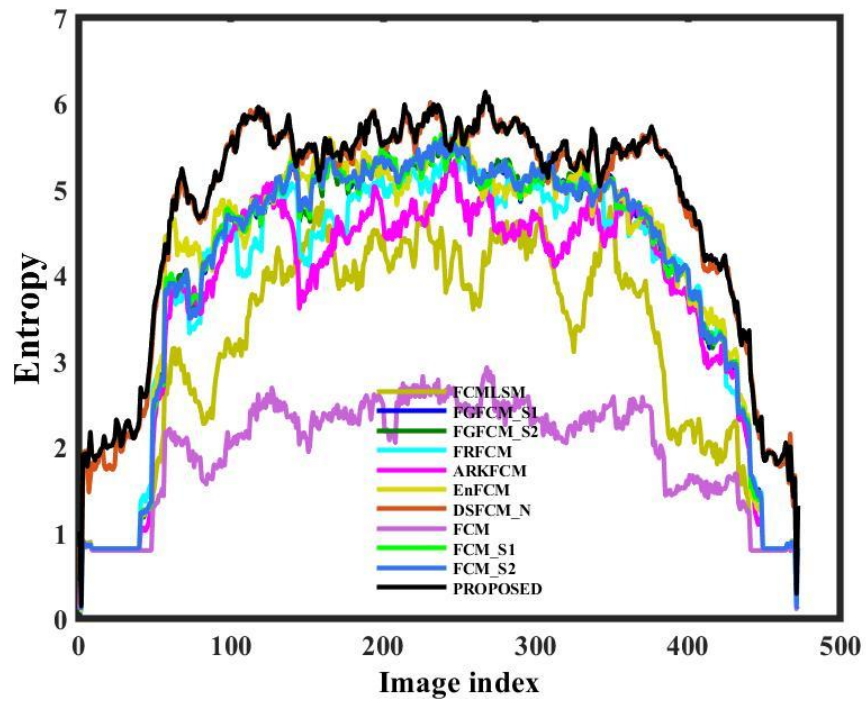**Fig. 5.18** Entropy plot for Test image 4

110

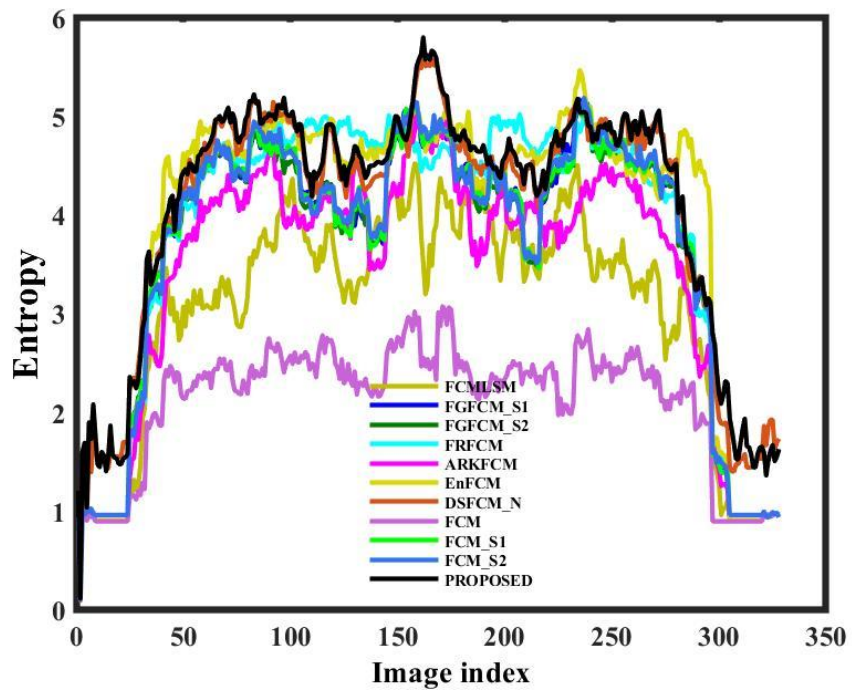**Fig. 5.19** Entropy plot for Test image 5.



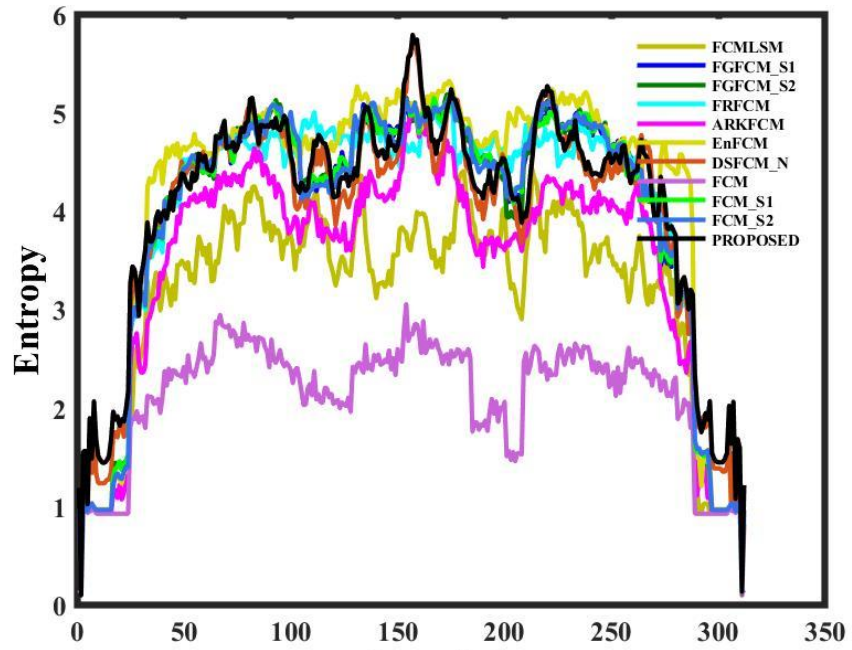**Fig. 5.20** Entropy plot for Test image 6.

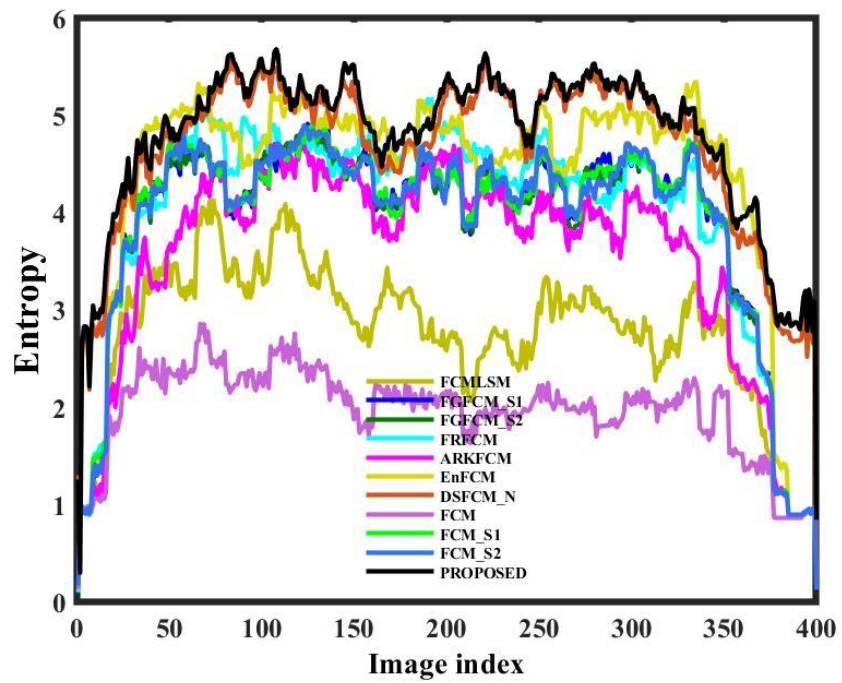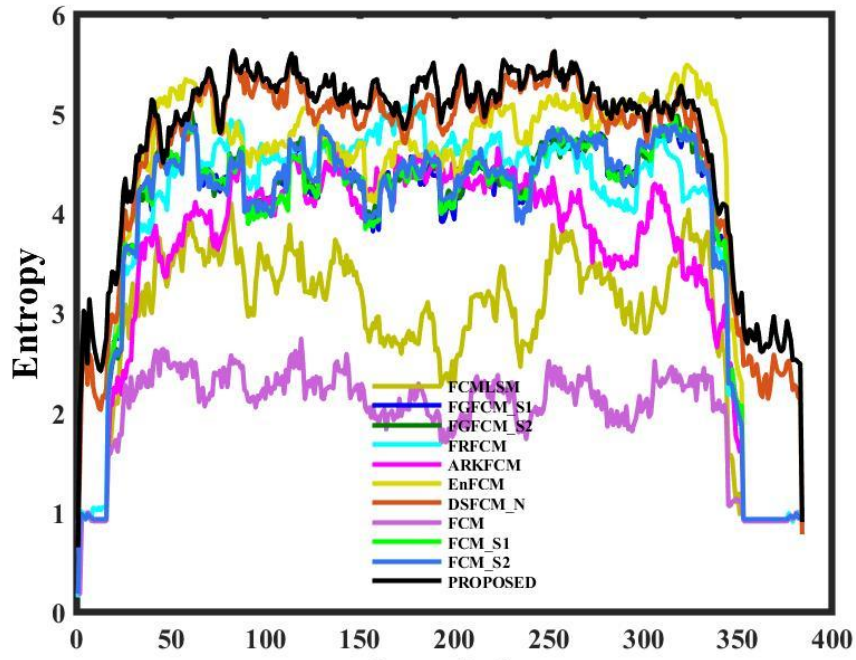**Fig. 5.21** Entropy plot for Test image 7



**Fig. 5.22** Entropy plot for Test image 8

112

**Fig. 5.23** Entropy plot for Test image 9
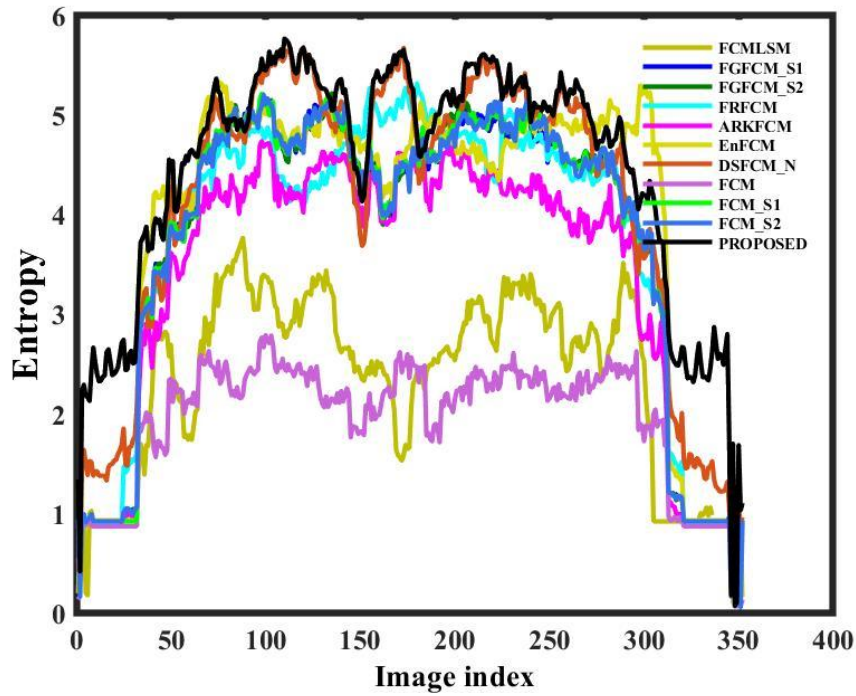


**Fig. 5.24** Entropy plot for Test image 10
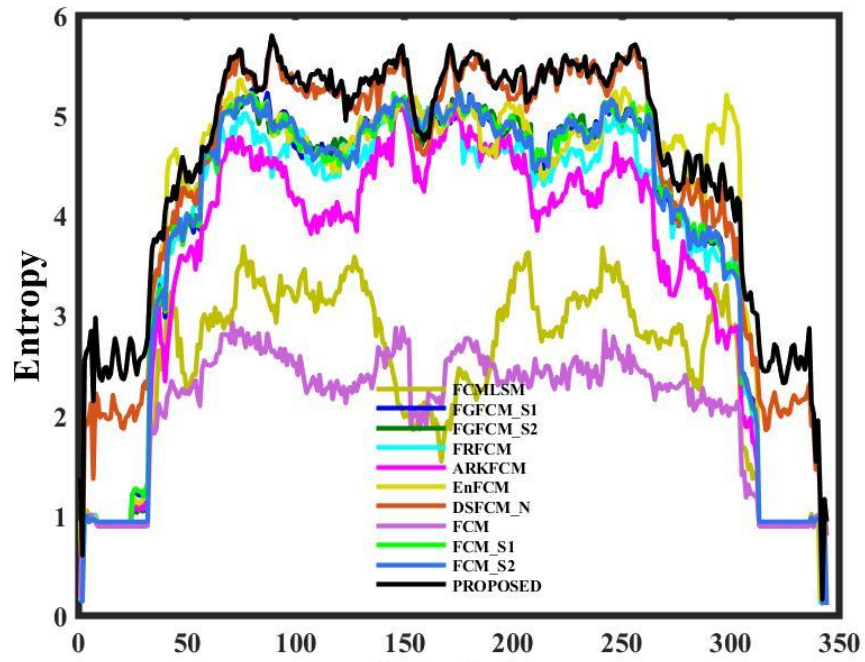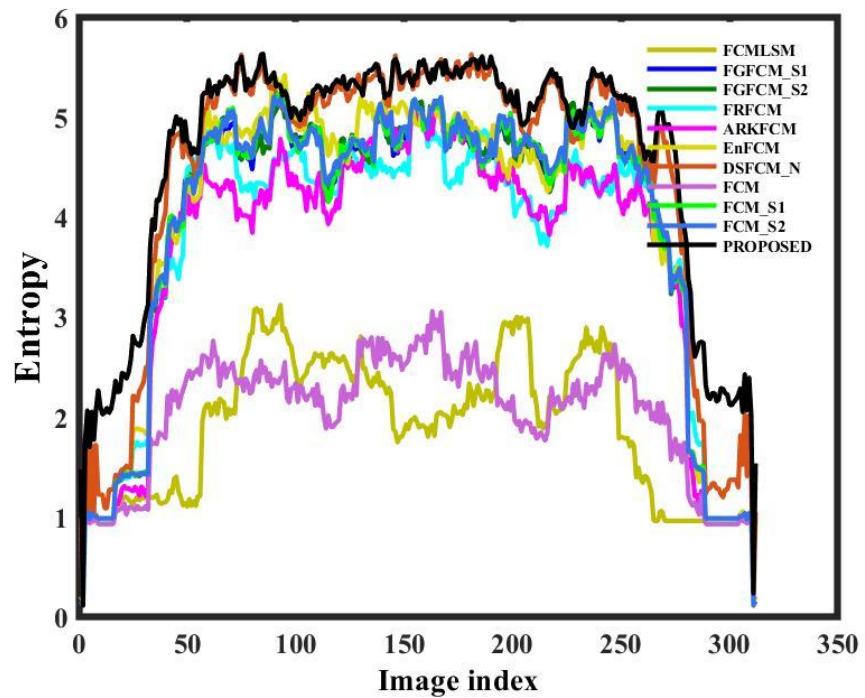
**Fig. 5.25** Entropy plot for Test image 11



**Fig. 5.26** Entropy plot for Test image 12

## 5.5   Discussion

In this chapter, an algorithm called Adaptive Neighbor Constrained Deviation Sparse Variant Fuzzy C-Means Clustering (AN_DsFCM) is proposed which can efficiently process the low contrast brain MRI scans. The presented algorithm meets the clustering accuracy required to figure out MCI. By incorporating the Rician noise to MR images, the problem domain becomes challenging as similar to practical standards. The intervention of sparse deviations reinforces AN_DsFCM to estimate theoretical artifacts and suppress noise. The novel strategy of neighbor information constraints strengthens AN_DsFCM to produce appropriate clustering parameters. Simulation results of proposed method demonstrate significant improvement in clustering accuracy both quantitatively and visually for ADNI and practical patient MRI data set. AN_DsFCM seems to be a viable tool to provide high-order clustering precision in MR images to predict MCI.

## REFERENCES

[1]  J. C. Bezdek, Pattern recognition with fuzzy objective function algorithms. Springer Science & Business Media, 2013.

[2]  M. N. Ahmed, S. M. Yamany, N. Mohamed, A. A. Farag, and T. Moriarty, "A modified fuzzy c-means algorithm for bias field estimation and segmentation of mri data," IEEE transactions on medical imaging, vol. 21, no. 3, pp. 193–199, 2002.

[3]  S. Krinidis and V. Chatzis, "A robust fuzzy local information c-means clustering algorithm," IEEE transactions on image processing, vol. 19, no. 5, pp. 1328–1337, 2010.

[4]  Y. Zhang, X. Bai, R. Fan, and Z. Wang, "Deviation-sparse fuzzy c-means with neighbor information constraint," IEEE Transactions on Fuzzy Systems, vol. 27, no. 1, pp. 185–199, 2018.

[5]  S. Pereira, A. Pinto, V. Alves, C. A. Silva, "Brain tumor segmentation using convolutional neural networks in MRI images," IEEE transactions on medical imaging, vol. 35, no. 5, pp. 1240–1251.

[6]  C. E. Shannon, "A mathematical theory of communication," Bell system technical journal, vol. 27, no. 3, pp. 379–423, 1948.

[7]  O. P. Verma and A. S. Parihar, "An optimal fuzzy system for edge detection in color images using bacterial foraging algorithm," IEEE Transactions on Fuzzy Systems, vol. 25, no. 1, pp. 114–127, 2016.

[8]  M. N. Ahmed, S. M. Yamany, N. Mohamed, A. A. Farag, and T. Moriarty. "A modified fuzzy c-means algorithm for bias field estimation and segmentation of MRI data," IEEE transactions on medical imaging, vol. 21, no. 3, pp. 193–199, 2002.

[9]  B. N. Li, C. K. Chui, S. Chang, and S. H. Ong, "Integrating spatial fuzzy clustering with level set methods for automated medical image segmentation," Computers in biology and medicine, vol. 41, no. 1, pp. 1–10, 2011.

[10]  T. Lei, X. Jia, Y. Zhang, L. He, H. Meng, and A. K. Nandi, "Significantly fast and robust fuzzy c-means clustering algorithm based on morphological reconstruction and membership filtering," IEEE Transactions on Fuzzy Systems, vol. 26, no. 5, pp. 3027–3041, 2018.

[11] A. Elazab, C. Wang, F. Jia, J. Wu, G. Li, and Q. Hu, "Segmentation of brain tissues from magnetic resonance images using adaptively regularized kernel-based fuzzy-means clustering," Computational and mathematical methods in medicine, vol. 2015, 2015.

[12] M. Gong, Y. Liang, J. Shi, W. Ma, and J. Ma, "Fuzzy c-means clustering with local information and kernel metric for image segmentation," IEEE transactions on image processing, vol. 22, no. 2, pp. 573–584, 2012.

[13] S-H. Wang, Q. Zhou, M. Yang, and Y. D. Zhang, "ADVIAN: Alzheimer's disease VGG-inspired attention network based on convolutional block attention module and multiple way data augmentation," Frontiers in Aging Neuroscience, vol. 13, no. 687456, 2021.

[14] H. Nawaz, M. Maqsood, S. Afzal, F. Aadil, I. Mehmood, and S. Rho, "A deep feature-based real-time system for Alzheimer disease stage detection. Multimedia Tools and Applications," vol. 80, pp.35789-35807, 2021.

[15] H. Sun, A. Wang, W. Wang, and C. Liu, "An improved deep residual network prediction model for the early diagnosis of Alzheimer's disease," Sensors, vol.21, no. 12, pp. 4182, 2021.

# Chapter 6

# Hippocampus Associated Functional 3D Connectivity Modeling

## 6.1 Introduction

Dementia due to early interventions of MCI should be essentially identified for taking precautionary measures. The disease can be traced with tissue loss in hippocampus and MTL and plays major role in cognitive and emotional ecstasy of long term memories [1-4]. Automated diagnosis of resting-state functional magnetic resonance imaging (Rf-MRI) leads to early identification of MCI limited spatial-temporal dependent dementia [5, 6]. The neuronal health and progression of AD can be estimated by retrieval and modeling of functional connectivity (FC) between major hubs of human brain [7 - 9]. Due to motion related artifacts at acquisition time, noise intervention and several other interventions; the sparse constraint becomes predominant in Rf-MRI. In the first phase of this chapter, a unique Kullback-Leibler (K-L) divergence based sparse constrained regression model is presented. The model creates a framework which identifies and analyzes FC between hippocampus and other significant region of interests (ROI) of brain. In the second phase of this chapter, a three dimensional hippocampus-parahippocampus FC analysis algorithm is presented to find out the early interventions of MCI. The semantic and episodic memory is formulated in MTL with hippocampus and associated parahippocampus, perirhinal and entorhinal neocortical subfields [10]. Hippocampus mostly controls the memory formation while neighboring cortices are responsible for memory storage. Due to interventions of MCI, tissue loss is observed in MTL and consequent FC degradation occurs in resting state f-MRI analysis. A robust quadratic detrending process is implemented to model both longer scan sessions and complex scanner drift constraints. The presented method examines the FC between each hippocampal subfields and parahippocampal subfields in its entirety. The outcome of simulated results in form of correlation

matrix exhibits promising efficiency of dealing functional connectivity constraints. The entire process leads to trace MCI related FC malfunctions more precisely.

## 6.2 Hippocampus Associative K-L Sparsity Constraint Model

### 6.2.1 Methodology

Input Rf-MRI test images are arranged in parallel for different subjects both in structural and functional formats. The hippocampus based neuronal activity modeling with whole brain is studied here. The proposed architecture is depicted in Fig. 6.1 which illustrates the Rf-MRI feature extraction and connectivity modeling. All the working steps can be mainly divided into four parts viz. preprocessing, denoising, connectivity mapping and result analysis.
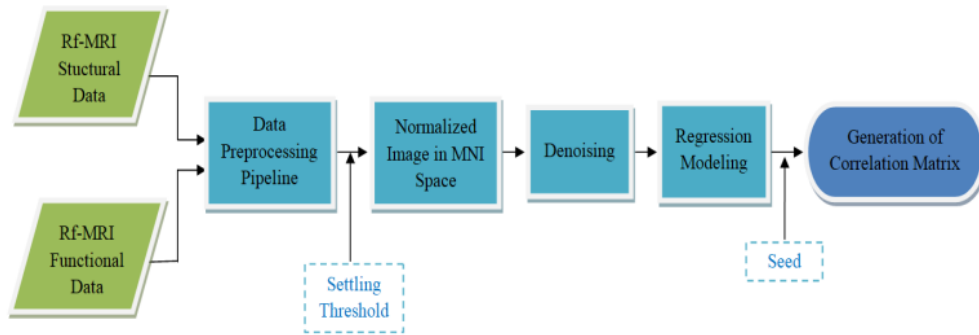


**Fig. 6.1** Complete architecture of proposed framework expanding K-L sparse constrained regression modeling

Let us assume that for a particular subject, the resting state f-MRI time series data is identified by $X = (x_1, x_2, \ldots, x_N)^T \in \mathbb{R}^{j \times i}$, where each vector $x_j \in \mathbb{R}^M$ where $(j = 1, \ldots, N)$ is associated with blood oxygen level dependent (BOLD) estimation for the $j^{th}$ ROI at $M$ consecutive time points. Total number of ROI is selected to be *N=136*. Based on BOLD time series data, a hippocampus to whole brain sparse connectivity learning model is constructed which can further be employed to figure out disease progression.

Normalization of BOLD time series is carried out for each ROI by $(X_j) = (X_j - \mu_j)/\sigma_j$, where $\mu_j$ and $\sigma_j$ respectively denotes mean and standard deviation of BOLD time series signal for $j^{th}$ ROI.

The average activated value of the $n^{th}$ hidden unit to all $i$ training samples will be

$$\hat{\xi}_n = \frac{1}{i} \sum_{m=1}^{i} g_i^2(x^m)$$

<div align="right">(6.1)</div>

where $g_i^2(x^m)$ represents the $n^{th}$ first autoencoder hidden unit output for the $m^{th}$ input.

A network sparse parameter is estimated and initiated with a value which is close to zero. This sparsity is introduced due to other ROI influence on target ROI and temporal BOLD time series correlation. To keep $\hat{\xi}_n$ more close to the sparse parameter of the network ξ, a Kullback-Leibler divergence sparsity constraint is introduced:

$$\sum_{n=1}^{S_L} KL\left(\xi \parallel \hat{\xi}_n\right) = \sum_{n=1}^{S_L} \left[\xi \log\frac{\xi}{\hat{\xi}_n} + (1-\xi) \log\frac{1-\xi}{1-\hat{\xi}_n}\right]$$

<div align="right">(6.2)</div>

In order to train components to learn the neighbor influence on local temporal properties from BOLD time series data, K-L sparsity constraints are imposed. Therefore, temporal-constrained convolution (*k* associated channels) property is defined for $X^t$ such as:

$$F_{m,n}^k = \sigma\left[W_m^k * \chi_m^t * \chi_n^t * KL\left(\xi \parallel \hat{\xi}_n\right)\right]$$
$$= \left[\sum_{l=0}^{L-1} W_{m,l}^k X_{m,l}^t X_{n,l}^t \left\{\alpha \sum_{n=1}^{S_L} KL\left(\xi \parallel \hat{\xi}_n\right)\right\}\right]$$

<div align="right">(6.3)</div>

where $W_m^k$ represents the learning weights $(1 \times L)$ for the $k^{th}$ kernel, $\chi_m^t$ and $\chi_n^t$ are time series sections for $m^{th}$ and $n^{th}$ ROIs respectively and $F_{m,n}^k$ is the learned correlation between $m^{th}$ and $n^{th}$ ROIs.

Hub regions frequently form distinct contributions to gross distribution of functional connectivity. Hence a specific set of filters for each ROI is learned and further shared across diverge time frames to identify and distinguish hub regions. Considering *K* channels for each segment, a dynamic *K* functional connectivity network is constructed. The connections between seed ROI and remaining (*N-1*) ROI are learned in data-driven manner via equation (6.2) and the connectivity between each ROI with itself is set to 0. Thus from equation (6.3), sparse constrained whole brain hippocampus dependency is estimated.

## 6.2.2 Experimental Results

In this research work, the preprocessed brain images have been collected from brain imaging data structure (BIDS) database available in openneuro repository (accession number ds002422). The functional MRI dataset chosen for simulation is resting state analysis to reduce psychological artifacts. This is done due to estimation of MCI progression from brain network connectivity. The experimental simulation is done using MATLAB based Statistical Parametric Mapping (SPM12) software and Resting-State fMRI Data Analysis (REST) toolkit.

To reduce the effect of motion related physiological artifacts, many confound factors are regressed before functional connectivity analysis. The preprocessing data path is set for volume and surface based analysis in MNI (Montreal Neurological Institute standard atlas) space with repetition time 3.56 seconds and interleaved Siemens slice order. The structural overlay over functional response during preprocessing is analyzed with harvard oxford cortical atlas. Furthermore, the quality assurance check is confirmed over plotted overlay with MNI boundary. Settling down the covariates is done with frame wise displacement parameter and head motion movement parameters. The structural and functional data are set parallel with conservative thresholding in normative sampling to retain maximum BOLD particulars for each subject. For default tissue probability map, a structural target resolution is set as 1 mm and functional target resolution as 2 mm with settling appropriate bounding box. Moreover, the ROI to ROI dynamic connectivity regression analysis for proposed algorithm is implemented. The polynomial expansion adds higher ability of handling detrending and despiking for the regressor.
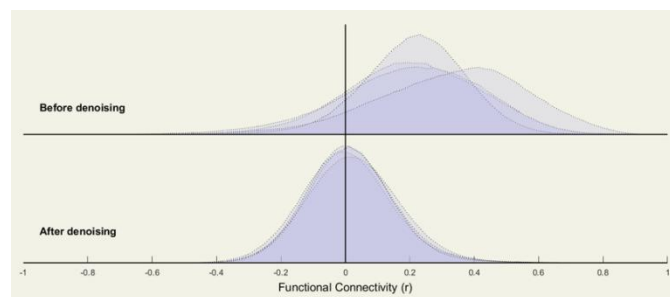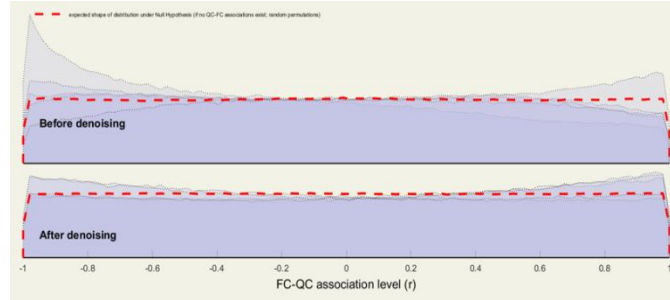
Fig. 6.2 BOLD signal traces in carpet plot and ART time series

To trace the physiological connection between different brain regions and hippocampus, it is first identified by the simulator. Fig. 6.3 and 6.4 depict the simulation results that automatically fetch the hippocampus region for each subject.


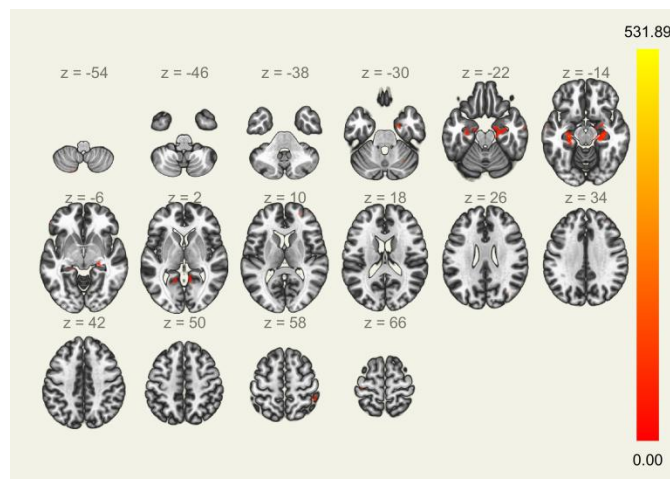Fig. 6.3 Right hippocampus identified by proposed algorithm


Fig. 6.4 Left hippocampus identified by proposed algorithm

Finally the correlation of blood-oxygen levels for a large set of two hundred thirty one ROIs is analyzed for whole brain to find out hippocampus dependency map. Fig. 6.5 and 6.6 respectively identify right hippocampus and left hippocampus connectivity where the red links represent significantly correlated and the blue links represent significantly negative ROI connectivity with selected seed. It is observed from the executed results that the right hippocampus and left hippocampus have most likely correlations. This is found because of functional homogeneity between right hemisphere and left hemisphere.
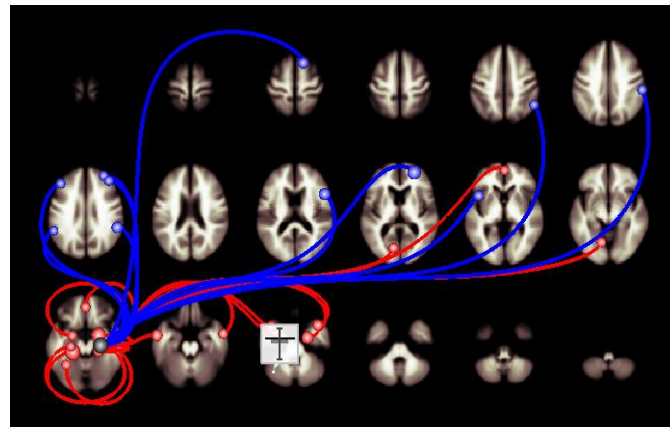


**Fig. 6.5** Right hippocampus connectivity with different ROI
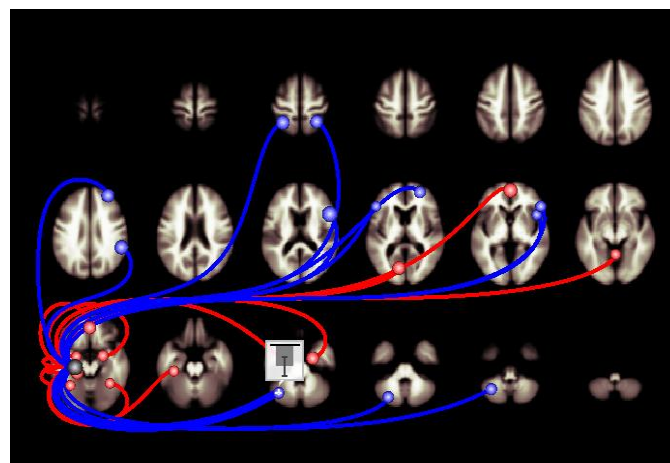


**Fig. 6.6** Left hippocampus connectivity with different ROI

A three dimensional transparent brain with all the nodes overlay connecting right hippocampus and left hippocampus is displayed in Fig. 6.7 and 6.8 respectively. The large set-study regarding transparent brain connectivity analysis shows both hippocampus regions posses higher correlation coefficient with medial temporal lobe. The significant correlation between the nodes as a whole in connector ring is displayed in Fig. 6.9 where any pair of ROI connectivity can be
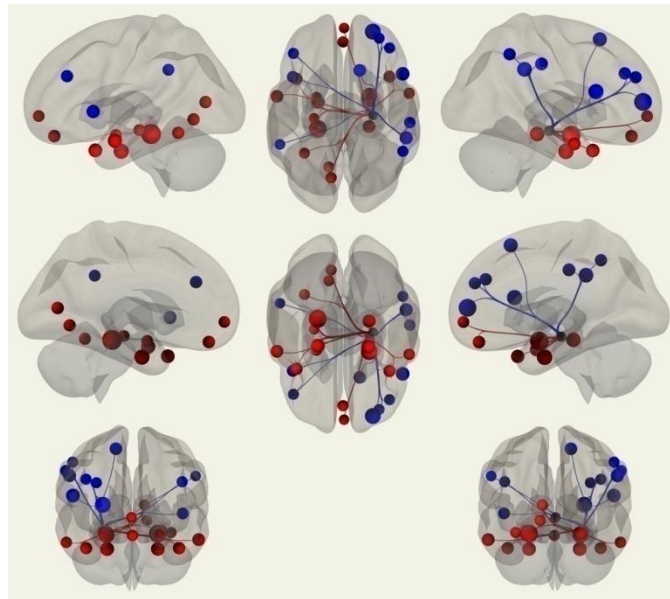
studied.



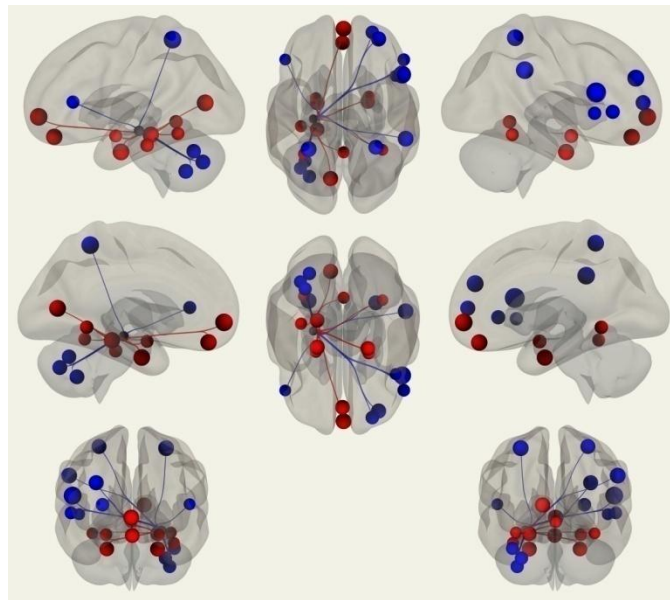**Fig. 6.7** Proposed right hippocampus connectivity identification in 3D



**Fig. 6.8** Proposed left hippocampus connectivity identification in 3D
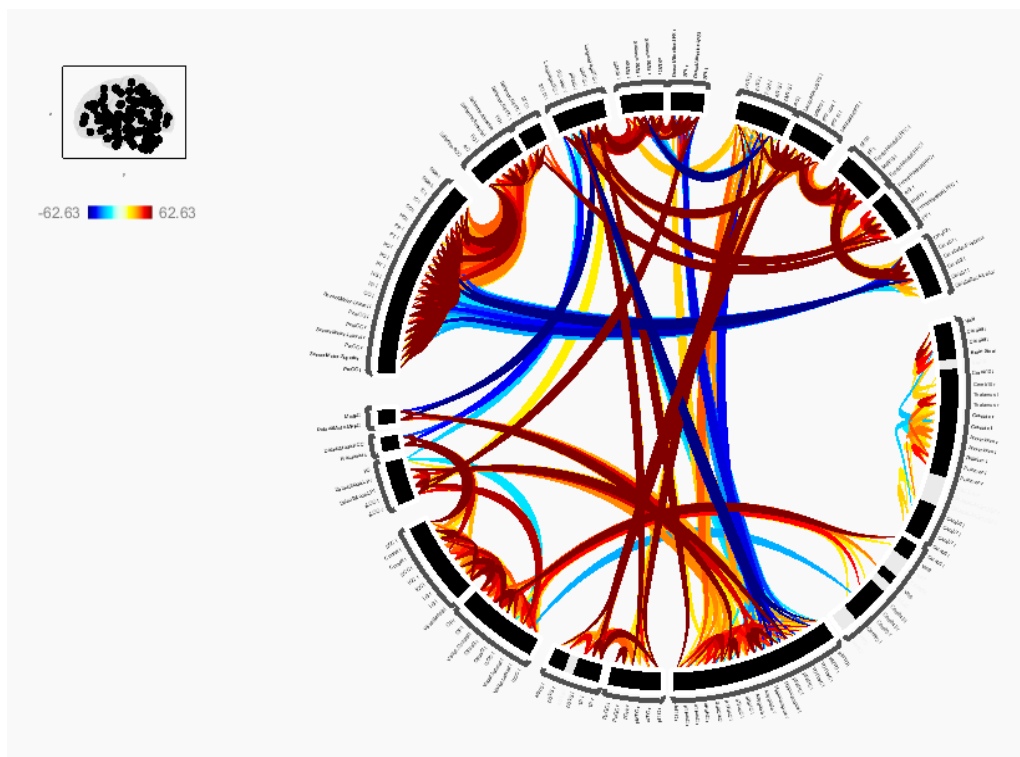
**Fig. 6.9** Simulated whole brain cluster set connectivity montage (No of clusters: 231)

# 6.3 Hippocampus-Parahippocampus Functional 3D Connectivity Modeling

## 6.3.1 Methodology

Structural and functional Rf-MRI images corresponding to different subjects are arranged in parallel for input test set. Neuronal activity of hippocampus is severely degraded due to progression of MCI. Parahippocampus is regarded as a major neighbourfield attached to hippocampus in temporal lobe. It is also responsible for memory organization and retrieval in association with hippocampus. The degraded hippocampal memory handling capability with progression of MCI must be reflected as functional connectivity in parahippocampal associability in resting state. In this section, a hippocampus-parahippocampus functional connectivity has been studied which can be divided into subsections such as: data acquisition, preprocessing, denoising, FC mapping on target ROI and result analysis.
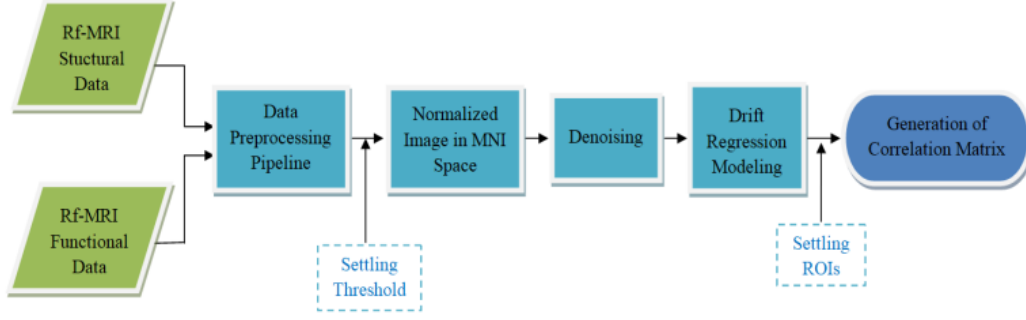
**Fig.6.10** Complete architecture of proposed framework expanding drift regression modeling

Let us consider that for a particular subject, the Rf-MRI time series data is represented by $\mathbb{X} = (f_1, f_2, \dots, f_N)^T \in \mathbb{R}^{i \times j}$, where each vector $f_i \in \mathbb{R}^M$ $(i = 1, \dots, N)$ is associated with BOLD estimation of $i^{th}$ ROI at $M$ successive time point.

Based on BOLD time series data, a hippocampus to parahippocampus quadratic detrending connectivity learning model is formulated which is capable to figure out AD progression. Initially, the normalization of BOLD time series is done for each ROI of interest:

$$N(f_i) = \frac{(f_i - \mu_i)}{\sigma_i}$$

(6.4)

where $\mu_i$ and $\sigma_i$ $(i = 1, \dots, N)$ respectively identify the mean and standard deviation of BOLD time series signal for $i^{th}$ ROI.

In order to put together the proposed quadratic detrending, the main objective becomes optimizing $f : \mathbb{X} \to \mathbb{R}$, where $\mathbb{X}$ represents a metric space. Let us consider $f$ is the Borel $\alpha$ −field, $\mu$ is a measure on $\mathbb{X}$ and $f$ is $\mu$ measureable. $\vartheta$ expresses any monotonically increasing set function on $\mathbb{F}$ which can be represented as $\vartheta(A) \leq \vartheta(B)$ for any $A, B \in \mathbb{F}$ and $A \subseteq B$. Moreover, $f$ is transformed to an invariant cost function which is defined as $V_f : x \to \vartheta[y : f(y) \leq f(x)]$. A family of probability distribution $P_\theta$ is considered on $\mathbb{X}$. A quasi objective function $J$ in the parameter space $\theta$ with the expected value of $V_f$ over $P_\theta$ can be expressed as:

$$J(\theta) = \mathbb{E}_{X \sim P_\theta}\left[V_f(X)\right]$$

(6.5)

The natural gradient is calculated with respect to the Fisher metric, which is the inverse component of Fisher information matrix $I_\theta$ and vanilla gradient $\nabla J(\theta)$ of the function. Hence the

natural gradient of $J$ is $I_\theta^{-1} \nabla J(\theta)$. The parameter update rule can be formulated as

$$\theta^{t+1} = \theta^t - \eta^t I_{\theta^t}^{-1} \nabla J(\theta^t)$$

(6.6)

where learning rate is expressed by $\eta^t$.

The main objective is to focus on optimizing $f: \mathbb{X} \to \mathbb{R}$, where $\mathbb{X}$ is in metric space. So, it can be conferred as $\mathbb{X} = \mathbb{R}$, where $\mu$ $and$ $\mathbb{F}$ are Lebesgue measure on $\mathbb{R}$ and Borel $\sigma$-field on $\mathbb{R}$. Let us choose the sampling Gaussian distribution $P_\theta$ $(\theta \in \Theta)$ where mean vector $m(\theta)$ is in $\mathbb{R}$ and the covariance matrix $C(\theta)$ is a $d$-dimensional positive definite and symmetric matrix.

Now the invariant cost $V_f(x)$ is defined with the help of Lebesgue measure $\mu_{Leb}$ as:

$$V_f(x) = \mu_{Leb}^{d/2}[y: f(y) \le f(x)]$$

(6.7)

The infinitum of $J(\theta) = \mathbb{E}_{X \sim P_\theta}[V_f(X)]$ becomes zero which is located on boundary contour of the domain $\Theta$ where the covariance matrix is zero and mean vector becomes equal to the global minimum of $f$.

The parameterization of Gaussian distribution $P_\theta$ puts an impact on natural gradient update with learning rate $\eta^t$. Covariance matrix and mean vector are chosen as the parameters of the Gaussian distribution. Let us have $\theta = [m^T, vec(C)^T]^T$ , where $vec(C)$ represents the vectorization of $C : [\{C\}_{(i,j)} \equiv \{vec(C)\}_{(i+d(j-1))}]$ [10]. Analytical form of Fisher information matrix is given by:

$$I_0 = \begin{bmatrix} C^{-1} & 0 \\ 0 & \frac{1}{2}(C^{-1} \otimes C^{-1}) \end{bmatrix}$$

(6.8)

where $\otimes$ represents the Kronecker product operator. On some regulatory conditions, we have

$$\nabla J(\theta) = E_{X \sim P_\theta}\left[V_f(X) \nabla l \nabla(\theta; X)\right]$$

(6.9)

where $l(\theta, x) = ln p_\theta(x)$ is long likelihood. The long likelihood of $l(\theta, x)$ can be expressed as

$$\nabla l(\theta, x) = \begin{bmatrix} C^{-1}(x - m) \\ \frac{1}{2}vec(C^{-1}(x-m)(x-m)^T C^{-1} - C^{-1}) \end{bmatrix}$$

(6.10)

Now the natural gradient becomes

$$I_\theta^{-1}\nabla J(\theta) = [\delta m^T, vec(\delta C)^T]^T$$

(6.11)

At $\theta = \theta^T$, natural gradient can be expressed by part such as:

$$\delta m^t = \mathbb{E}_{X \sim P_{\theta t}}[V_f(X)(X - m^t)]$$

(6.12)

$$\delta C^t = \mathbb{E}_{X \sim P_{\theta t}}[V_f(X)((X - m^t)(X - m^t)^T - C^t)]$$

(6.13)

For different learning rates in natural gradient algorithm, the mean vector and covariance matrix update can be formulated as:

$$m^{t+1} = m^t - \eta_m^t \delta m^t \text{ and } C^{t+1} = C^t - \eta_C^t \delta C^t$$

(6.14)

This is regarded as deterministic natural gradient descent (NGD) method. Now the stochastic NGD algorithm can be approximated to the ideal value as the size of $n$ becomes sufficiently large. Therefore, the NGD algorithm converges on convex quadratic detrending function and takes down the form as:

$$f(x) = (x - x^*)^T P(x - x^*) + f^*$$

(6.15)

where P is positive definite symmetric matrix, $x$ is variable input set and $x^*$ is considered as the global optimum solution.

A dynamic detrending functional connectivity network is constructed between hippocampus and parahippocampus in a data-driven manner with zero initialization weight settling via eq. (6.15).

### 6.3.2 Experimental Results

In this research work, the preprocessed MRI brain images are collected from brain imaging data

structure (BIDS) database which is available at openneuro repository (accession number: ds002422). In particular, the resting state functional MRI dataset is chosen to reduce psychological artifacts. Rf-MRI analysis also provides the precision accuracy required to estimate MCI progression. Experimental simulations are executed in MATLAB based Statistical Parametric Mapping software (SPM12) and Resting-State fMRI Data Analysis (REST) toolkit.

To model both complex scanner drift constraints and longer scan sessions, several confound factors are regressed in FC analysis. The volume and surface based analysis in MNI space for preprocessing data path is set with repetition time of 3.56 seconds and interleaved Siemens slice order. The functional response on top of structural overlay during preprocessing is analyzed with harvard oxford cortical atlas. Moreover, the quality assurance is checked overlay within MNI boundary. The structural and functional MRI data is analyzed in parallel with conservative thresholding in normative sampling. This process conserves maximum of BOLD properties for each subject. Proposed quadratia detrending is further formulated and implemented. A three dimensional dynamic FC between hippocampus and parahippocampus is executed in the context of proposed regression analysis. The quadratic components in deternding expansion provide higher ability of modeling drift constraints and despiking.

Prominent functional connectivity between different brain ROIs and parahippocampus is first identified by simulator. Fig. 6.11 to 6.14 has depicted the automatically fetched parahippocampus connectivity network for both anterior and posterior sections. Depending on BOLD statistics, two hundred and thirty one significant ROIs have been analyzed in each simulation. In the resultant connectivity mapping, blue links represent significantly negative correlations and red links signify prominently correlated connectivity pairs.

Simulated 3D transparent brain module on multiple view angle is displayed in Fig. 6.15 to 6.18. All prominent nodes connectivity overlay with parahippocampus sub-regions is identified and demonstrated. The hippocampus connectivity overlay with all prominent nodes is exhibited in Fig. 6.19 and 6.20 which is quite similar to parahippocampus. It is observed from brain connectivity analysis that hippocampus-parahippocampus gyrus sub-regions have higher FC correlation with medial temporal lobe. The final simulated output that correlates all possible

hippocampus-parahippocampus subfield combination in terms of connectivity strength is displayed in Fig. 6.21. It is observed that most likelihood correlation is found between left hippocampus and right hippocampus. Significant correlation between all major paired ROIs as a whole in a connector ring format is studied and displayed in Fig. 6.22. This study additionally helps to understand the overall hippocampus-parahippocampus dependency in resting state condition.
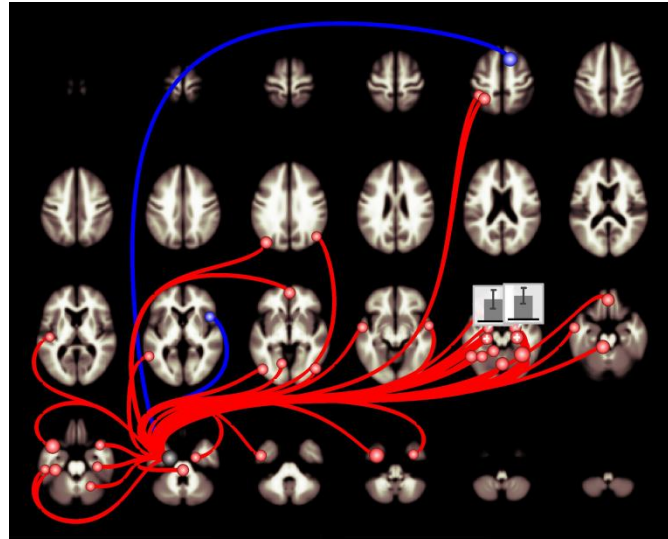


**Fig. 6.11** Parahippocampus functional connectivity link (anterior left)
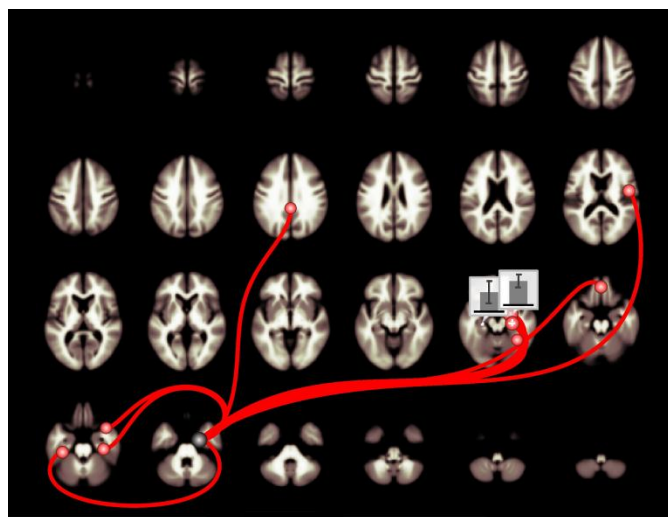


**Fig. 6.12** Parahippocampus functional connectivity link (anterior right)
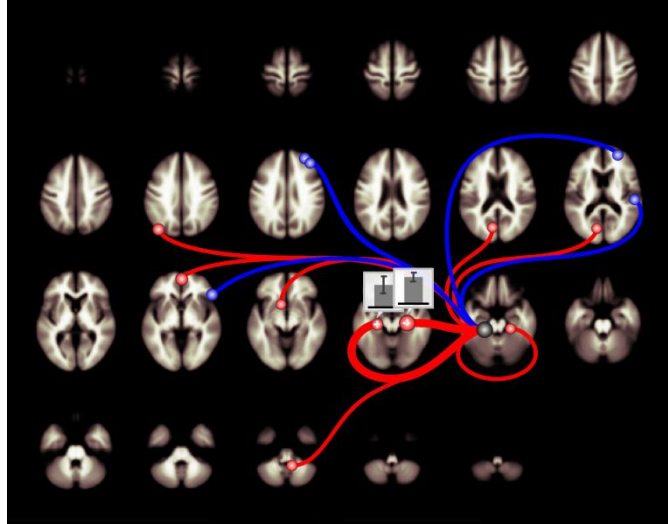
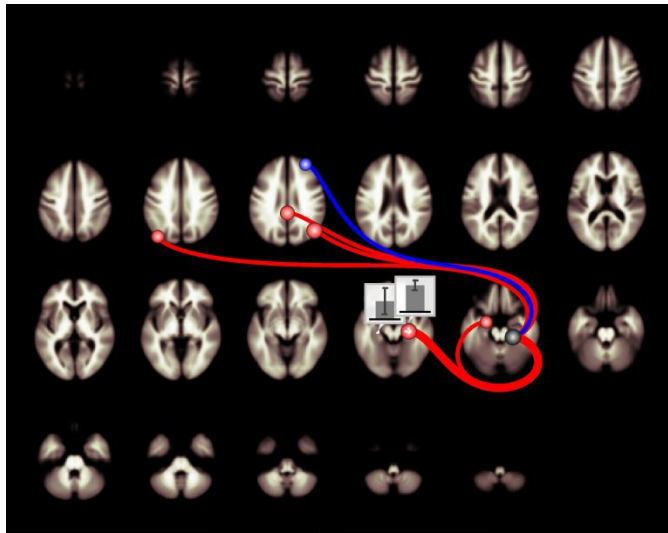**Fig. 6.13** Parahippocampus functional connectivity link (posterior left)



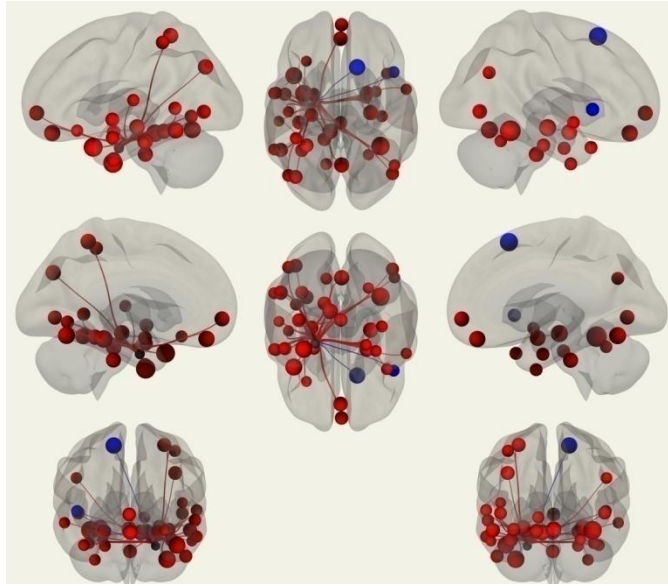**Fig. 6.14** Parahippocampous functional connectivity link (posterior right)

**Fig. 6.15** Parahippocampus functional connectivity in 3D (anterior left)
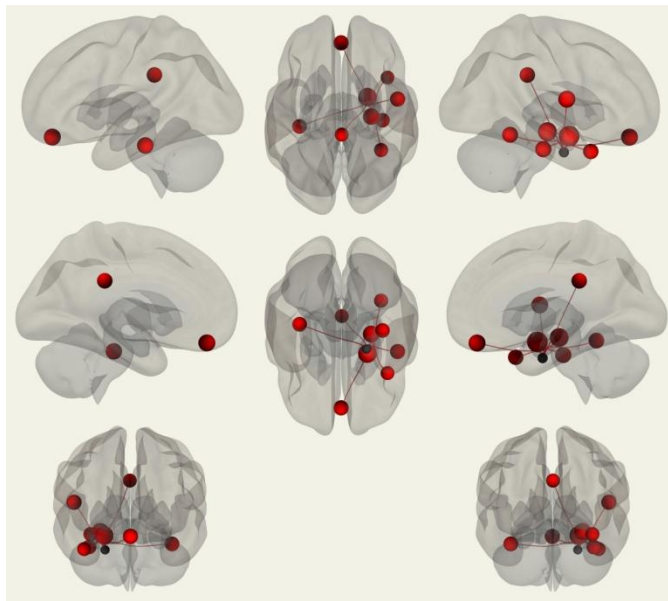


**Fig. 6.16** Parahippocampus functional connectivity in 3D (anterior right)
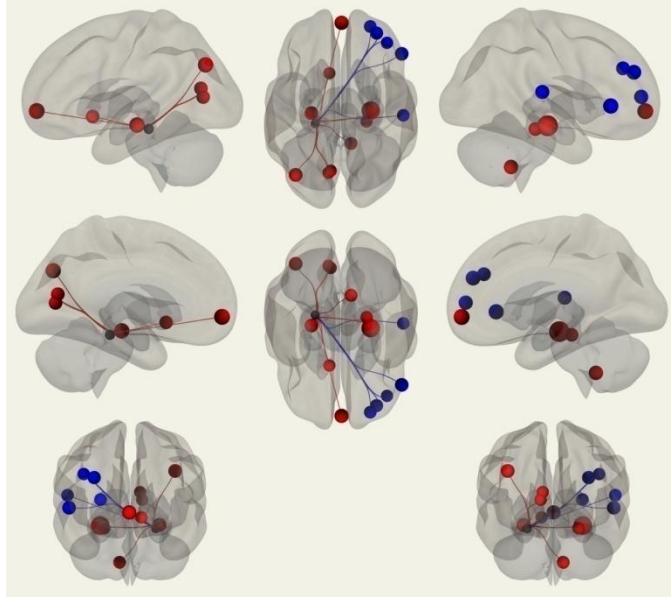
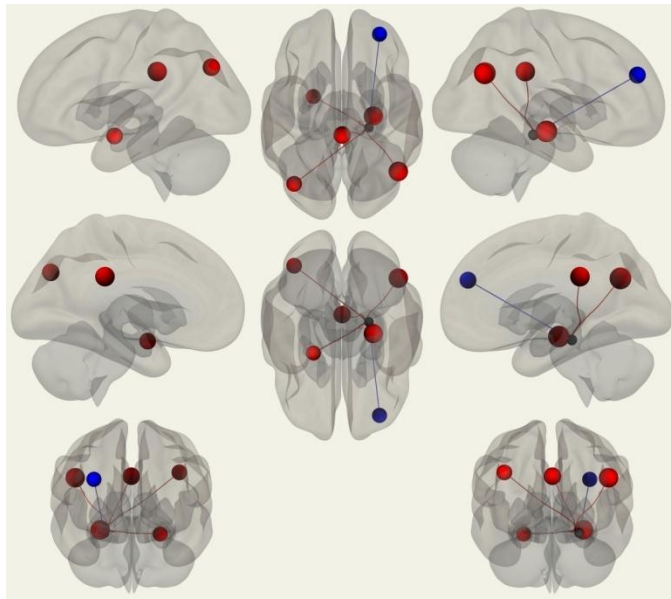**Fig. 6.17** Parahippocampus functional connectivity in 3D (posterior left)



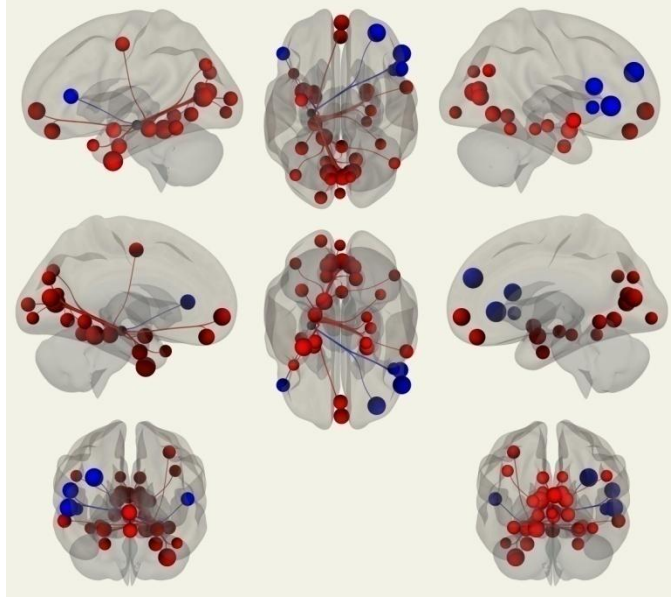**Fig. 6.18** Parahippocampus functional connectivity (posterior right)

**Fig. 6.19** Left hippocampus functional connectivity in 3D
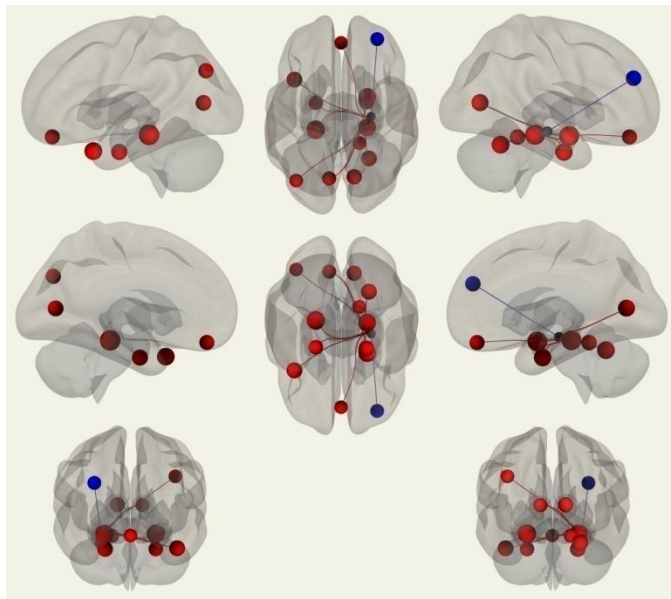


**Fig. 6.20** Right hippocampus functional connectivity in 3D
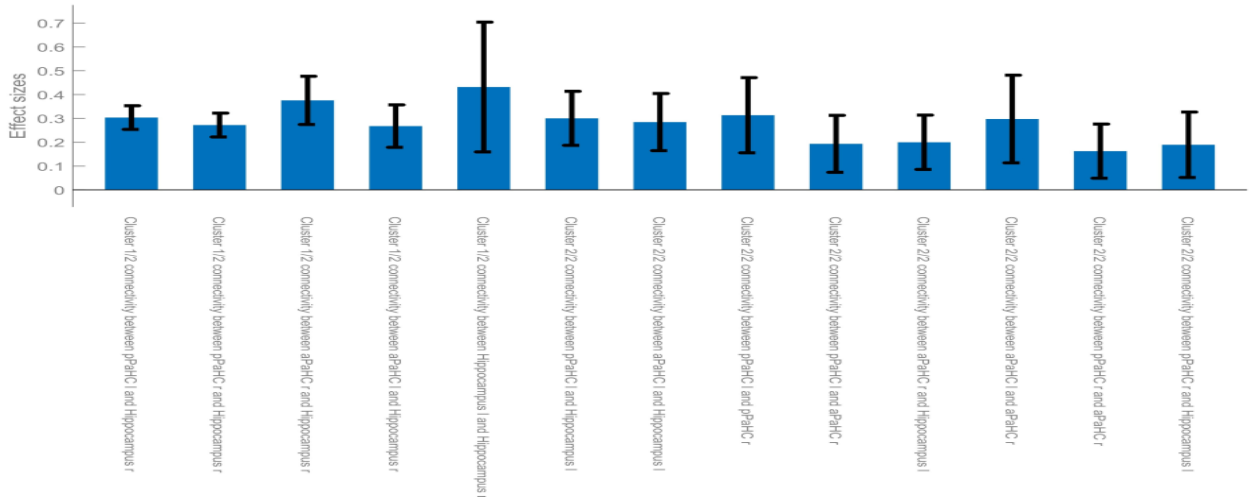
**Fig. 6.21** Functional connectivity measure between all parahippocampus and hippocampus subfields



**Fig. 6.22** Cluster set connectivity montage of whole brain (No of clusters: 231)

## 6.4 Discussion

In the first phase of this chapter, a robust nonlinear K-L sparsity constrained FC model is implemented successfully for brain connectivity analysis. The presented model not only identifies high-order sparse dependency patterns but also recognizes major ROIs to learn spatial

correlation. The algorithm executes the Rf-MRI data simulation by considering hippocampus as the seed ROI. Hence, the entire process leads to the identification of cognitive degradation due to MCI. The presented method pro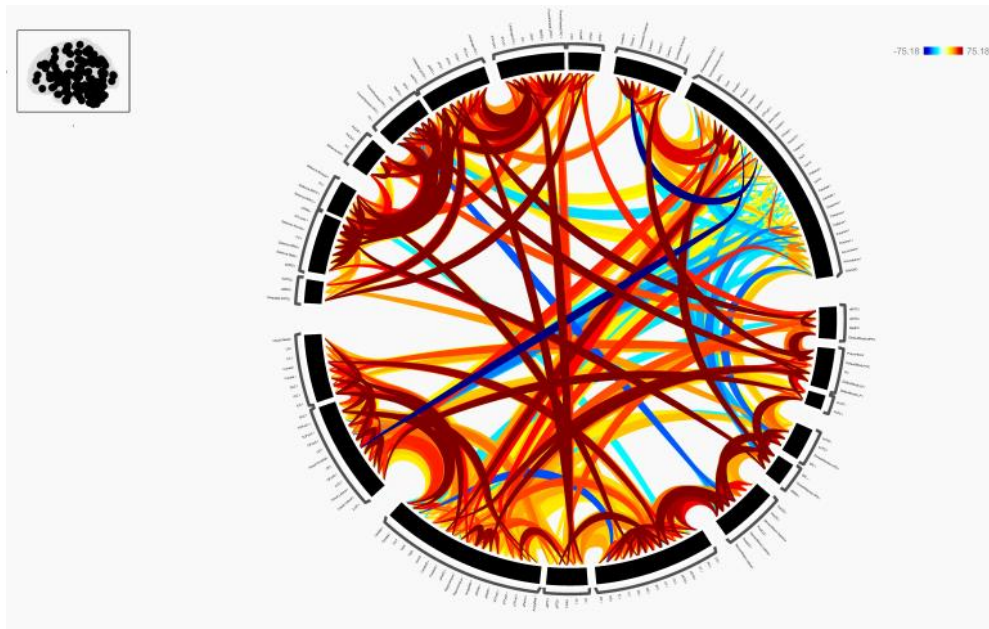duces a promising outcome that models whole brain hippocampus connectivity in 3D. In the second phase of this chapter, a robust quadratic detrending based hippocampus-parahippocampus interactive 3D functional connectivity model is executed successfully to figure out early sign of MCI. The presented algorithm models complex scanner drift constraints and it is capable to handle constraints in longer scan sessions for elder and young subjects. The presented algorithm runs on Rf-MRI data and considers hippocampus and parahippocampus subfields as pair ROIs for FC analysis. The simulated results demonstrate a promising outcome which models hippocampus-parahippocampus functional connectivity.

## REFERENCES

[1]   Y. Noh *et al.* Anatomical heterogeneity of Alzheimer disease: based on cortical thickness on MRIs. Neurology, vol. 83, pp. 1936–1944, 2014.

[2]   Whitwell, J. L. *et al. "*Neuroimaging correlates of pathologically defined subtypes of Alzheimer's disease: a case-control study", Lancet. Neurol, vol. 11, pp. 868–877, 2012.

[3]   D. Ferreira et al., "Distinct subtypes of Alzheimer's disease based on patterns of brain atrophy: longitudinal trajectories and clinical applications," Nature Neuroscience, doi: 10.1038/srep46263., 2017.

[4]   Whitwell, J. L. *et al. "*Temporoparietal atrophy: a marker of AD pathology independent of clinical diagnosis", Neurobiol. Aging 32, pp 1531–1541, 2011.

[5]   J. S. Damoiseaux, "Resting-state fMRI as a biomarker for Alzheimer's disease?", Alzheimer's Research and Therapy, vol. 4, no. 8, pp. 1–2, 2012.

[6]   M. Machulda, H. Ward, B. Borowski, J. Gunter, R. Cha, P. Obrien, R. Petersen, B. Boeve, D. Knopman, D. Tang-Wai et al., "Comparison of memory fMRI response among normal, MCI, and Alzheimer's patients," Neurology, vol. 61, no. 4, pp. 500–506, 2003.

[7]   B. Jie, D. Zhang, W. Gao, Q. Wang, C.-Y. Wee, and D. Shen, "Integration of network topological and connectivity properties for neuroimaging classification," IEEE Transactions on Biomedical Engineering, vol. 61, no. 2, pp. 576–589, 2013.

[8]   C.-Y. Wee, P.-T. Yap, D. Zhang, L. Wang, and D. Shen, "Groupconstrained sparse fMRI connectivity modeling for mild cognitive impairment identification," Brain Structure and Function, vol. 219, no. 2, pp. 641–656, 2014.

[9]   M. Odusami, R. Maskeliūnas, R. Damaševičius, and T. Krilavičius, "Analysis of features of alzheimer's disease: detection of early stage from functional brain changes in magnetic resonance images using a fine tuned ResNet18 network," Diagnostics, vol. 11, no. 6, pp.1071, 2021.

[10]  Dalton, M.A., McCormick, C. and Maguire, E.A., "Differences in functional connectivity along the anterior-posterior axis of human hippocampal subfields", NeuroImage, vol. 192, pp.38-51, 2019.

# Chapter 7

# Conclusion & Future Scope of Work

This thesis proposes and successfully implements several novel brain image processing algorithms which can potentially help us to diagnose Alzheimer's disease at an early stage. As of now, MRI analysis is considered to be the most efficient non invasive tool for AD diagnosis. In connection to this, high end application specific algorithms are expected to be developed which will provide necessary features like advanced edge detection, robust clustering algorithm or improved functional connectivity model etc. Traditional approaches of image processing provide satisfactory results for standard images. On the other hand, brain MRI scans are low pixel density images where exact detection of regional information is very challenging for MCI identification or estimating AD progression. In this work, state of the art fuzzy based edge detection, LV classifier & clustering tools are presented which can overcome the challenges by eliminating proxy edges or noise interventions. Additionally, advanced mathematical models are proposed which are implemented to model Rf-MRI data based hippocampus associated whole brain functional connectivity for accurate detection of MCI. In brief, major contributions of the thesis are summarized as follows:

- A novel fuzzy pixel intensity correlation based brain MRI segmentation algorithm for early detection of Alzheimer's disease
- A composite implementation of robust morphological filtering and self adaptive fuzzy c means clustering algorithm for segmentation of lateral ventricle
- An adaptive neighbor constrained deviation sparse fuzzy c-means clustering algorithm for brain MRI scans
- A robust Kullback-Leibler (K-L) divergence based sparse constrained regression model to study hippocampus associative functional connectivity structure
- An interactive hippocampus-parahippocampus functional 3D connectivity modeling with quadratic detrending

In a nutshell, this chapter briefly accumulates the technical advancements achieved through this research work. Concluding remarks on presented algorithms and scope of future research are further discussed.

## 7.1   Concluding Remarks

As the first contribution of this work, a novel fuzzy method is presented which follows the natural correlation of pixel properties that exist in edges of an image object. Proposed algorithm finds the connected edge contour based on image pixel intensities for brain MRI scans of AD subject. The executed algorithm, together with a robust image opening and morphological gradient, reveals promising improvement in detecting object edges more accurately. In this context, a robust fuzzy rule base and fuzzy inference system is designed and successfully implemented where a fuzzy pixel intensity weight-based topological selection of adjacent edge pixels has been initiated to achieve higher-order precision. The presented scheme emphasizes on settling up the primary edge pixel and finds out the next adjacent edge pixel dynamically based on correlation properties. Finally, the sorted out edge pixels are accumulated in a form of pixel matrix to settle an impression of edge contour. The presented strategy leads to trace early loss in tissue volume and helps us to detect the occurrence of AD.

As the second contribution of this work, lateral ventricle segmentation in brain MRI is focused since morphological changes of LV like hypertrophy exhibit very close relation with AD progression. This task becomes more challenging due to the presence of tinny or proxy edges, low contrast and noise in overlapping regions. In the presented work, a robust morphological filtering process is initiated which can eliminate noise, focus on ROI and avoid over estimation in image object boundary as well. Moreover, a self adaptive FCM clustering algorithm, ACWE algorithm and a RG algorithm is executed to segregate ventricular region. This unique combination of different algorithms provides an excellent improvement over LV region segmentation both qualitatively and quantitatively.

As the third contribution of this work, a novel FCM clustering algorithm is presented to trace MCI related tissue loss in medial temporal lobe and associated enlargement of LV. In execution of the proposed process, the rician noise is initially incorporated and sparsity is initiated in proposed clustering method in MR scans of AD subject. Secondly, a novel neighbor pixel

constrained FCM clustering algorithm is designed and implemented where topology dependent selection of parsimonious neighbor pixel is automated. The adaptability in selection of neighbor pixel class provides most justified object edge boundary which outperforms other clustering methods. The presented adaptive neighbor constrained deviation sparse variant fuzzy c-means clustering (AN_DsFCM) is capable to withhold imposed sparsity and efficiently withstands rician noise. The experimental outcomes are compared with state-of-the-art fuzzy clustering methods for standard MRI scans and normative data where visual evaluation and statistical measures meet both image processing and clinical neurophysiology standards.

In the first phase of fourth contribution of this work, an automated diagnosis of Rf-MRI based retrieval of FC among various hubs of human brain is developed to estimate the progression of MCI. The sparse constraint becomes predominant for functional connectivity in Rf-MRI particularly due to motion related artifacts during MRI acquisition, noise intervention and several other reasons. A unique Kullback-Leibler (K-L) divergence based sparse constrained regression model is implemented which develops a framework that identifies and analyzes connectivity between hippocampus and other significant ROIs of the brain. Simulation outcomes reveal promising improvement in FC measures of hippocampus subfields.

In the second phase of the fourth contribution of this work, an algorithm on a three dimensional FC analysis between hippocampus and parahippocampus is presented to trace MCI consequent FC degradation. The semantic and episodic memory is formulated in MTL with hippocampus and associated subfields like parahippocampus, perirhinal and entorhinal neocortical subfields. A novel quadratic detrending process is incorporated to model both complex scanner drift constraints and longer scan sessions. The motion related artifacts and noise interventions are also well handled by presented framework. Functional connectivity between each hippocampal subfield and parahippocampal subfields in its entirety are examined.

## 7.2   Future Scope of Work

In this thesis, different advancements of fuzzy based MRI and Rf-MRI data analyzing tools have been developed to meet the precision required for early detection of AD.
There are no significant limitations in the first and third contribution of this work as both the presented methods show their supremacy over other state-of-the-art techniques. The second

contribution of this work lacks in providing the lateral ventricle volume information as this method is limited by providing only 2D outcomes. Further development of 3D modelling of presented method will make the MCI classification process more robust. The fourth contribution of the presented work lacks in incorporating the FC interactions in MTL associated major ROIs. An in depth study of FC between MTL sub regions and whole brain significant ROIs will help to understand the information sharing degradation due to MCI intervention.

Algorithms demonstrated in this thesis fundamentally advance the image processing tools which can also be potentially implemented to trace other neurodegenerative diseases. In view of further advancements of more efficient diagnostic tools, some of the possible future scopes are discussed below:

- Detection of AD may also be targeted in future with the aid of other soft computing tools like neural network and machine learning approaches. The presented fuzzy based algorithm may be fused with deep learning technique; thus allowing large scale feature learning to explore higher accuracy for neuro-image classification or segmentation. Similarly, the combination of sparse representation and presented algorithms can be modeled to come up with better tools for brain image classification in future.

- A three dimensional modeling of lateral ventricle can be developed so that MCI can be predicted much more precisely. In addition to this, better filtering technique or higher order modeling of fused FCM clustering algorithm can also achieve better results in this context.

- Evaluation of presented FC algorithms on larger data can be further developed with machine learning or other soft computing based approaches to enhance the diagnosis standard for AD and other neurological diseases. A rigorous modeling on larger dataset can provide better disease specific diagnosis accuracy.